# COMPUTER-AIDED CRANIOMAXILLOFACIAL SURGERY PLANNING FOR FRACTURED SKULLS

CHENG YUAN

NATIONAL UNIVERSITY OF SINGAPORE

2014

# COMPUTER-AIDED CRANIOMAXILLOFACIAL SURGERY PLANNING FOR FRACTURED SKULLS

CHENG YUAN (HT080111R)

(B.Sc., Fudan University, China, 2008)

A THESIS SUBMITTED

FOR THE DEGREE OF DOCTOR OF PHILOSOPHY

DEPARTMENT OF COMPUTER SCIENCE

NATIONAL UNIVERSITY OF SINGAPORE

October 2013

# Dedication

*To my father Cheng Xiuxi,*

*my mother Zhang Liping,*

*my wife Hu Yaoyun.*

## Acknowledgements

I am deeply grateful to my supervisor, Professor Leow Wee Kheng for his patient and thoughtful supervision and continuous support during the whole period of my PhD study. Prof. Leow involved me in the project of computer-aided craniomaxillofacial surgery planning in the first place. He taught me the way of initiating a good and useful research topic, formulating a research problem, solving problems, conducting experiments, and writing scientific reports, etc. He was always responsible and provided encouragements and insightful ideas to me whenever I faced obstacles. Without Prof. Leow's great help, it is impossible for me to complete the thesis.

A special thanks goes to our collaborator, Professor Lim Thiam Chye at National University Hospital. Prof. Lim is a CMF surgeon who raised the requirements of the CMF surgery planning procedure, provided us with the data for experiments, and taught us the practical validation methods. He is a nice doctor that cares about his patients, and is enthusiastic about improving the treatment of CMF deformities.

I really appreciate my colleagues in Computer Vision lab: Ding Feng, Li Hao, Song Zhiyuan, Wang Yumei, Yang Xin, Zhang Kun, Guo Dong, Zhuo Shaojie, Ye Ning, Gao Junhong, Deng Fanbo, Lin Haiting, etc. It was my beautiful memories working with these brilliant people.

I would like to thank my beloved friends, Kennth Tay, Jessica Wang, Wei Xueliang, Lu Xuesong, Xu Yin, Li Gang, Liu Xiaomin, Chen Wei, Jin Yiping, etc. I really enjoyed the life in Singapore with them.

Last, but not least, I give my sincere thanks to my parents, my wife Hu Yaoyun and my whole family for their endless love, unconditional support and encouragement. I wish my grandfather, Cheng Shaocheng and my father-in-law, Hu Zaihua were here to see me finish.

# Abstract

Many patients suffer from skull deformity which may greatly affect their life quality and even threaten their lives. To restore normal appearances of skulls, craniomaxillofacial (CMF) surgery is performed. This surgery is very complex and requires careful pre-operative planning to determine how to reposition bone fragments to restore the deformed skulls.

There are two related problems in CMF surgery planning, namely restoration and reconstruction. Restoration seeks to restore a deformed skull back to its normal state by repositioning the bones in the deformed model. It directly results in a feasible surgery plan. Reconstruction, on the other hand, derives an estimate of the normal skull from the deformed skull by shape similarity. To use the reconstructed model for surgery planning, the surgeon needs to manually work out how to reposition the patient's bone fragments to match the reference as given by the reconstructed model. At present, there is no reliable automatic skull restoration method.

Many computer-aided systems have been developed for medical application. Reactive systems are real-time systems that attempt to simulate the reactions of the body in response to user inputs. They are more suitable for surgery training than surgery planning. Predictive systems attempt to accurately predict surgical results of complex surgical procedures based on predefined or user-specified surgical requirements. They are suitable for planning complex CMF surgery. Some existing computer-aided CMF systems generate reconstructed bone models, and others generate surgery plans for mandible restoration. To our best knowledge, there is no existing planning system that generates a restored skull model from a patient's deformed skull by bone repositioning.

The goal of this thesis is to develop a computer-aided procedure for assisting a surgeon in deriving a CMF surgery plan. In this procedure, the surgeon

first uses a semi-automatic segmentation algorithm to segment the patient's bone fragments from medical images and constructs the patient's deformed skull model from the segmentation result. Next, the surgeon uses a user-friendly tool to indicate bone fragments to be repositioned. Then, the surgeon identifies the salient surfaces of the skull semi-automatically. After that, the surgeon or an automatic algorithm identifies the MSP and FP landmarks on the patient's skull. Then, the surgeon applies an automatic restoration algorithm to generate a restored model by repositioning the fractured bone fragments. Finally, the plan is exported to DICOM and STL files for surgeon's verification and usage in surgery guidance system.

This thesis has three main contributions:

1. Development of a computer-aided procedure for assisting a surgeon in deriving a surgery plan for restoring a patient's deformed model back to the normal state by bone repositioning.
2. Development of an algorithm to automatically identify craniometric planes and landmarks of skulls.
3. Development of an algorithm to generate the restored model from a patient's deformed model.

The two algorithms in the computer-aided CMF surgery planning procedure were validated. For the automatic craniometric planes and landmarks identification algorithm, the test results on normal skulls and real patients' skulls validate its robustness and accuracy. For the skull restoration algorithm, the test results on real patients' data show that the algorithm satisfies surgical requirements and produces restored models similar to real post-operative skulls.

We are working with our collaborating surgeon to deploy the planning tool and algorithms for clinical trial. We hope that our research can help surgeons work out more accurate plans and benefit CMF patients.

# Contents

# List of Publications

1. K. Zhang, **Y. Cheng**, and W. K. Leow. Automatic Dense Correspondence of 3D Skull Models Based On Anatomical Landmarks. In Proceedings of International Conference on Computer Analysis of Images and Patterns (CAIP), 2013.

2. W. K. Leow, **Y. Cheng**, L. Zhang, and T. Sim. Background Recovery by Fixed-rank Robust Principal Component Analysis. In Proceedings of International Conference on Computer Analysis of Images and Patterns (CAIP), 2013.

3. **Y. Cheng**, W. K. Leow, and T. C. Lim. Automatic Identification of Frankfurt Plane and Mid-Saggital Plane of Skull. In Proceedings of IEEE Workshop on Application of Computer Vision (WACV), 2012.

4. D. Guo, **Y. Cheng**, S. Zhuo, and T. Sim. Correcting Over-Exposure in Photographs. In Proceedings of IEEE Conference on Computer Vision and Pattern Recognition (CVPR), 2010.

5. F. Ding, H. Li, **Y. Cheng**, and W. K. Leow. Medical Volume Image Summarization. In Proceedings of IEEE Workshop on Applications of Computer Vision (WACV), 2009.

6. J. Zhang, **Y. Cheng**, and C. Chen. Low Resolution Gait Recognition with High Frequency Super Resolution. In Proceedings of Pacific Rim International Conference on Artificial Intelligence (PRICAI), 2008.

# List of Figures

# List of Tables

# Chapter 1

# Introduction

## 1.1 Motivation

Many patients suffer from skull deformity congenitally or in accidents. Worldwide, one in 700 children is born with cleft palate [Wro10], i.e., opening of the roof of the mouth, and one in $5,600$ children is born with facial asymmetry [Lit10] (Figure 1.1). In addition, many patients suffer from head and facial injuries that typically result in deformities such as fracture of the skull and jaws. For example, in North America, every year, around 1.58 million people suffer from head and facial injuries (Figure 1.2) due to traffic accidents, work accidents, home accidents, sports injuries, and violence [Wik12, GTH*03]. In Singapore, National University Hospital (NUH) alone receives about 250–350 patients with skull fracture every year.

Skull deformities may lead to unaesthetic facial appearance as well as incomplete functionalities because the muscles and skins attached to a deformed skull are also deformed [LP98]. For example, jaw deformity (Figure 1.1) may affect the movement of the jaws, leading to chewing problem. Orbit (eye socket) deformity (Figure 1.2) may affect the ability of the skull to support the eye ball, which may lead to impaired vision. Nasal deformity may choke the airway and cause breathing difficulty. These problems greatly affect the patients' quality of life and even threaten their lives.

To correct skull deformities and restore the normal appearance of the skull, craniomaxillofacial (CMF) surgery is performed. CMF surgery involves complex operations on the jaws and skull [Ltd06, LP98]. As an example, let us consider a patient whose skull was

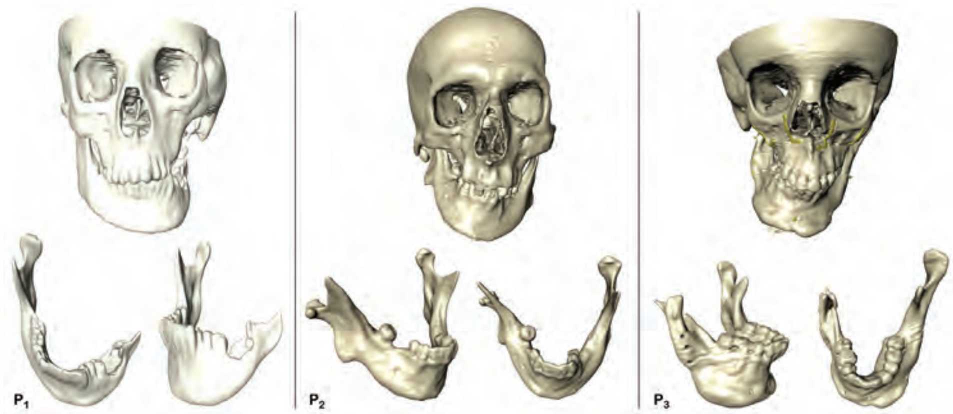


Figure 1.1: Congenital skull asymmetry [ZLES05]. (Top) The skulls are severely deformed congenitally. Large amounts of left-right asymmetry exist in these skulls. (Bottom) Various views of the deformed jaws.

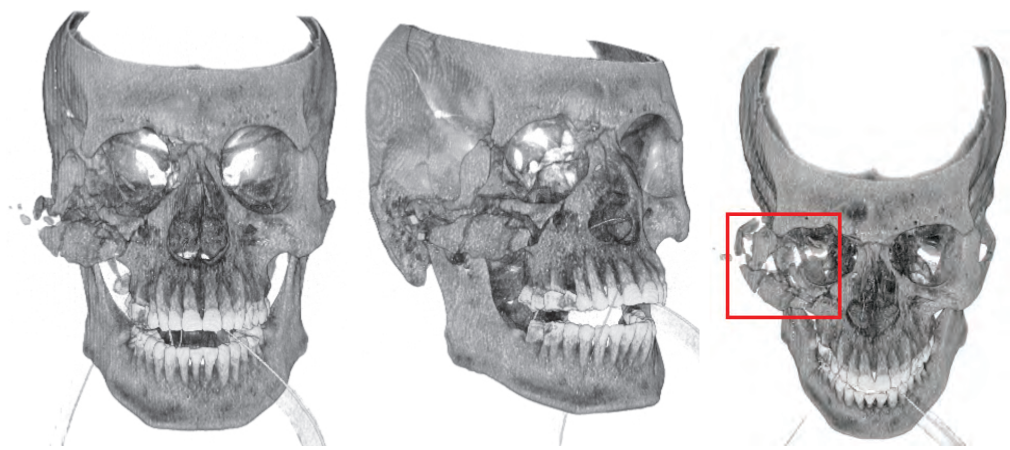

(a) (b) (c)

Figure 1.2: Skull deformity due to accident. The right part of patient's skull is severely fractured in an accident.

severely deformed in an accident (Figure 1.3). The patient's frontal skull was broken into fragments and depressed inward. The right cheek bone was broken into several small fragments and displaced backward. The right eye socket was also broken leaving the eye ball unsupported, and the lower jaw was broken into two parts. To treat this patient, the CMF surgeon in NUH pulled back the usable fragments of the frontal bone and held them in correct positions using metal meshes, put back the cheek bone and held it in the correct position using metal plates, inserted metal meshes into the eye socket floor to provide

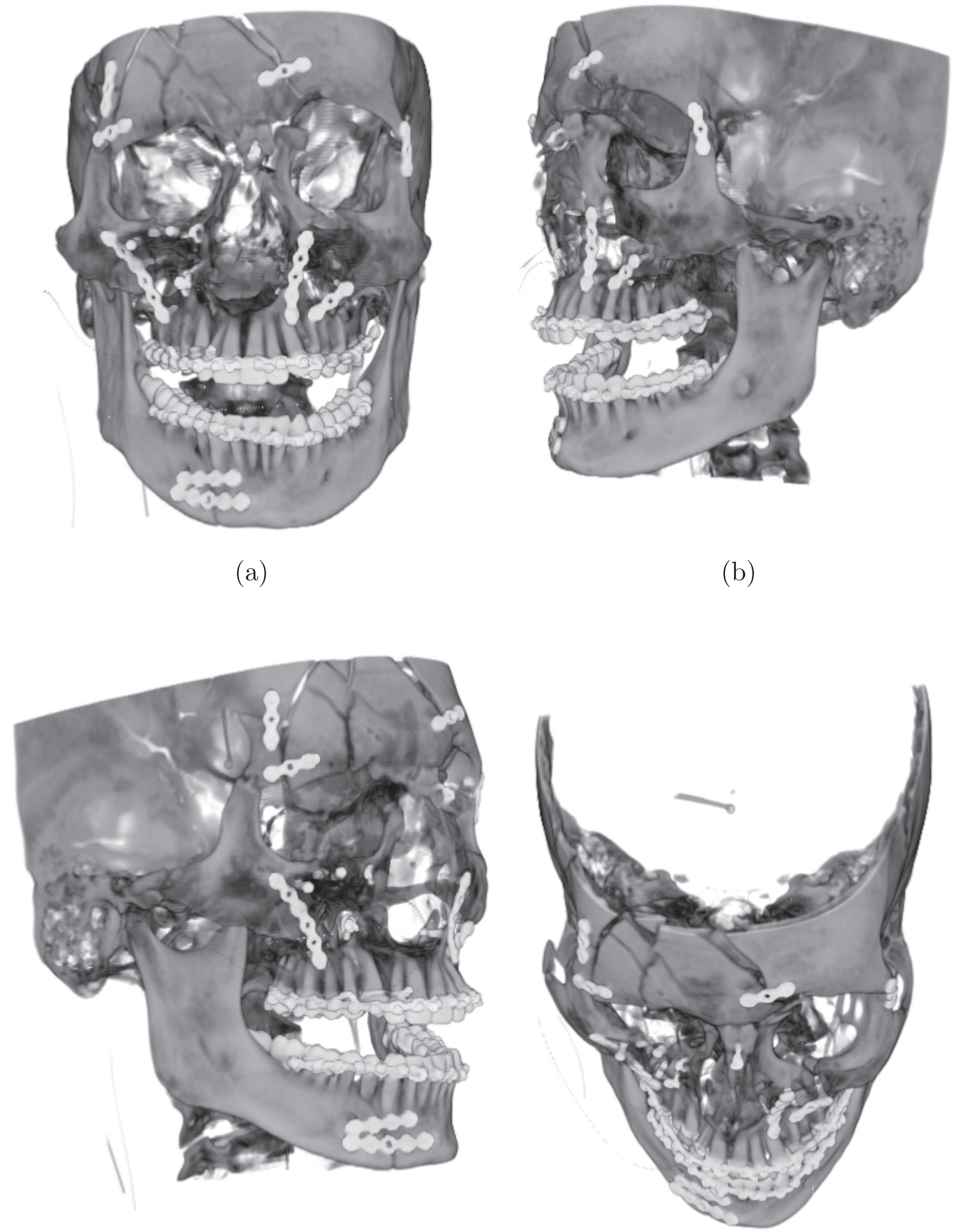

(a) (b) (c) (d)

Figure 1.3: A CMF patient after an unsatisfactory CMF surgery. Fractured bones were not correctly repositioned, causing the right side of the skull to be set back.

support for the eye ball, and used metal plates to hold the two lower jaw fragments in correct position to allow healing (Figure 1.4).

As can be seen, the whole CMF procedure is very difficult and complex. In addition to the procedural complexity, difficulties of performing such a surgery also result from the variation of patients' anatomical structures and the severity of the skull deformation. Therefore, careful pre-operative planning of CMF surgery is crucial for the success of the operation.

In CMF surgery planning, determination of the correct positions and orientations of the fractured bones required to restore a deformed skull is a very difficult procedure because information of the patient's normal skull is usually unavailable to the surgeon. For congenital deformity, the patient is born with a deformed skull. For deformity due to injury, the patient's normal skull before injury is typically unavailable unless he has undergone CT or MRI scan due to other head-related diseases prior to the injury. This difficulty often leads to unsatisfactory surgical results, with permanent functional and cosmetic deformities of a patient's face [Ltd06].

Manual estimation of the correct 3D positions and orientations of bone fragments is inaccurate. An example of an unsatisfactory CMF surgical result is shown in Figure 1.3. The surgery was performed on the same patient shown in Figure 1.4 before he was admitted to NUH. It was performed by an inexperienced CMF surgeon in a foreign hospital. After the surgery, the frontal part of the skull was still depressed, the patient's cheek bone was not properly restored, and the right side of the skull was still sunken.

The same patient was later admitted to NUH, where the surgeon in NUH used a surgery planning and guidance tool Brainlab [GWL99] to plan and guide the surgery. Brainlab is designed to accurately track the bones in the operating theatre so that the bones are accurately placed and fixed at the desired position and orientation. Besides intra-operative guidance, Brainlab provides a tool for planning a CMF surgery. Using the planning procedure, the surgeon first segments the CT images to generate the patient's skull, and identifies the healthy bone fragments. Then Brainlab reflects the fractured bone fragments about a user-defined laterally symmetric mid-plane. The reflected fragments server as the reference model and an estimation of the patient's normal skull. Finally, the surgeon exports the reference model to a DICOM file which is used by the guidance system during operation.

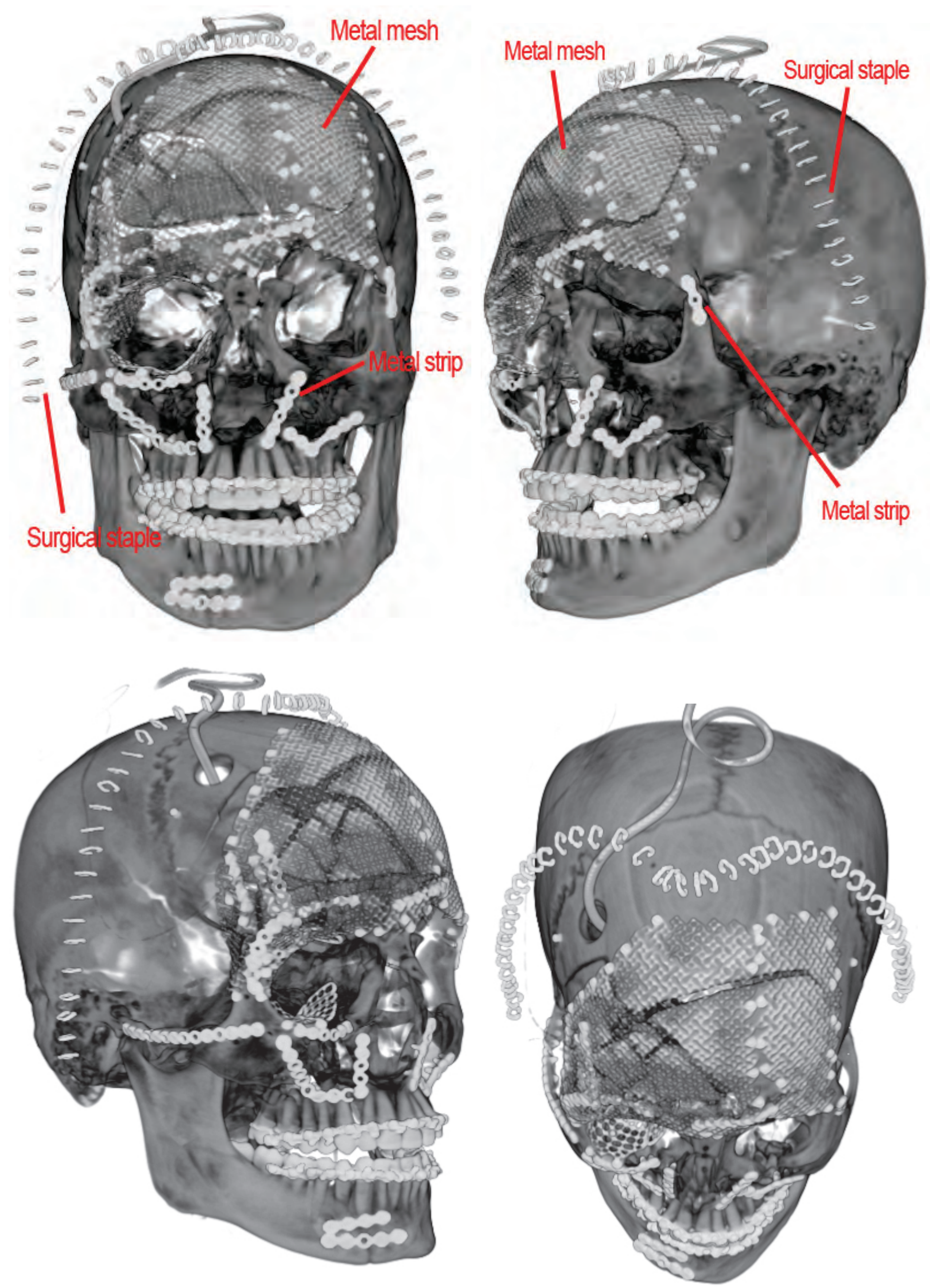


Figure 1.4: A satisfactory CMF surgery result. It correctly restored the skull to normal appearance. Surgical staples were used to close the skin. Metal strips and metal meshes were used to fix the bones.

As can be seen, Brainlab provides very limited support for assisting the surgeon in developing a surgery plan. The reflection method is only applicable to patients with unilateral fracture. For patients with bilateral fractures (Figure 1.3), there is no healthy part on either side of the skull for Brainlab to use. In this case, the surgeon has to segment small pieces of bones on either side, reflect them to the other side and fuse them together into a single piece to serve as the reference. This process is tedious, time-consuming and inaccurate.

There are other computer-aided systems developed to assist the surgeons in surgeries related to the skull [AGG*03a, AGG*03b, AGG*04, BPM*00, BCT*04, CMPB02, CP00, CMC*04, CSP*07, CBRY06, CBRY07, DMCP*06, GZDH01, GZDH03, GIR04, GEH*99, GWL99, KGA*96, KGPG96, KGRG98, KSS09, KRG*99, LCL*02, LCL*03, CTS*10, MSB*06, MSCS03, MSCP04, SVBBC09, SBF*04, Mim, TGG99, TPS*02, XIS*00, XSC*00, XGT05, ZGSZ03, ZLES05]. These systems visualize medical images in 3D and allows the surgeons to manually cut and reposition bones in the 3D models of the patients' skulls. This manual manipulation is tedious and inaccurate, because it is difficult to assess correctness in 3D visualisation. Some systems attempt to simulate the reactions of the body in response to user inputs in real time to provide the user with realistic situations and perception of surgical procedures [AGG*03a, AGG*03b, AGG*04, KSS09, LCL*02, MSB*06, ZGSZ03]. They are suitable for training and planning of simple operations, but not suitable for planning of complex operations such as CMF surgery. Other systems attempt to generate normal skull models of the patient for surgery planning and guidance [CSP*07, DMCP*06, GWL99, LCL*03, CTS*10, Mim, ZLES05]. The surgeons still need to manually work out how to reposition the bones to match the estimated normal skull. Some systems can also estimate and evaluate post-operative facial appearance [CMPB02, CP00, CMC*04, GZDH01, GZDH03, GIR04, KGA*96, KGPG96, KGRG98, KRG*99, MSCS03, MSCP04, SVBBC09, SBF*04, TGG99, XIS*00, XSC*00]. They do not directly assist the surgeon infer the optimal bone repositioning. In summary, existing systems do not provide any means for assisting the surgeon to automatically infer the optimal repositioning of the fractured bones of patients' skulls. The surgeons have to manually explore various options to determine the optimal repositioning of the bones.

In summary, there is no computer-aided system to help surgeons generate CMF surgery plans based on restoration of fractured skulls, and there is no automatic, reliable and accurate method for generating a restored model of a patient from his deformed model.

## 1.2 Research Goal

The goal of this thesis is to develop a procedure for generating a CMF surgery plan for restoring a deformed skull back to normal appearance. Due to the great complexity in different kinds of CMF surgery, this thesis will focus on skull deformities due to trauma.

The input to the procedure is a patient's 3D medical images. From these images, a 3D model of the injured skull called the **deformed model** is generated. The ideal normal state of the patient's skull before injury is called the **normal model**, which is generally unavailable in clinical practice.

A **reference model** is used to provide information about the normal appearance of a skull. This model can be either a 3D model of a single healthy skull or a statistical model of a population of healthy skulls. Theoretically, a statistical model contains more information about the possible variations of normal skulls than a single generic model. However, to build a good statistical model, many normal skull models must be collected. Therefore, as a start, a single normal skull model is used as the reference model. Statistical model will be considered later when enough normal skull models are available for constructing the statistical model.

The output of the method consists of a **restored model** of the patient's skull and a **surgery plan** for obtaining the restored model by repositioning the bones in the deformed model. It tells which bone fragments to reposition, and how to reposition them. The order or applying these repositioning depends on surgeon's decision according to medical considerations. The restored model should be as close to the normal model as possible.

In comparison, some existing systems produce the **reconstructed model** [CSP*07, DMCP*06, GWL99, LCL*03, CTS*10, Mim, ZLES05] from the deformed model based on shape similarity. The detailed shapes of the bones in the reconstructed model are not necessarily the same as those in the deformed model. Although the reconstructed model may be used as a reference guide during actual surgery, the surgeon still needs to manually work out how to reposition the patient's bones to match the reference as given by the reconstructed model.

In summary, the main contributions of this thesis include:

1. Development of a computer-aided procedure for assisting a surgeon in deriving a

surgery plan for restoring a patient's deformed model back to the normal state by bone repositioning (Chapter 4).

2. Development of a method for automatic identification of craniometric planes and landmarks of skulls (Chapter 5).

3. Development of a method for generating the restored model from a patient's deformed model, which is the core algorithm in the proposed procedure (Chapter 6).

With these contributions, CMF surgeons can work out accurate CMF surgery plans. CMF patients would also benefit from these contributions, because accurate surgery plans can potentially improve surgical outcomes and improve patients' life quality.

Before describing the details of the planning procedure and algorithms, this thesis first presents necessary medical backgrounds (Chapter 2) and existing works related to the thesis (Chapter 3). Experimental results and validation of the whole procedure are presented in Chapter 7 followed by conclusion in Chapter 9.

# Chapter 2

# Background

This section provides background knowledge that serves as the basis of further discussions. First, the anatomy of the skull is presented in Section 2.1. Next, two important anatomical planes that define the skull's orientations and anatomical landmarks are discussed in Section 2.2. Next, skull deformities are briefly discussed in Section 2.3. Finally, CMF surgery for correcting skull deformity is described in Section 2.4.

## 2.1 Skull

The skull is a 3D structure consisting of 28 bones that are fused together [SH]. While its general shape is similar for all normal humans, it can vary greatly in size and shape details among different individuals, resulting in the variation of facial appearance of people in different age, gender and ethnic groups.

Excluding three pairs of small auditory ossicles (the small bones in the ear canals transmitting sound), the other 22 skull bones can be divided into two groups, the cranial bones and the facial bones [Wik] (Figure 2.1). 8 cranial bones fuse together to form the cranial cavity that contains and protects the brain. 14 facial bones form the mechanical framework of the face, and provide the attaching sites for the facial muscles. Based on their positions, the 14 facial bones together with the frontal cranial bone are divided into three groups, namely the upper third (frontal bone), middle third (from the frontal bone down to the upper jaw) and lower third (the lower jaw).

Most of the skull bones are fixed. The only exception is the jaw structure that provides

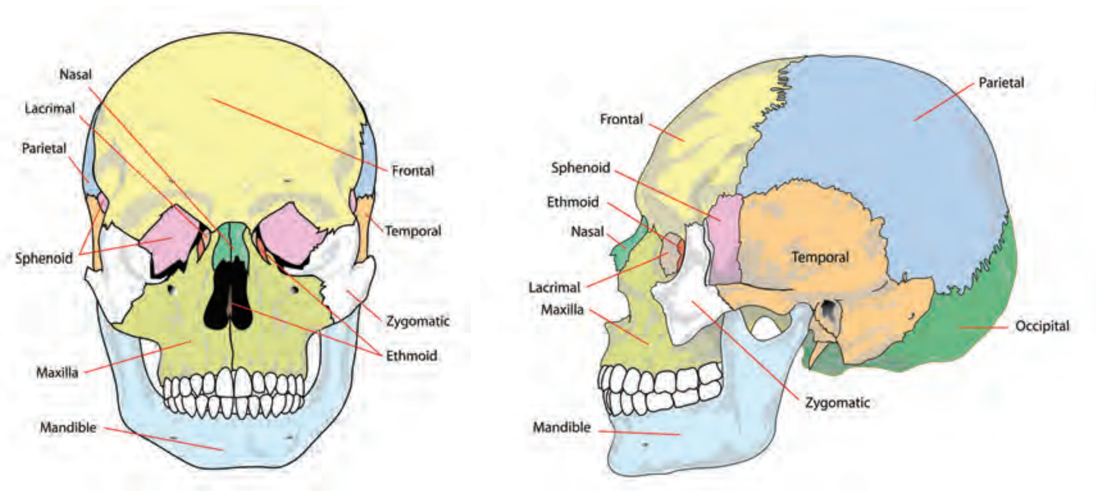


(a) (b)

Figure 2.1: Skull bones [Wik]. A skull consists of 28 bones fused together. (a) Frontal view. (b) Side view.

chewing function. The upper jaw, maxilla, is fused with the zygomatic (cheek) bones and other bones. The lower jaw, mandible, connects to the two temporal bones. The temporomandibular joints between them are the only joints that allow movement of the lower jaw relative to the upper jaw.

## 2.2 Anatomical Planes of the Skull

The Frankfurt Plane (FP) and the Mid-Sagittal Plane (MSP) of a skull (Figure 2.2) are very important in surgery, forensics, and anthropology. They are used to define the three anatomical orientations of the skull. The lateral (left-right) direction is normal to the MSP, the superior-inferior (up-down) direction is normal to FP, and the anterior-posterior (front-back) direction is parallel to the intersection line of FP and MSP. These anatomical orientations, in turn, are used to define craniometric landmarks that are used for pre-operative surgery planning, intra-operative surgery guidance, forensic reconstruction, and anthropological and archaeological studies [CHV99, DMCP*06, GWL99, SH, Tay01, Woo31].

In anatomy, the FP is defined as a plane that passes through the orbitales and the porions [AAG09] (Figure 2.2). The left and right orbitales (Ol, Or) are the lowest points of the lower margin of the left and right orbits (eye sockets). The left and right porions

(Pl, Pr) are the most lateral points of the roofs of the left and right ear canals.

The MSP is defined as a vertical plane that passes the midline of the skull [AAG09]. A number of features lie on the skull's midline. Based on the landmarks used in anatomy [SH] and forensics [Tay01], 6 landmarks are selected to define the midline (Figure 2.2) in our work [CLL11]:

1. The nasal bone suture (NR) is a ridge structure formed by the joint of the left and right nasal bones.
2. The mid-philtrum ridge (MPR) is a ridge structure along the anterior (front) nasal spine towards the upper lip margin.
3. The posterior nasal spine (PNS) is the peak at the posterior end of the median palatine suture, which is the joint of the left and right palatine bones.
4. The vomer ridge (VR) is a ridge structure at the vomer, which forms a part of the nasal septum (the bone that divides the nose into the left and right airways).
5. The foramen magnum center (FMC) is the center of foramen magnum, a circular opening at the bottom of the skull where the spinal cord passes through.
6. The external occipital crest (EOC) is a ridge structure along the midline at the bottom of the skull.

The ridges lie on or close to MSP. For the purpose of defining the MSP, we can use an estimate of the ridge centroid as the ridge landmark point. The landmarks that define the FP are called **FP landmarks**, and the landmarks that define the MSP are called **MSP landmarks** or **midline landmarks** in this thesis.

The skull is divided into the left and right halves by the MSP. The general structure, shape, and craniometric landmarks of the two sides are roughly similar. Therefore, MSP is sometimes considered as the symmetric plane of the skull [DMCP*06]. It is important to note that extensive studies have shown that there is significant asymmetry in the human skull [RRS03, Woo31].

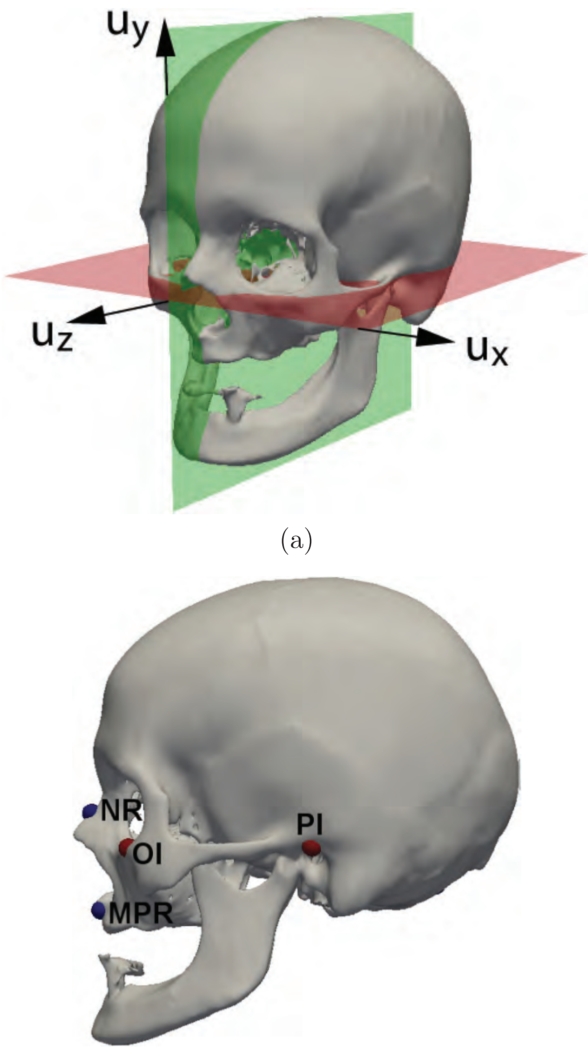


(a) (b) (c) (d)

Figure 2.2: Frankfurt plane, mid-sagittal plane and craniometric landmarks. (a) The Frankfurt plane (FP) is the horizontal (red) plane, and the mid-sagittal plane (MSP) is the vertical (green) plane. The arrows $u_x$, $u_y$, and $u_z$ indicate the left direction, the upward direction, and the frontal direction respectively. (b–d) The red landmarks are the landmarks that define the FP. The blue landmarks are the landmarks that define the MSP.

## 2.3 Skull Deformities

Skull deformities refer to shape distortions of the skull. They may be traumatically acquired in traffic accidents, work accidents, home accidents, sports accidents, or violence, or congenitally malformed at birth. As the proposed research focuses on skull deformities due to injuries, congenitally malformed deformities are omitted in this discussion.

Traumatic deformities to different parts of the skull have different type of features [LP98] (Figure 2.3). Deformities to the upper part of the skull are usually linear cracks or bony depressions over the frontal sinuses, the empty gap in the frontal region of the frontal bone (Figure 2.3).

Severe deformities of the middle part of the facial bone can result in the detachment of the bone, and the bone is thrust backward down the inclined slope of the base of the skull. This will cause a flattened face. For the example in Figure 2.3, the right zygomatic arch, a bony structure formed by the forward extending part of the temporal bone and the side of the zygomatic (cheek) bone, is broken into several small fragments and displaced backward. More dangerously, the fractured and displaced the bones near the airway may close off the airway, which threatens the life of the patient. Moreover, these fractures may cause permanent damage such as compression and folding of the thin bones in the nose and the orbit, which cannot be reconstructed by CMF surgery.

Fractures to the lower part of the skull can occur in many positions of the mandible (lower jaw). They are mainly cracks, displacements and smashes. The mandible of the patient shown in Figure 2.3 is broken into fragments, which are displaced from their original positions.

## 2.4 CMF Surgery

Craniomaxillofacial (CMF) surgery aims to restore a deformed skull back to its normal state. More specifically, its resulting skull should be normal in appearance. In addition, the MSP and FP of the skull should be restored and the whole skull should be laterally symmetric with respect to the restored MSP.

CMF surgery involves very complex operations on the skull bones [LP98, Ltd06]. This section describes the CMF operations that were applied to the patient in Figure 2.3, as

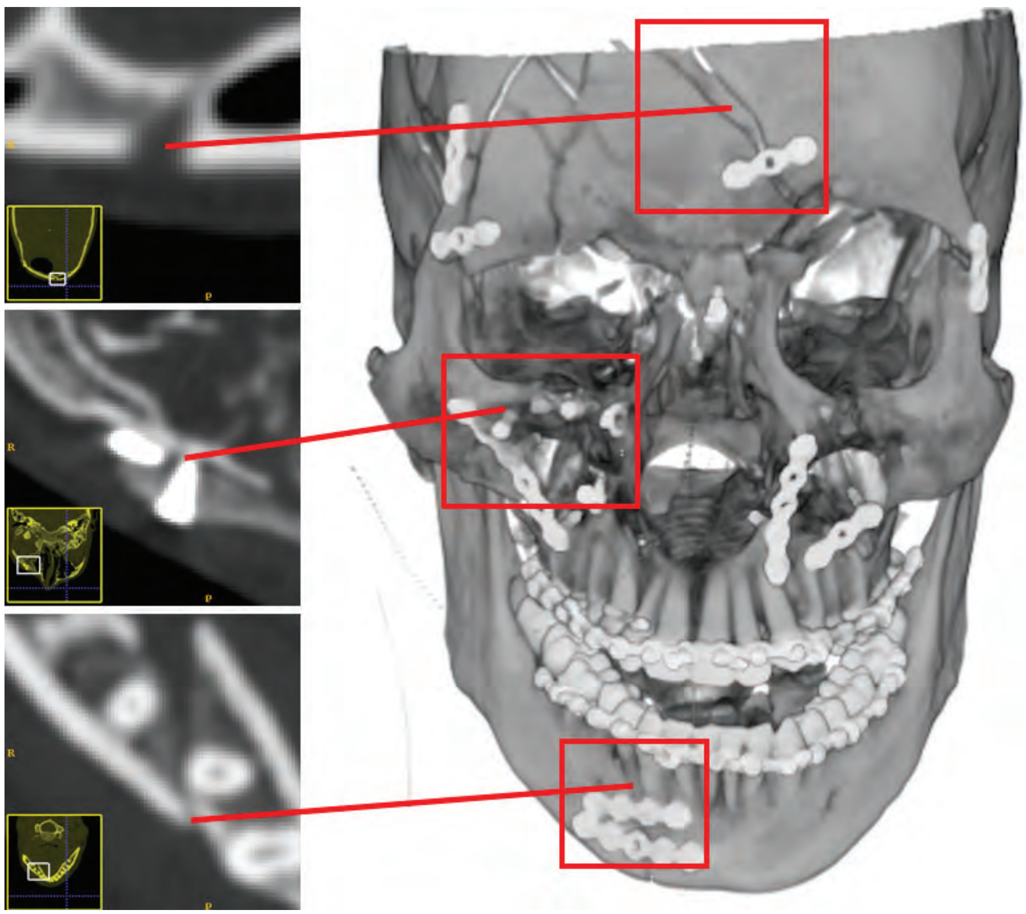

(a) (b)

Figure 2.3: Skull deformities. (a) CT images showing various deformities. (b) Volume rendering of the skull shows the fractures of the bones.

explained by the NUH surgeon who operated on the patient.

Figure 2.4 illustrates the CMF operations on the patient. In the top part of the skull, the fractured frontal bones were located and pulled forward to a new position and a new orientation to restore the normal shape (Figure 2.4, first and second row).

Operations to the middle part of the skull is more complex. The zygomatic (cheek) bone was moved forward and downward, rotated a bit and fixed to the new position using plates, restoring a normal zygomatic arch shape connecting the zygomatic bone and the temporal bone (Figure 2.4, third row). To provide support for the eye balls, a metal mesh was fixed to the lower orbital roof (Figure 2.4, fourth row). In addition, in order to hold the upper jaw, the maxilla, in proper position while healing, metal plates were used to fix the maxilla bone to the zygomatic bones (Figure 2.4, fifth row).

In the lower part of the skull, the surgeon estimated the original positions of the two fractured bone fragments of the lower jaw. Then, he moved them and fixed them at the estimated original positions.

Figure 2.5 shows the result of the CMF surgery. In comparison to the pre-operative state (Figure 2.3), the overall shapes of the post-operative skull were restored to a more normal and symmetric state.

It is worth noting that some bone fragment were not operated on though they were affected by the injury. This was mainly due to clinical considerations. For example, some bones were broken into very small fragments. The position of these small bone fragments had little effect on the overall structure of the resulting skull. In addition, though fractured, some other fragments were not displaced very much (Figure 2.6). They were still close to the correct position, and they also did not affect the overall structure too much. Therefore, these bones were left in the places where they were attached to the skin and muscles and not operated on to reduce unnecessary trauma to the patient.

(1)
(2)
(3)
(4)
(5)

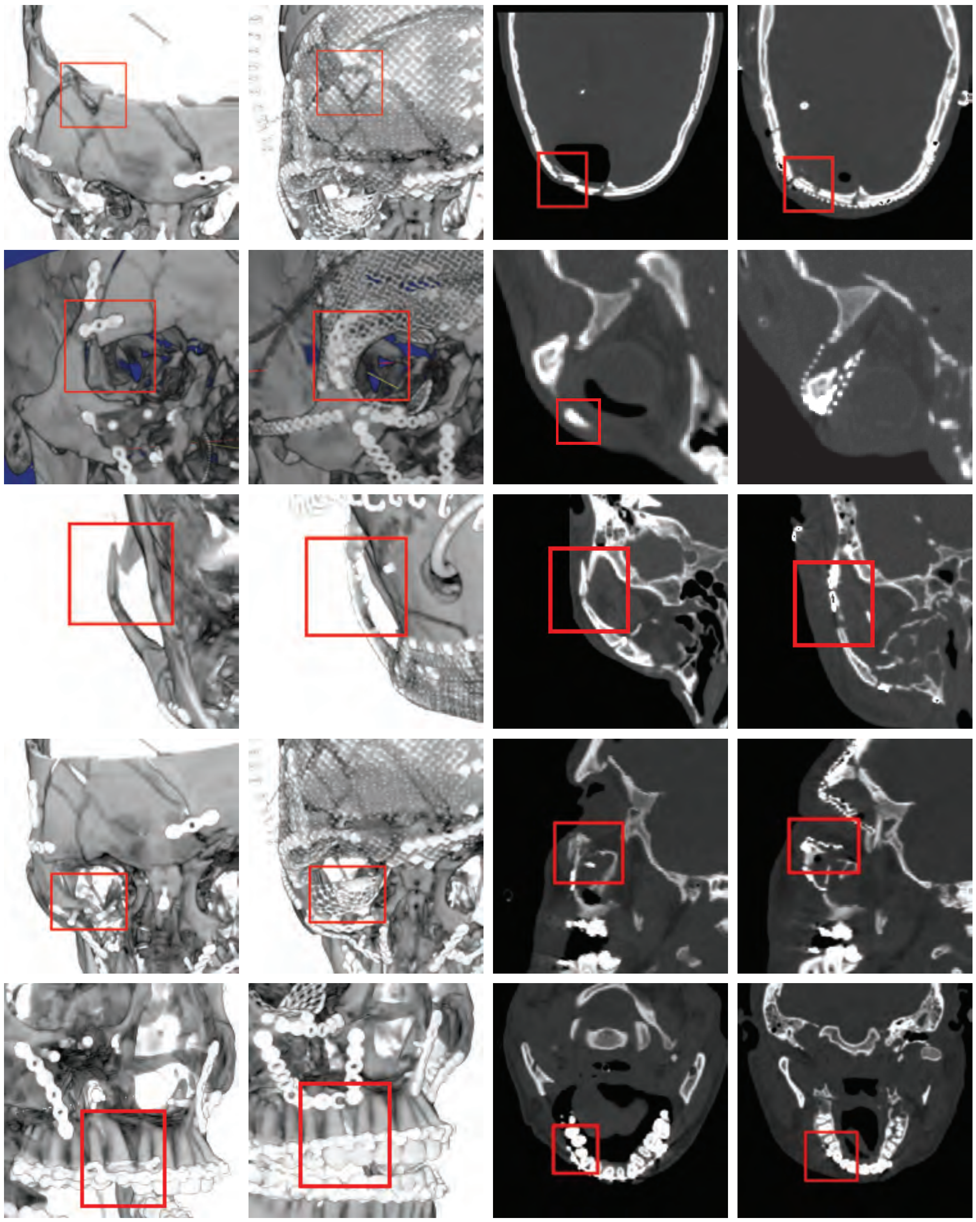

(a) (b) (c) (d)

Figure 2.4: CMF surgery on deformed skull. (a) Volume rendering of pre-operative skull. (b) Volume rendering of post-operative skull. (c) CT slices of the pre-operative skull. (d) CT slices of the post-operative skull. (1) Frontal bone region. (2) Upper right orbital region. (3) Right zygomatic arch region. (4) Lower right orbital region. (5) Maxilla bone.

Figure 2.5: CMF surgery result. Post-operative skull is normal and symmetric.

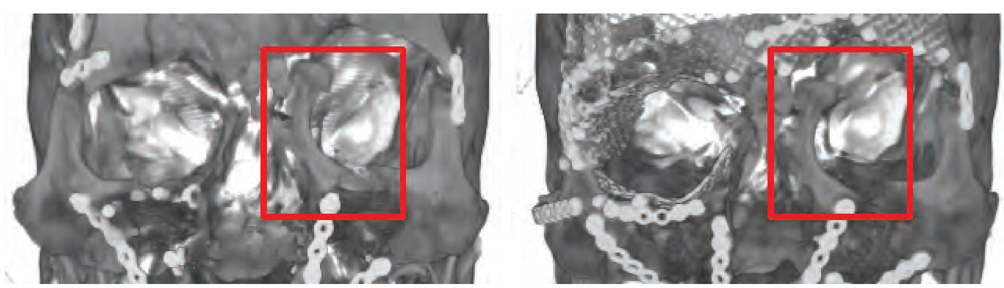

(a) (b)

Figure 2.6: Bone fragment not moved in surgery. The bone in the red box was not moved though it was not in the normal position. (a) Pre-operative state. (b) Post-operative state.

# Chapter 3

# Related Work

As discussed in Section 1.2, there are three main contributions in this thesis, which are summarized below. Their related works are reviewed in the following sections separately.

1. Develop a computer-aided procedure for assisting a surgeon in deriving a surgery plan for restoring a patient's deformed model back to the normal state. Section 3.1 reviews computer-aided systems for skull surgery planning.

2. Develop a method to automatically identify FP and MSP of skulls. Section 3.2 reviews related work on this problem.

3. Develop a method for generating the restored model from a patient's deformed model, which is the core algorithm in the proposed procedure. Section 3.3 reviews existing related methods.

## 3.1 Computer-Aided Systems for Skulls and Jaws

CMF surgery operates on the skull whereas orthodontics surgery operates on the jaws and teeth. As both types of surgeries are related, this section reviews existing computer-aided surgical systems for both of them. These systems are categorized into reactive systems (Section 3.1.1) and predictive systems (Section 3.1.2).

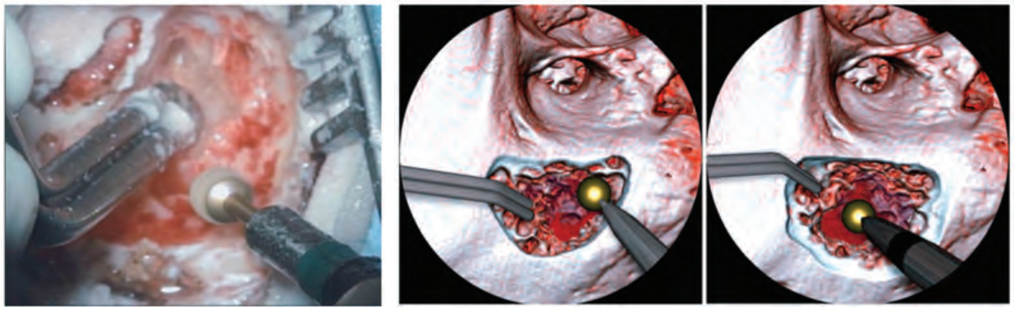

(a) (b)

Figure 3.1: A reactive system that simulates bone removal operation [KSS09]. (a) Typical view in real surgical procedure. (b) Screen shots of the reactive system.

### 3.1.1 Reactive Systems

Reactive systems are real-time systems that attempt to simulate the reactions of the body in response to user inputs [AGG*03a, AGG*03b, AGG*04, KSS09, LCL*02, MSB*06, ZGSZ03]. The user inputs emulate surgical operations such as cutting, drilling, moving, and fixing of bones. The systems simulate body reactions such as change of bone shape, displacements of bones, bleeding, etc. The objective of reactive systems is to provide the user with realistic situations and perception of surgical procedures, through user interactions and simulated reactions of the body.

Reactive systems have been developed for skull surgeries. For example, Kerwin et al. [KSS09] developed a reactive system for simulating the removal of the bone behind the ear. Figure 3.1(a) shows a real image taken in an operation theater. It is the typical view that a surgeon would have during the procedure. The reactive system shown in Figure 3.1(b) aims to provide a realistic feel for the user. To achieve this, it provides the user with virtual tools such as bone drilling tool, irrigation tool and suction tool that emulate real surgical tools, and provides the user with haptic feedback and sound cues of tool usage. The system also simulates the change of bone shape and bleeding in response to drilling in real time to enhance the experience. The system of Agus et al. [AGG*03a, AGG*04, AGG*03b] provides the same user experience. For general CMF surgery, the system of Morris et al. [MSB*06] provides visual and haptic feedback for surgical operations such as drilling, cutting, moving of bone fragments, and attaching of rigid metal plates.

Reactive systems are useful for medical training and pre-operative planning of basic surgical operations. They are not suitable for pre-operative planning of complex surgical procedures such as the whole CMF surgery. To use a reactive system to plan a complex procedure and predict the surgical results, the user would need to go through all the delicate operations in the procedure, which is very tedious and time-consuming.

### 3.1.2 Predictive Systems

Predictive systems attempt to accurately predict surgical results of complex surgical procedures based on predefined or user-specified surgical requirements. Depending on the design of the predictive systems, the user inputs to the systems can consist of surgical requirements like desired facial shape, implant shape, bone cutting position, etc. The surgical results provided by predictive systems can be the resultant skull model or facial surface. The objective of predictive systems is to allow the user to easily explore various surgical options to determine the best surgery plan.

Compared to reactive systems, predictive systems are designed to plan for the entire surgical procedures such as the whole CMF surgery instead of simulating basic surgical operations. In predictive systems, real-time response is not a necessary requirement. Instead, accurate surgery planning and effective assessment of the surgical results are very important.

Predictive simulation systems have been developed for pre-operative planning of orthodontics surgery and surgical implants [CSP*07, DGL*01, TVE*07, VvCM*96]. The system of Verstreken et al. [VvCM*96] allows a surgeon to manually manipulate dental implant model in either 3D or 2D. The system of Dutreuil et al. [DGL*01] allows a surgeon to validate dental implant shape by rendering the 3D data in the view defined by the surgeon. The system of Bettega et al. [BPM*00] allows a surgeon to manually reposition the bones in the upper jaw and perform dental analysis on the model for evaluation. The system of Chapuis et al. [CSP*07] provides a symmetry-based method for generating a reconstructed model that is overlaid onto the deformed model to guide the manual planning of bone repositioning.

Over the last few decades, a lot of systems have been develop for CMF surgery. Most of these systems focus on predicting post-operative facial appearance to assist the surgeon in evaluating the plan as well as facilitate the communication between the surgeon and the patient [CMPB02, CP00, CMC*04, GZDH01, GZDH03, GIR04, KGA*96, KGPG96,

KGRG98, KRG*99, MSCS03, MSCP04, SVBBC09, SBF*04, TGG99, XIS*00, XSC*00]. In addition to predicting face appearance, the system of Gladilin, Zachow et al. [GZDH03] also predicts post-operative facial expressions. Some systems generate reconstructed models of the patient from the deformed ones [CSP*07, DMCP*06, LCL*03, CTS*10, ZLES05]. Commercial systems such as Brainlab [GWL99] and SurgiCase CMF [Mim] also provide partial reconstruction based on symmetry. A few other systems perform restoration of mandible using fracture surface matching [BCT*04, CBRY06, CBRY07].

To the best of the author's knowledge, there is no existing predictive system that generates restored skull model from deformed skull model. This thesis proposes a computer-aided procedure for assisting a surgeon in deriving a surgery plan by generating a restored model.

## 3.2 FP and MSP Identification

There is currently no related automatic method for identifying FP. Existing methods require the user to manually mark landmark points of FP on the skull and then fit a plane over the landmark points [GWL99, PG96]. This straightforward approach requires an experienced user to accurately locate the landmark points.

There are existing methods for semi-automatic identification of MSP [SOGB*09, DMCP*06]. In the work of [DMCP*06], two methods were proposed. The first method requires the user to indicate the points on the MSP and/or laterally symmetric points on both sides of the skull. Then, it fits a plane over the points as the MSP. The second method requires the user to indicate laterally symmetric parts on both sides of the skull. Then, it determines the mirror reflection plane between the left and right parts, which is regarded as the MSP.

The method of [SOGB*09] requires the user to indicate the regions that contain the landmark points that define the MSP and a transverse plane that is orthogonal to MSP. Then, it detects extreme points in these regions as landmark points, and fits two orthogonal planes through these points. The fitted vertical plane is regarded as the MSP.

Identifying MSP based on lateral symmetry is inaccurate because extensive anthropological studies show that there is significant lateral asymmetry in the human skulls [RRS03, Woo31]. Another shortcoming of existing methods is the manual marking of landmark points or regions on the skull. This approach is tedious and it requires an

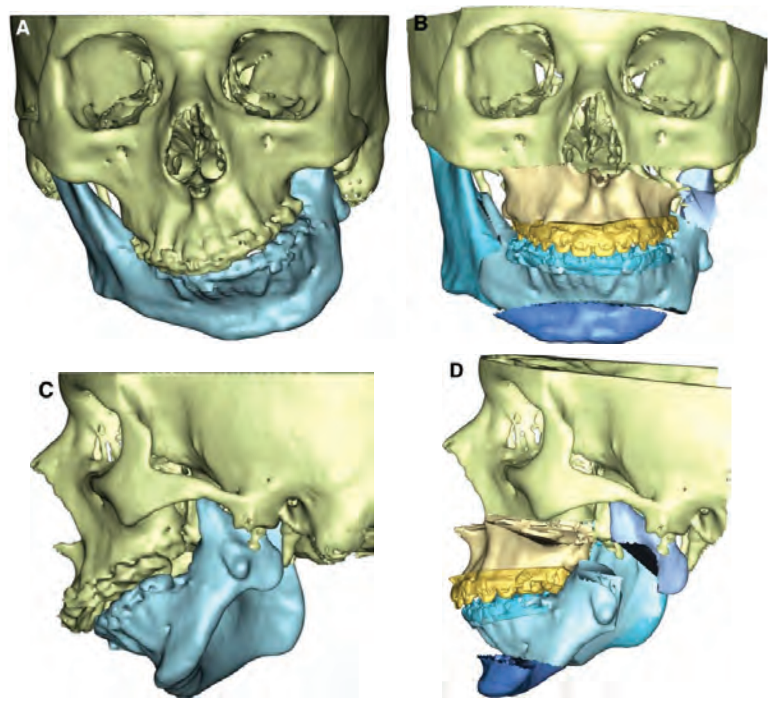


Figure 3.2: Manual restoration [XGT05]. (a, c) Deformed model. (b, d) Restored model after cutting and repositioning of bones.

experienced user to locate the landmarks accurately.

In contrast, this thesis presents a fully automatic method that automatically robustly, and accurately identifies FP, MSP and craniometric landmarks of human skulls.

## 3.3 Restoration and Reconstruction

Model restoration seeks to restore the deformed model back to its normal state by repositioning the bones in the deformed model. Model reconstruction, on the other hand, derives an estimate of the normal model from the deformed model by shape similarity. There are currently two restoration approaches, namely manual manipulation and fracture surface matching, and three reconstruction approaches, namely symmetry-based reconstruction, geometric reconstruction, and statistical reconstruction. The following sections discuss these methods in increasing order of complexity.

### 3.3.1 Manual Manipulation

Manual manipulation methods display the 3D model of a patient's skull in the computer monitor and allow the surgeon to virtually cut and reposition the bones in the 3D model [BPM*00, CMPB02, CP00, CMC*04, CSP*07, DMCP*06, GZDH01, GZDH03, GIR04, GEH*99, GWL99, KGA*96, KGPG96, KGRG98, KSS09, KRG*99, LCL*03, CTS*10, MSCS03, MSCP04, SBF*04, SVBBC09, Mim, TGG99, TPS*02, XIS*00, XSC*00, XGT05, ZLES05]. They provide user interfaces for the surgeon to operate on 3D models of bones and manually determine the surgery plan. For example, Figure 3.2 shows a planning system based on manual manipulation [XGT05]. The system allows the user to virtually cut and displace bones, and it renders the resulting skull shape for visual examination. Some systems provide additional features to assist the surgeon in manual manipulation. These features include anatomical measurements such as relative position and angle between anatomical landmarks [BPM*00, CMPB02, CSP*07, TPS*02, XGT05], collision detection [GEH*99, TPS*02], post-operative facial tissue prediction [CMPB02, CP00, CMC*04, GZDH01, GZDH03, GIR04, KGA*96, KGPG96, KGRG98, KRG*99, MSCS03, MSCP04, SVBBC09, SBF*04, TGG99, XIS*00, XSC*00] and generation of reconstructed model [CSP*07, DMCP*06, GWL99, LCL*03, CTS*10, Mim, ZLES05]. They facilitate the planning procedure and improve manual manipulation accuracy.

Manual manipulation method is relatively easy to implement. It gives the surgeon maximum control over how the bones in the deformed model should be repositioned. Some systems provide additional features to assist the surgeon. Nevertheless, it is quite tedious for the surgeon to manually manipulate bones in 3D in order to explore various possibilities. It also requires an experienced surgeon to visually assess whether the restored model is satisfactory.

### 3.3.2 Symmetry-Based Reconstruction

Symmetry-based methods produce a reconstructed model based on left-right symmetry of the human skull [CSP*07, DMCP*06, GWL99, LCL*03, CTS*10, Mim, WYLL11]. These methods require the user to indicate the healthy regions of the deformed model (Figure 3.3, green part). Then, they reflect the healthy parts with respect to the mid-sagittal plane (MSP). This reflection (Figure 3.3, orange part) serves as an estimation of the normal state

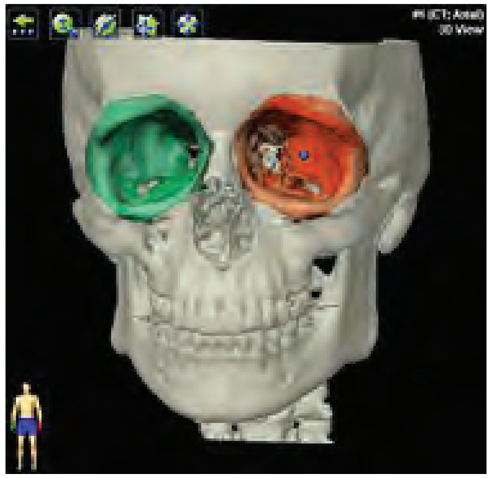

Figure 3.3: Symmetry-based reconstruction [GWL99]. The skull model is colored white. The green region on the right side is reflected and overlaid onto the left side as the orange region.

of the deformed parts, and is used to generate the reconstructed model. Symmetry-based method is applied in Brainlab [GWL99], a leading CMF surgery planning system used in NUH. Brainlab does not reconstruct the whole skull model. Instead, it just reflects the healthy parts identified by the user, which are then regarded as the reference for actual surgery. Thus, Brainlab can be regarded as producing a partially reconstructed model. As discussed in Section 1.1, in case of bilateral fractures, this reflection approach is not directly applicable.

In symmetry-based methods, correct identification of MSP is essential to the accuracy of reconstruction. Semi-automatic methods have been designed to identify MSP [CSP*07, DMCP*06, GWL99, CTS*10]. In the work of [DMCP*06], two methods were proposed. The first method requires the user to indicate the points on the MSP and/or laterally symmetric points on both sides of the skull (Figure 3.4(a)). Then, it fits a plane over the points as the MSP. Brainlab uses a similar method to identify MSP. The surgeon indicates MSP points on CT slices, and then Brainlab fits the MSP to them. The second method requires the user to indicate laterally symmetric parts on both sides of the skull using a virtual brush (Figure 3.4(b)). Then, it determines the mirror reflection plane between the left and right parts, which is regarded as the MSP.

Symmetry-based reconstruction uses the natural approximate left-right symmetry of the human skull. It requires the presence of healthy bones to reconstruct the fractured

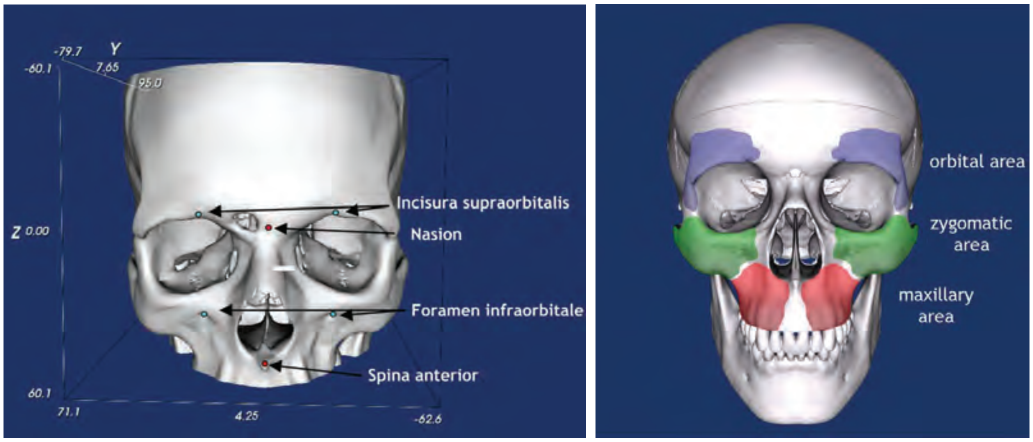


(a) (b)

Figure 3.4: Semi-automatic methods for identifying the MSP [DMCP*06]. (a) Red landmarks are the MSP landmarks given by user, and the blue landmarks given by user are symmetric to MSP. (b) Regions with the same color are the symmetric regions indicated by user.

parts on the opposite side of the skull. When both sides of the skull are fractured, which is common in impact injuries, this method cannot be applied.

### 3.3.3 Geometric Reconstruction

Geometric reconstruction methods use generic shape models to estimate the normal shape of the deformed part [BSMG09, GMbW04, WYLL11]. They deform the generic model to match the healthy parts of the deformed model. Then they apply a generic shape function to interpolate the fractured or missing parts to generate the reconstructed model. For example, [GMbW04] applies thin-plate spline to deform a reference model and register it to the model with missing parts (Figure 3.5(a)). After registration, the missing parts are filled in by the registered reference model (Figure 3.5(d)) .

Geometric reconstruction is relatively simple to apply. However, detailed shapes of human skulls vary significantly across different gender, age and ethnic groups. Selection of a reference model in the same gender, age and ethnic group is essential for reconstruction accuracy [GMbW04]. The lack of similar reference model will affect the reconstruction result. In addition, geometric reconstruction uses the correlation between the healthy parts and the deformed parts, which is weak for severely deformed model. In some severely deformed models, the whole frontal face is deformed (Figure 1.3), leaving only the back

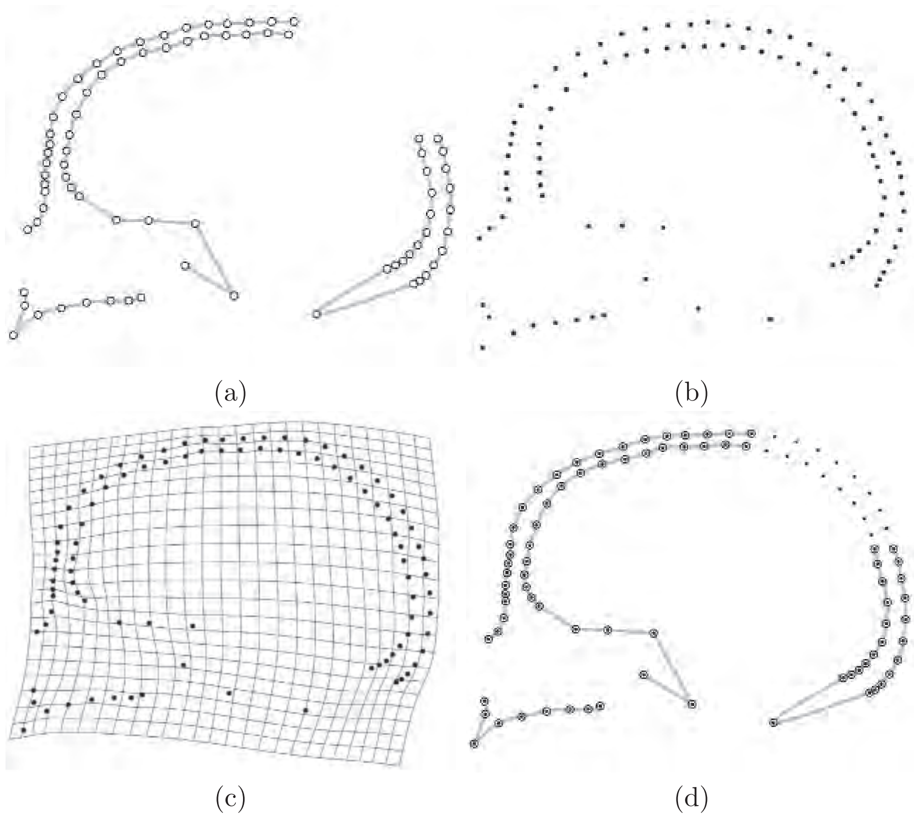

Figure 3.5: Geometric-based reconstruction [GMbW04]. (a) A model with missing parts. (b) A reference model. (c) Thin-plate spline deformation of (b) registered to (a). (d) Reconstructed model with the missing parts filled in by the registered reference model.

of the skull healthy. The correlation between the back portion and the frontal portion is weak. Therefore, in such cases, geometric reconstruction generates a model whose frontal face is close to the reference model instead of the patient's normal shape.

### 3.3.4 Statistical Reconstruction

Statistical reconstruction methods match a statistical reference model to the healthy parts of a deformed model and use the matched statistical model to infer the fractured parts of the deformed model [BSMG09, Phi05, LAV09, ZLES05]. For example, given a set of training samples of healthy mandibles, the method in [ZLES05] applies Principal Component Analysis (PCA) to compute the mean shape and the principal variation modes of the training samples. Next, it computes the principal variation modes that best match the statistical model to the healthy parts of a patient's deformed model. Finally, it uses the

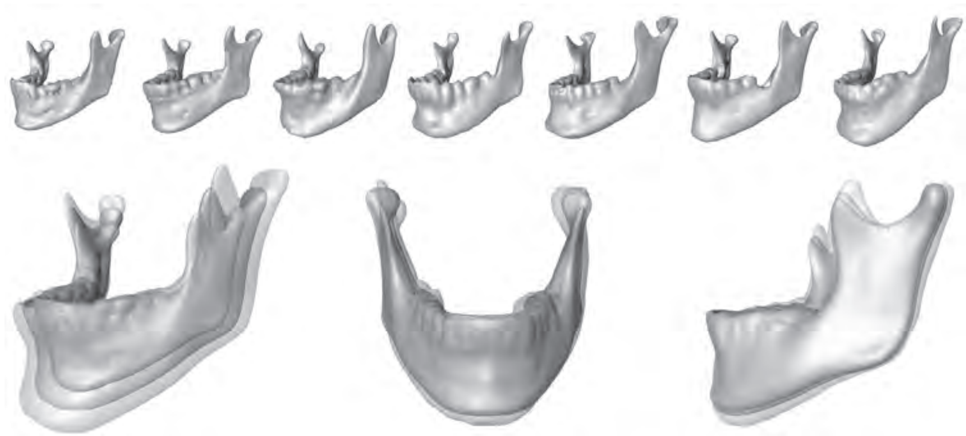

Figure 3.6: Statistical mandible shape model [ZLES05]. (Top) Training samples. (Bottom) Three main variation modes of the statistical model.

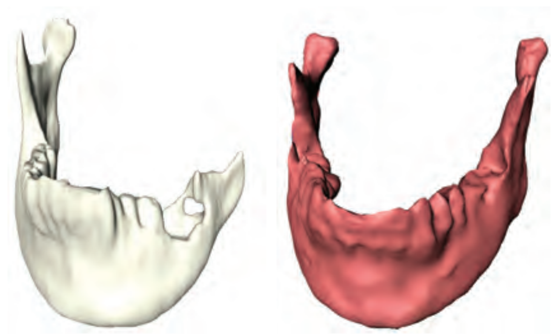

(a) (b)

Figure 3.7: Statistical reconstruction of mandible [ZLES05]. (a) Model of patient's deformed mandible. (b) Reconstructed model.

computed principal variation modes to generate a reconstructed model from the statistical model.

Statistical reconstruction overcomes the limitation of geometric reconstruction by capturing normal variations of human skulls in the statistical reference model. It can potentially produce a reconstructed model that is close to the normal model of a patient, provided that a good match is obtained between the patient's deformed model and the statistical reference model. However, one potential limitation is that the construction of the statistical reference model requires a large amount of training samples of healthy skull models, preferably categorized into various gender, age, and ethnic groups. Their reconstruction accuracy depends on how well the statistical model captures the normal shape variation of the patients' normal model. In the case that such normal shape variation is not

(a) (b)

Figure 3.8: Fracture surface matching method [CBRY06]. (a) Cross section of a bone that is fractured into two fragments. (b) The fragment on the left is repositioned at the correct position and orientation relative to the one on the right.

(a) (b)

Figure 3.9: Fracture surface matching method applied to multiple fracture case [BCT*04]. (a) Cross section of a bone that is fractured into multiple fragments. (b) Restored model computed by repositioning the fragments at their correct relative positions and orientations.

adequately captured, only the mean shape of the statistical reference can be used. Then, statistical reconstruction becomes geometric reconstruction. Insufficient training samples will affect the reconstruction result. In addition, statistical reconstruction methods are also based on the correlation between healthy parts and deformed parts. For severely deformed models with only a small healthy region, statistical methods can only generate a model which is close to the training samples' mean shape in the deformed regions.

### 3.3.5 Fracture Surface Matching

Fracture surface matching methods reposition fractured bones by determining their correct relative positions and orientations based on shape complementarity of adjacent fracture surfaces. Shape complementary is measured by the mean distance between the corresponding points of two adjacent surfaces. These methods first compute the rigid transformations that bring the adjacent fracture surfaces into registration that maximizes shape complementarity. The rigid transformations determine the relative positions and orientations of two adjacent bone fragments. This method is applied in the work of Bhandarkar et al. [BCT*04, CBRY06, CBRY07] to restore mandible fractures. It uses an algorithm inspired by RANSAC to determine a subset of corresponding vertices of the two fracture surfaces that best align them. After this initial alignment, it further refines the fracture surface alignment by ICP algorithm [BM92] over all the vertices. It then applies the transformation between the two fracture surfaces to restore the mandible shape (Figure 3.8).

In cases where multiple fractures occur, more that one pair of fracture surfaces exist. Determining the correspondence of adjacent fracture surfaces is also important. The work in [CBRY06] solves this problem using graph method. It formulates the problem as a maximum weighted graph matching problem. Each fracture surface corresponds to a node in the graph. The edge between two nodes is assigned a weight measuring the shape complementarity of the two fracture surfaces of the two nodes. These nodes and weighted edges form the graph. A matching of a graph is a set of edges such that no two edges are incident on the same vertex. Thus a matching gives the corresponding fracture surface pairs. Edmonds's algorithm [Edm65] is applied to solve the problem in polynomial time (Figure 3.9).

In [WYLL11], Zhao et al. proposed a similar method for automatic assembly of fragmented skulls in archaeological and anthropological applications. This method represents the skull by its outer surface with zero thickness instead of a solid model. So a fracture is represented by a curve instead of a surface. This method first uses ICP algorithm to roughly register the skull fragments to a reference skull. Then, it refines the result by registering neighboring fragments based on the matching of their fracture curves.

Fracture surface matching methods are also applied to solve similar problems in other research fields, for example, archeological assembling of fractured skulls and other objects. The method of Yin et al. [YWML11] assembles skull surface scans by matching the slippage features and spin-image descriptors extracted from fracture curves. To assemble general fractured objects, Huang et al. [HFG*06] match surface features that are extracted from neighboring fractured surfaces using level set method, and Winkelbach et al. [WW08] maximize surface contact of neighboring fragments.

In contrast to the methods discussed in the previous sections that produce only reconstructed models, fracture surface matching methods produce restored models by computing the positions and orientations of the fractured bone fragments. However, these methods require the features on the fracture surfaces to be well preserved so that accurate shape complementarity can be computed. In the case of impact injuries, the fracture surfaces may abrade each other obliterating their surface features and destroying shape complementarity [LP98]. In this case, fracture surface matching becomes inaccurate and unsuitable for surgery planning. So far, it has been applied only to the planning of mandible restoration [BCT*04, CBRY06, CBRY07]. In contrast, this thesis presents an automatic, reliable and accurate method for generating the restored model from a fractured deformed model.

## 3.4 Summary

Many computer-aided systems have been developed for CMF planning. Table 3.1 summarizes the existing systems. Reactive systems are real-time systems that attempt to simulate the reactions of the body in response to user inputs. They are more suitable for surgery training than surgery planning. Predictive systems attempt to accurately predict surgical results of complex surgical procedures based on predefined or user-specified surgical requirements. They are suitable for planning complex CMF surgery. Most of them generate post-operative facial appearance, while a few of them also generate facial expressions. Some systems generate reconstructed model that can be used to guide manual planning. Several systems can generate surgery plan for mandible restoration.

Existing methods for FP and MSP identification are summarized in Table 3.2. At present, there is no related method for automatic identification of FP. Existing methods require the user to manually mark landmark points of FP on the skull and then fit a plane over the landmark points. This straightforward approach requires an experienced user to accurately locate the landmark points. On the other hand, existing automatic methods for identifying MSP look for a symmetric plane of the skull. Unfortunately, this approach is inaccurate because extensive anthropological studies show that there is lateral asymmetry in the human skulls. In anatomy, MSP is in fact defined not as a laterally symmetric plane of the skull but as a vertical plane that passing through the midline of the skull, and the midline is defined by specific landmarks on the skull. There is no automatic, accurate,

Table 3.1: Comparison of computer-aided systems for skulls and jaws.

| System Type | Body Reaction | Face Appearance | Reconstruction | Restoration | |
|---|---|---|---|---|---|
| | | | | Mandible | Skull |
| Reactive System | [AGG*03a, AGG*03b, AGG*04, KSS09, LCL*02, MSB*06, ZGSZ03] | Nil | Nil | Nil | Nil |
| Predictive System | Nil | [CMPB02, CP00, CMC*04, GZDH01, GZDH03, GIR04, KGA*96, KGPG96, KGRG98, KRG*99, MSCS03, MSCP04, SVBBC09, SBF*04, TGG99, XIS*00, XSC*00] | [CSP*07, DMCP*06, GWL99, LCL*03, CTS*10, ZLES05, Mim] | [BCT*04, CBRY06, CBRY07] | Proposed procedure (Chapter 4) |

Table 3.2: FP & MSP identification methods.

| Plane | Semi-automatic | Automatic |
|---|---|---|
| Frankfurt Plane | [GWL99, PG96] | Proposed algorithm (Chapter 5) |
| Mid Sagittal Plane | [SOGB*09, DMCP*06] | Proposed algorithm (Chapter 5) |

and robust method for identifying FP, MSP of skulls.

Existing restoration and reconstruction methods are summarized in Table 3.3. Manual manipulation methods display 3D model of the patient's skull in the computer monitor and allow the surgeon to virtually cut and reposition the bones in the 3D model to generate restored model. They are relatively easy to implement, and give the surgeon maximum control over how the bones in the deformed model should be repositioned. As a result, bone repositioning is planned by the surgeon manually, which can be very tedious, time-consuming, and inaccurate.

Reconstruction methods generate reconstructed model to estimate the normal model based on the correlation between the healthy parts and the fractured parts. Symmetry-based methods reflect the healthy parts of a deformed model about the symmetry plane and use the reflected parts as estimates of the normal shapes of the fractured parts. They do not require any reference model. But they require the presence of healthy symmetric parts to reconstruct the fracture parts on the opposite side of the skull. When both sides of the skull are fractured, which is common in impact injuries, these methods cannot be applied. Geometric reconstruction methods register a reference model to the healthy parts of a deformed model and use the registered reference model to estimate the normal shapes of the fractured parts. These methods do not require the presence of healthy symmetric parts. Instead, they use a single reference model to generate the reconstructed model. Their reconstruction accuracy depends on the similarity between the reference model and the normal model, and the strength of the correlation between the healthy parts and deformed parts. Statistical reconstruction methods overcome the limitation of geometric reconstruction by matching a statistical reference model to the healthy parts of a deformed model and use the matched statistical model to infer the fractured parts of the deformed model. They require a statistical model, the construction of which requires a large amount of training samples of healthy skull models. Their reconstruction accuracy depends on how well the statistical model captures the normal shape variation of the patient's normal model. In the case that such normal shape variation is not adequately captured, only the mean shape of the statistical reference can be used. Then, statistical reconstruction becomes geometric reconstruction. Moreover, similar to geometric reconstruction methods, statistical reconstruction methods relies on the correlation between the healthy parts and the deformed parts.

Fracture surface matching methods reposition fractured bones by determining their correct relative positions and orientations based on shape complementarity of adjacent fracture surfaces. They do not require any reference models or the presence of healthy parts in the deformed model. Instead, they produce the restored model by computing the correct positions and orientations of the fractured bone fragments. However, they require the features of fracture surfaces to be well captured in the deformed model. In the case of impact injuries, where the fracture surfaces abrade each other destroying shape complementarity, fracture surface matching methods become inaccurate.

In conclusion, there is no existing predictive system that provides assistance for generating a CMF surgery plan based on restoration of fracture skull, there is no method for automatic identification of FP and MSP, and there is no automatic, reliable and accurate method for generating the restored model of a patient's skull from his/her deformed model. These are the focuses and main contributions of this thesis.

Table 3.3: Comparison of restoration and reconstruction methods.

| Method | Citations | Approach | Bone repositioning | Reference model | Need healthy parts | | Impact injury |
|---|---|---|---|---|---|---|---|
| | | | | | Symmetric | Non-symmetric | |
| Manual manipulation | [BPM*00, CMPB02, CP00, CMC*04, CSP*07, DMCP*06, GZDH01, GZDH03, GIR04, GEH*99, GWL99, KGA*96, KGPG96, KGRG98, KSS09, KRG*99, LCL*03, CTS*10, MSCS03, MSCP04, SVBBC09, SBF*04, Mim, TGG99, TPS*02, XIS*00, XSC*00, XGT05, ZLES05] | Restoration | Yes | No | No | No | Yes |
| Symmetry-based reconstruction | [CSP*07, DMCP*06, GWL99, LCL*03, CTS*10, Mim, WYLL11] | Partial reconstruction | No | No | Yes | NA | Yes |
| Geometric reconstruction | [BSMG09, GMbW04, WYLL11] | Reconstruction | No | Single | No | Yes | Yes |
| Statistical reconstruction | [BSMG09, Phi05, LAV09, ZLES05] | Reconstruction | No | Statistical | No | Yes | Yes |
| Fracture surface matching | [BCT*04, CBRY06, CBRY07] | Restoration | Yes | No | No | No | No |
| Proposed algorithm (Chapter 6) | | Restoration | Yes | Single or statistical | No | Yes | Yes |

# Chapter 4

# Computer-Aided CMF Surgery Planning Procedure

The proposed computer-aided CMF surgery planning procedure consists of several important stages. An overview of the procedure and how the surgeon is involved are presented in Section 4.1. The proposed procedure is compared with the procedure provided by a commercial software iPlan®(Brainlab, Munich, Germany). The proposed procedure uses mesh models of skull bones, which are segmented and constructed from CT images. Section 4.2 presents details of the segmentation and model construction stage.

## 4.1 Planning Procedure

The proposed computer-aided CMF surgery planning procedure takes CT images of a patient's skull as input and generates a surgery plan for restoring the patient's skull. It consists of 6 stages (Figure 4.1)

In the first stage, the surgeon applies software tools to segment and construct a 3D model of the patient's skull from CT images (Figure 4.2(a)). The skull model consists of separate 3D meshes, one for each bone fragment in the skull (Figure 4.2(b)). In practice, the surgeon may segment only the bones that need to be repositioned in the surgery as an individual mesh, while all other unfractured, undisplaced ("fixed") bones are segmented as a single mesh. In general more bone fragments could be segmented so that the surgeon can explore various surgical options. Details of this stage are presented in Section 4.2.

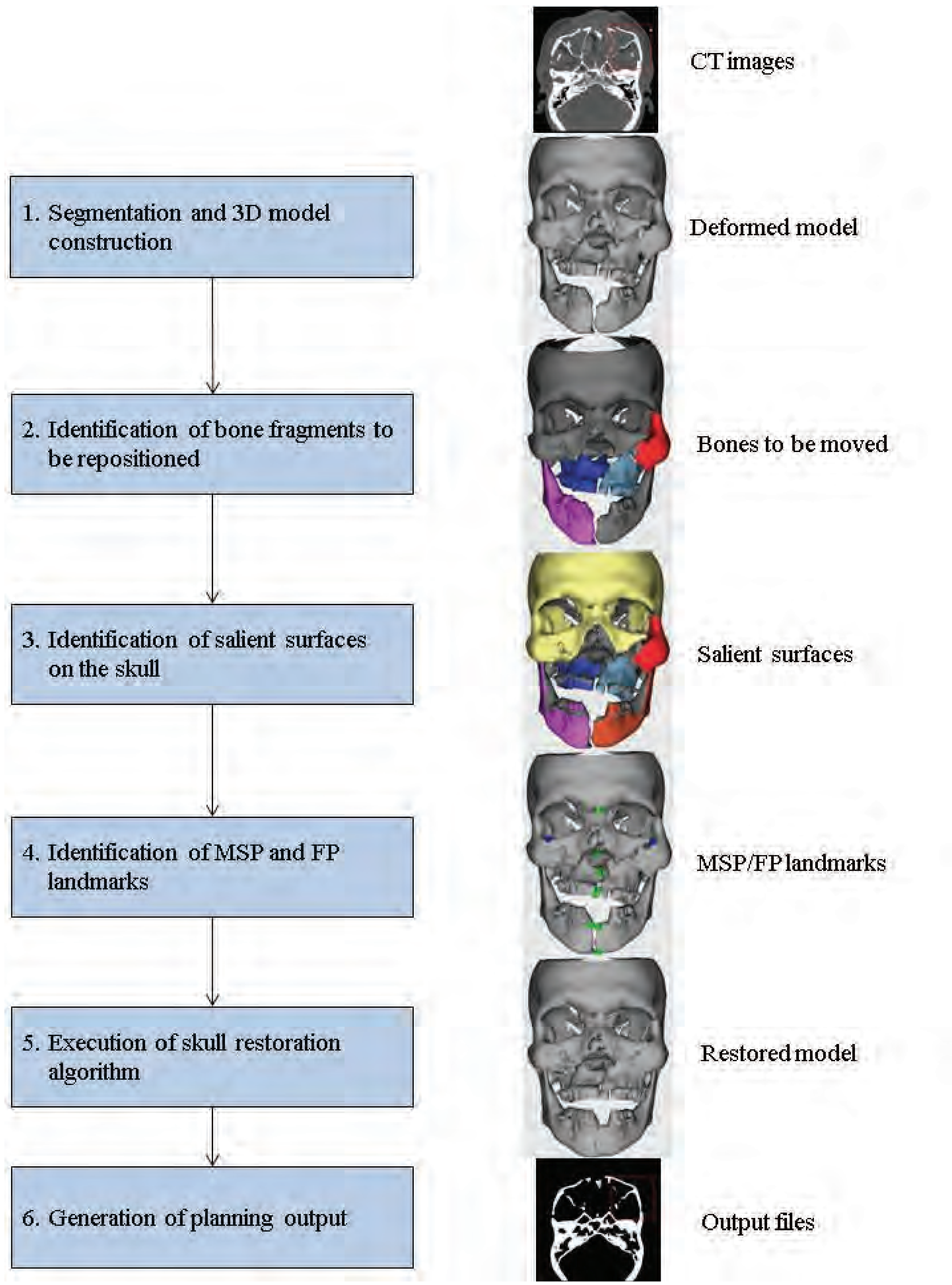


Figure 4.1: Flow diagram of the proposed computer-aided CMF surgery planning procedure.

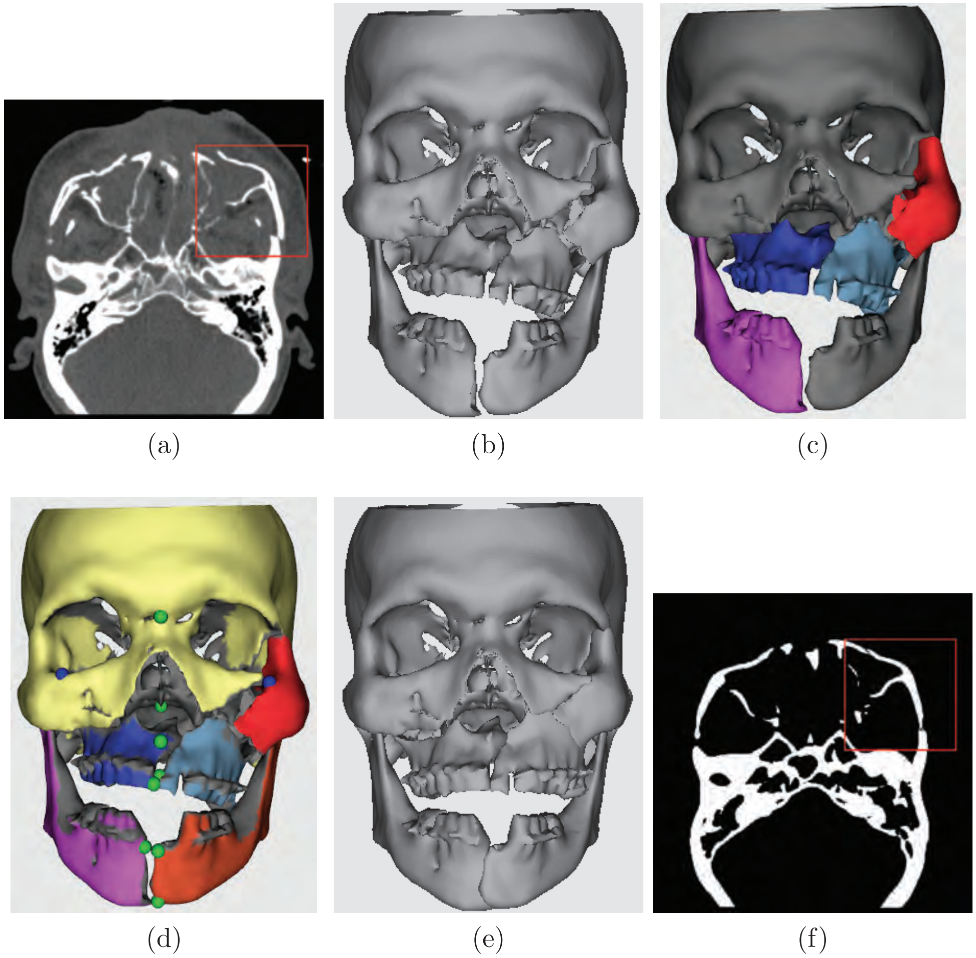


Figure 4.2: Results of each stage of the planning procedure. (a) Input CT. (b) Patient's deformed model generated using CT images. (c) Bone fragments to be repositioned (colored). (d) Identified salient surfaces (colored surfaces), MSP landmarks (green balls), and FP landmarks (blue balls). (e) Restored Model generated by the skull restoration algorithm. (f) Synthesized CT of the restored model.

In the second stage, the surgeon indicates the bone fragments that need to be repositioned using a GUI planning tool (Figure 4.3). Bone fragments that are not selected are fixed bones. The surgeon also indicates whether a bone contains teeth.

In the third stage, salient surfaces are identified on the bone fragments (Figure 4.2(d)). Salient surfaces are surfaces that should be flushed (i.e., continuous) after restoration. They consist of outer surfaces of the skull that can be automatically detected and surfaces around the eye sockets that are difficult to detect automatically, which need to be indicated by the surgeon (Figure 4.4).

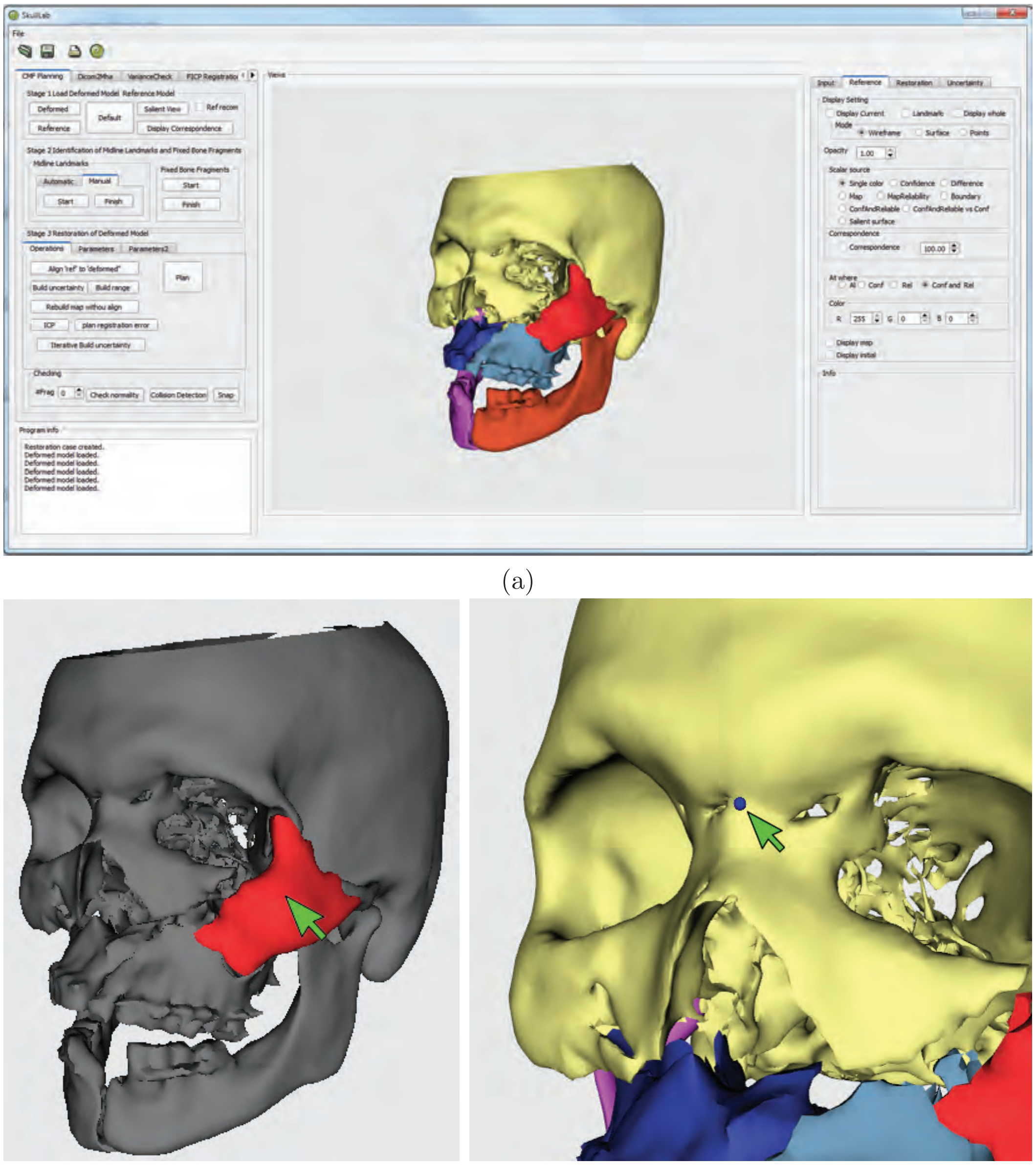

(a)

(b) (c)

Figure 4.3: Planning tool for indicating movable bone fragments and anatomical landmarks. (a) GUI of planning tool. (b) Identification of movable bone fragments to be repositioned. (c) Identification of a MSP landmark.

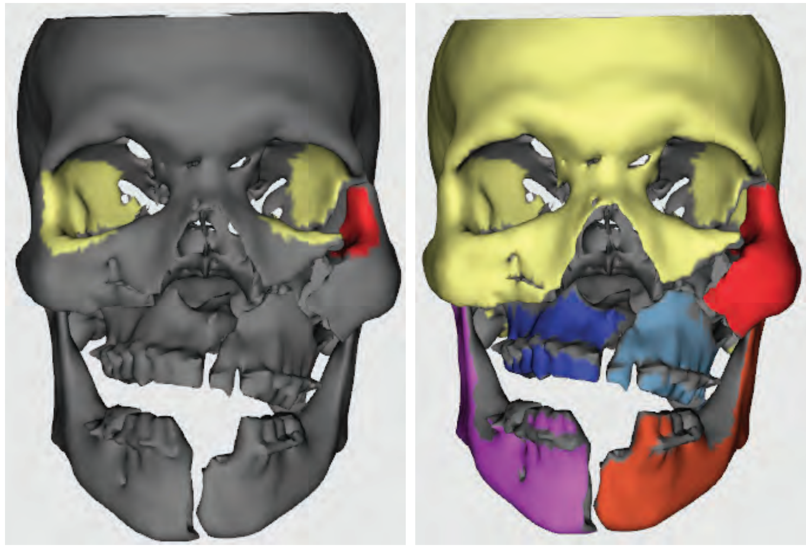

(a) (b)

Figure 4.4: Identification of salient surfaces. (a) Eye orbit regions identified by user. (b) Identified salient surfaces, including outer surfaces detected automatically.

In the fourth stage, FP, MSP and their landmarks are identified (Figure 4.2(d)). For normal skulls and skulls with minor injuries, these landmarks can be identified by the automatic algorithm described in Chapter 5. For patients with severe head injuries, whose skulls may be grossly distorted, the proposed automatic algorithm may fail. In such cases, the surgeon needs to manually indicate FP and MSP landmarks on the deformed model (Figure 4.3(c)).

In the fifth stage of the planning procedure, the surgeon applies an automatic restoration algorithm to generate the restored model (Figure 4.2(e)) from the deformed model. The restoration algorithm takes a patient's deformed model and a reference model of a normal person as inputs and generates a restored model by repositioning the bones in the deformed model. Before restoration (Figure 4.5(1)), the fractured bones in the skull are displaced from their correct positions, making the overall shape abnormal. The boundaries of adjacent bones are discontinuous and the MSP and FP landmarks may not lie on the MSP and FP. After restoration (Figure 4.5(2)), the overall shape becomes normal, the boundaries of adjacent bones are flushed and the MSP and FP landmarks lie close to the MSP and FP. Details of the restoration algorithm are described in Chapter 6.

In the final stage of the procedure, the surgeon instructs the planning tool to export the repositioned bones in STL format. The STL files can be imported into Brianlab's planning

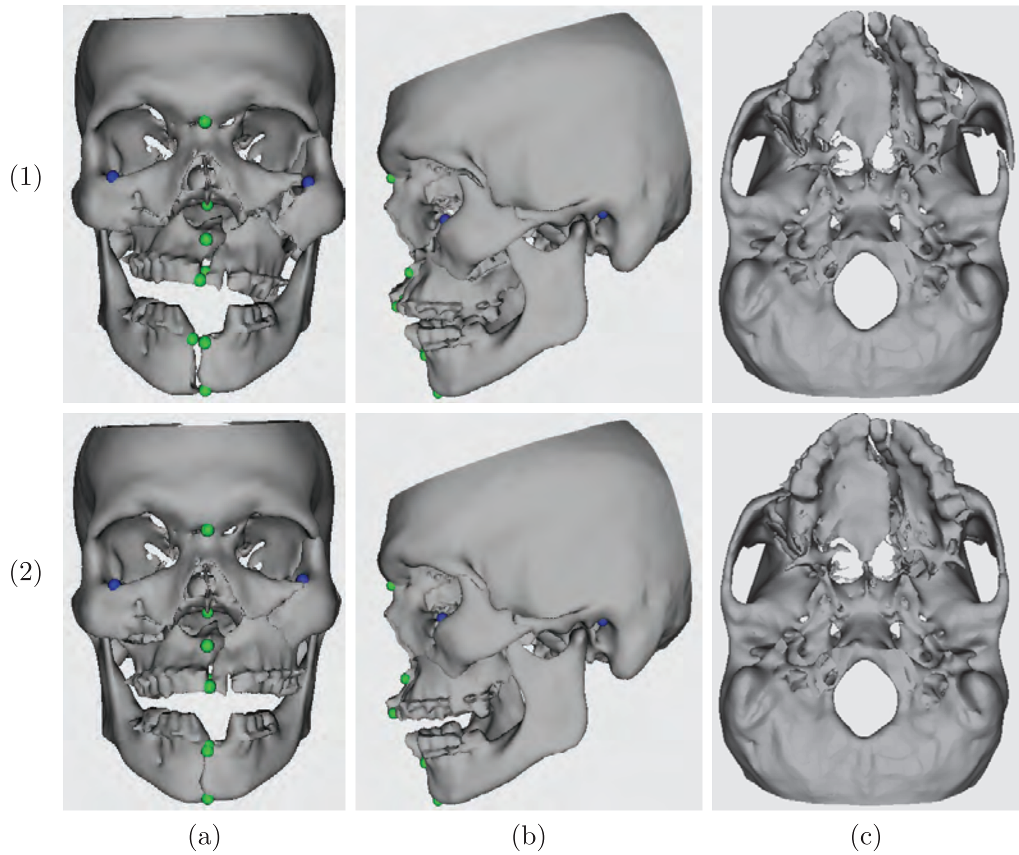


Figure 4.5: Restored skull vs. deformed skull. Top, deformed skull. Bottom, restored skull. Green balls, MSP landmarks. Blue balls, FP landmarks. (a) MSP alignment. (b) FP alignment. (c) Lateral symmetry and surface continuity.

software to overcome Brainlab's limitations. The planning tool also synthesizes DICOM images of the restored model (Figures 4.2(f) and 4.6) for the surgeon's verification.

The proposed planning procedure is flexible. In some cases, the FP landmarks are difficult to identify because of bone fractures. If FP landmarks are wrongly identified, they may result in an unsatisfactory restoration (Figure 4.7(2)). In this case, the surgeon may skip the landmarks that are difficult to identify, and the skull restoration algorithm can still generate restored model (Figure 4.7(3)). The proposed procedure also allows the surgeon to explore various plans by selecting different bone fragments to be repositioned (Figure 4.8).

At present, segmentation and mesh model construction are performed by several tools (Section 4.2) that are separate from the surgery planning tool (Figure 4.3). In the future, we plan to develop an integrated tool for the entire procedure.

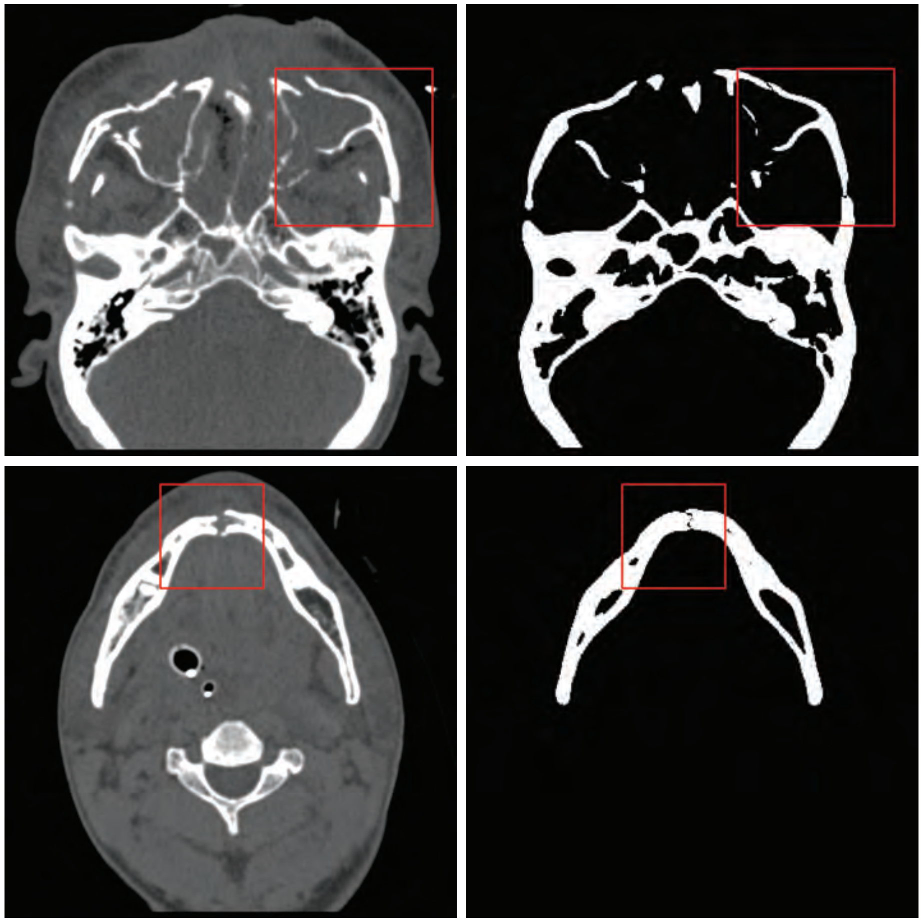

(a) (b)

Figure 4.6: Synthesized DICOM images of the restored model. (a) CT images of the deformed skull. (b) Synthesized DICOM images of the restored model.

For comparison, Brainlab's CMF planning procedure is summarized in Figure 4.9. In the first stage, the surgeon applies thresholding method to segment the healthy parts of the skull (Figure 4.10(a)) which will be used as a reference for the fractured part on the opposite side of the skull. Brainlab segments the required parts and generate their mesh models. In the second stage, the surgeon indicates MSP and FP landmarks and Brainlab fits the MSP and FP to the landmarks. In the third stage, Brainlab reflects the healthy parts about the MSP to serve as the reference for fractured parts (Figure 4.10(b)). The surgeon can manually adjust the positions and orientations of the reflected parts to match the fractured parts. Finally, Brainlab outputs the reference model into a proprietary Brainlab file which can be imported into its intra-operative guidance system. In contrast, the proposed procedure generates a restored model by bone repositioning, the

(1)

(2)

(2)

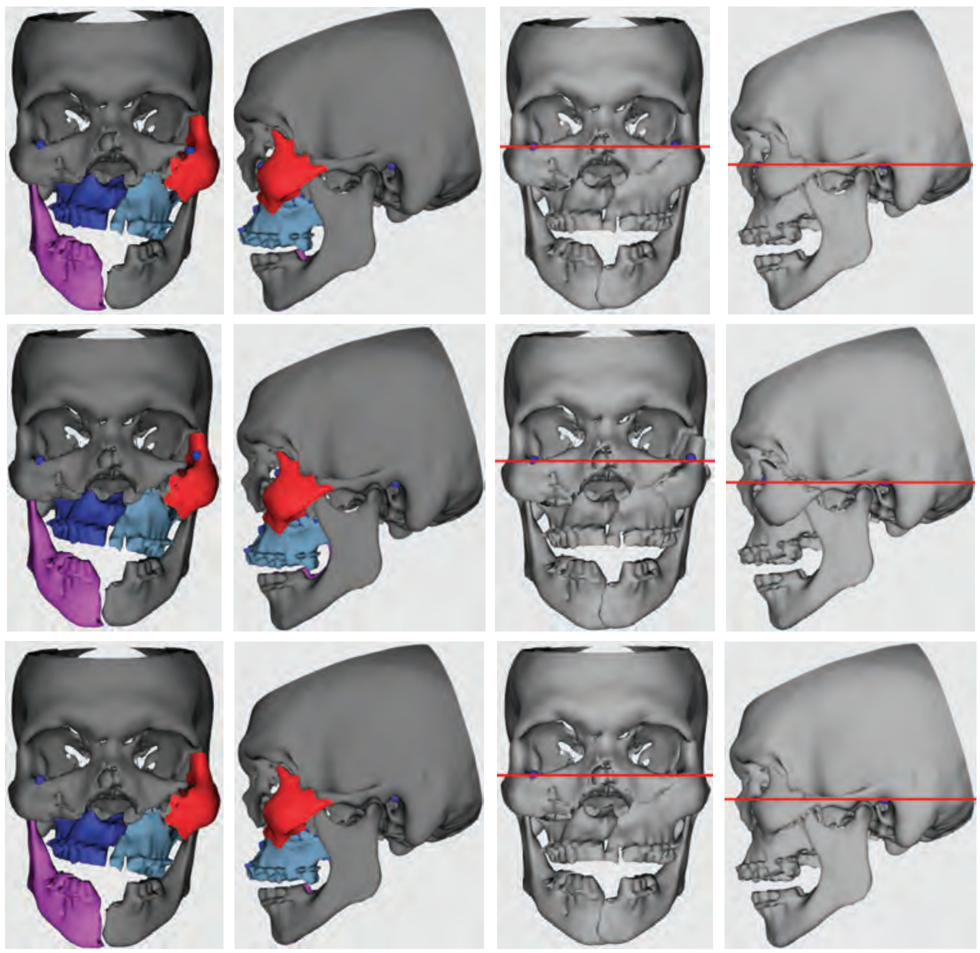

(a) (b) (c) (d)

Figure 4.7: FP landmarks identification affects the restored model. (1) FP landmarks are accurately identified on movable bones, and the restored model is accurate. (2) FP landmarks are inaccurately identified on movable bones, and the restored model is misled by the them. (3) No FP landmarks are identified on movable bones, the restored model is also acceptable. Blue balls indicate FP landmarks. (a, b) Deformed skull, colored bones are movable. (c, d) Restored skull, red lines indicate the FP.

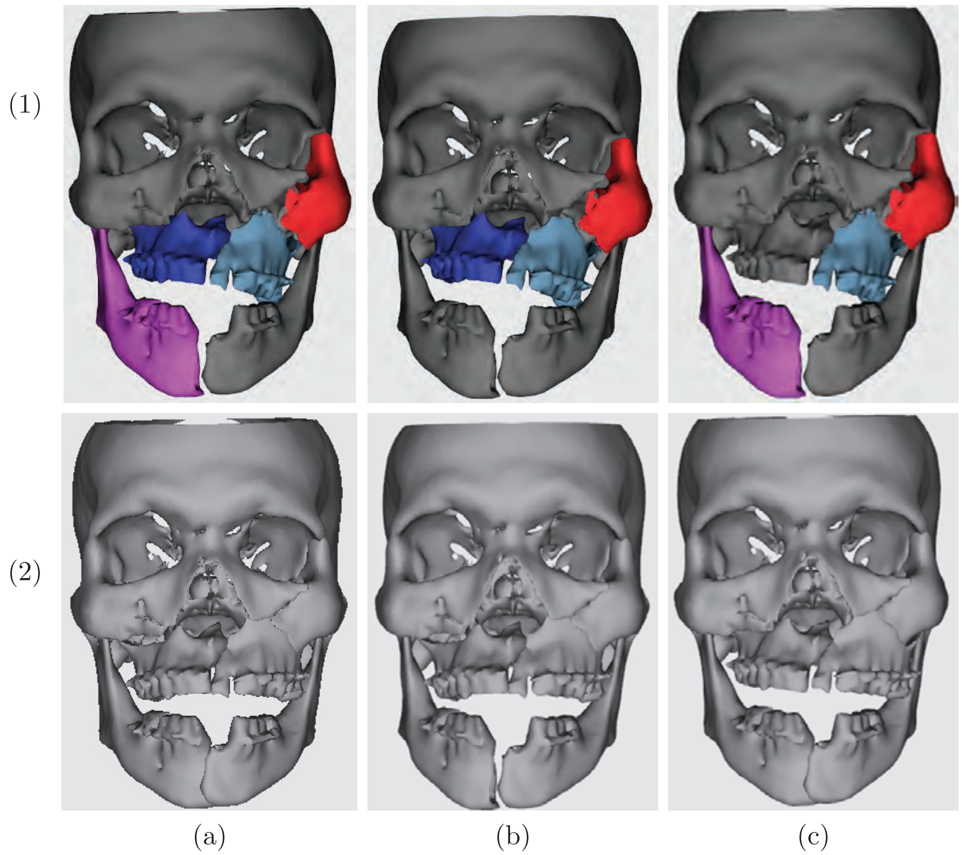

Figure 4.8: Exploration of various surgery plans. Selecting different bones to be repositioned (1) result in different restored models (2). (a–c) Various selection of bones to be repositioned.

bone fragments in it are from the patient's deformed model.

In patients with bilateral fractures (Figure 4.10 (d, e)), there is no single healthy part that can be used as the reference. Brainlab's procedure cannot be applied directly. At present, the surgeon has to segment small pieces of bones on either side, reflect them to the other side and fuse them together into a single piece to serve as the reference. This process is tedious, time-consuming and inaccurate. In contrast, the proposed procedure can successfully generate the restored skulls for bilaterally fractured skulls.

In general the proposed planning procedure is similar to Brainlab's procedure. Both methods generate patient's models from medical images, require the user to indicate healthy and fractured parts and MSP and FP landmarks, and generate a planning output. The differences are as follows:

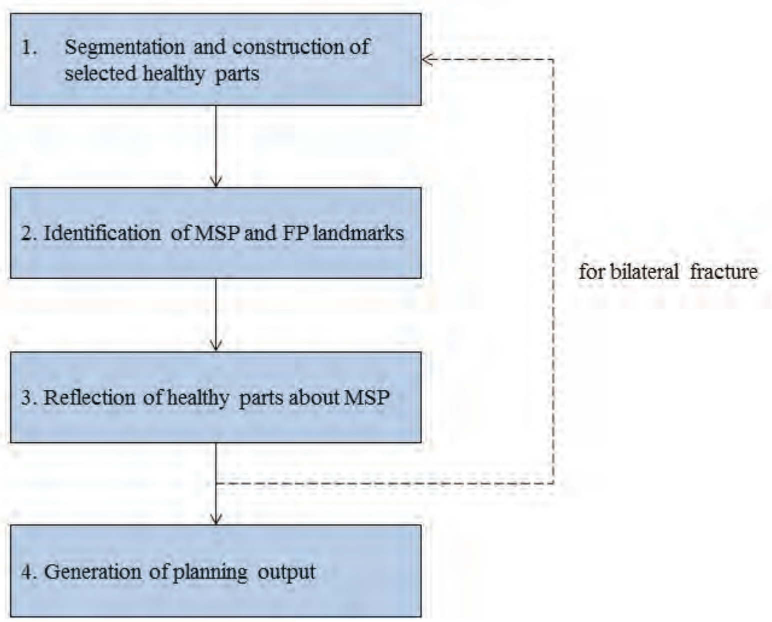


Figure 4.9: Brainlab's CMF surgery planning procedure. Stage 1 to 3 are repeated to sidestep Brainlab's limitations to unilateral fracture.

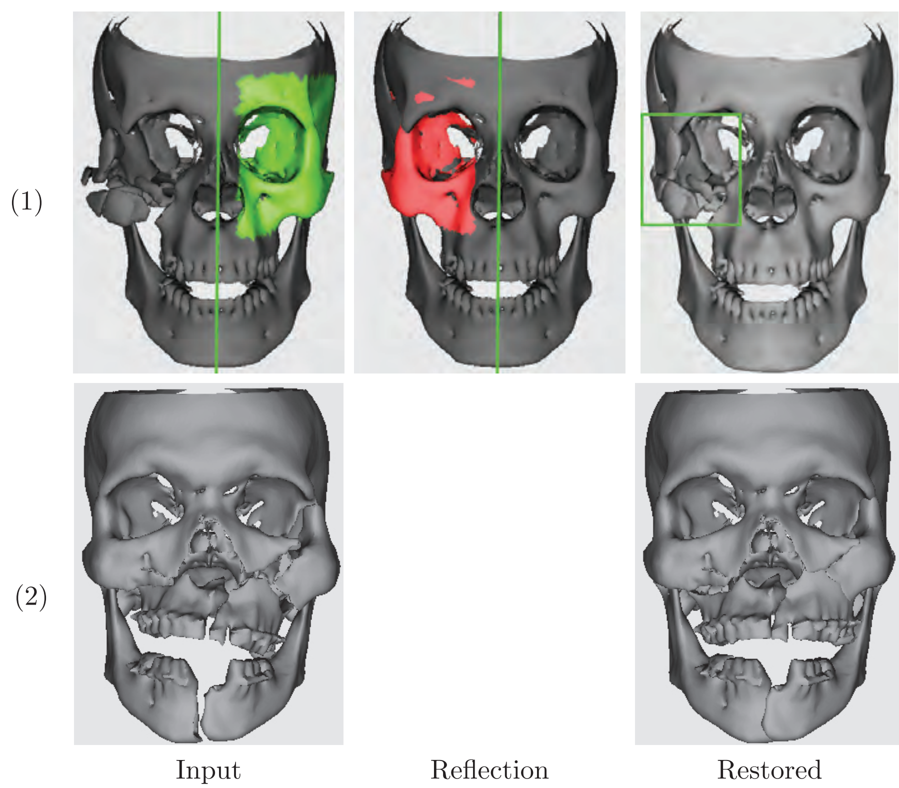


Figure 4.10: Comparison of reflection-based reconstruction and the proposed restoration algorithm. Reflection-based method can only handle unilateral fractured cases (1). The proposed method can handle both unilateral (1) and bilateral (2) fractured cases. (a) Inputs. Green region is the user indicated healthy region on one side. (b) Reflection overlaid on the deformed skulls without the fractured bones. Red region is the reflection of the green region about the MSP indicated by the green line. (c) Restored models.

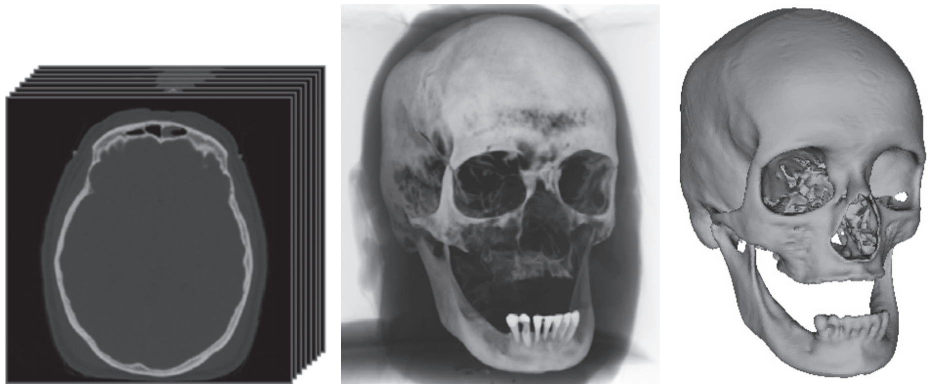

(a) (b) (c)

Figure 4.11: Threshold segmentation of normal skull. (a) CT images. (b) Volume Rendering. (c) Skull model constructed from threshold segmentation result.

1. The proposed procedure provides an automatic FP, MSP and landmark identification method for skulls with minor injuries.

2. The proposed procedure replaces Brainlab's reflection method by an automatic restoration algorithm.

3. The proposed procedure generates a restored model by bone repositioning whereas Brainlab generates a partially reconstructed model by lateral symmetry.

## 4.2 Segmentation and 3D Model Reconstruction

Several existing methods have the potential to solve the segmentation and 3D reconstruction problem. Thresholding algorithm [SS04] is suitable for whole skull segmentation. However, it is not suitable for the proposed procedure because the proposed procedure requires a separate mesh model for each of the bone fragments. Thresholding algorithm does not provide any information about which voxel belongs to which bone fragment and produces only a whole mesh model for the skull (Figure 4.12).

Fully automatic segmentation of individual bone fragments from medical images is a very challenging problem. State-of-the-art commercial segmentation software such as Amira [Gmb] provides only a thresholding algorithm for automatic segmentation, which is insufficient as discussed earlier. ITK-SNAP [YPH*06], an open-source segmentation software, provides a level-set algorithm [KWT88] for seeded automatic segmentation. How-

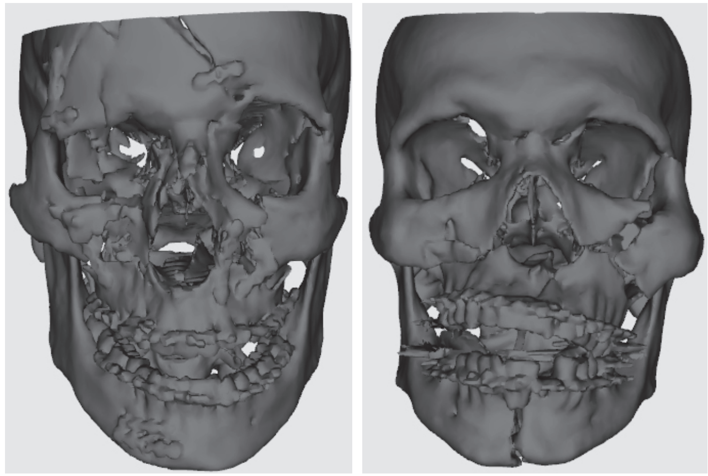

(a) (b)

Figure 4.12: Threshold segmentation of deformed skulls.

ever, the level-set algorithm may leak into irrelevant regions such as the cracked regions between bone fragments and the regions belonging to neighboring bone fragments. In summary, there is no existing automatic method that can segment separate bone fragments.

The focus of this thesis is CMF surgery planning and restoration of deformed skull models. Fully automatic segmentation of separate bone fragments is outside the scope of this research. So in the proposed procedure, bone fragment segmentation is performed using a semi-automatic method. First, the user applies a thresholding algorithm in Seg3D [CIB13] to segment the whole skull from the CT images. Usually, parts of the fractured regions are in the segmentation result because they also have high intensities. Then, the user manually separate connected bone fragments slice by slice using the interactive segmentation tool provided by ITK-SNAP [YPH*06]. Mesh model rendering, volume rendering and CT slices are used to guide this stage. After that, the user applies marching cubes algorithm [LC87] in ITK-SNAP to generate separate meshes for the segmented bone regions. Finally, the user smoothes the mesh models using Laplacian smoothing [Fie88] and reduces the mesh resolution using Garland's quadratic edge collapse method [GH97], both supported by Meshlab [CNR13].

For comparison with the proposed method, a combination of thresholding and level-set algorithm is applied to segment a bone fragment of the right cheek bone. First, the thresholding algorithm generates the initial seeds using a high threshold. Then, the

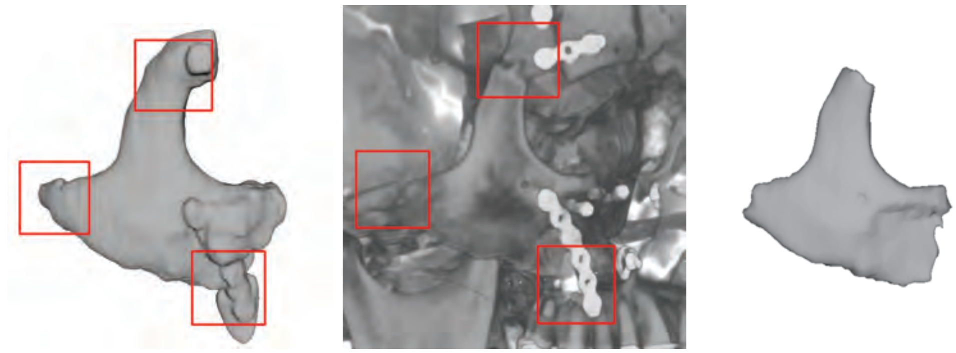

(a) (b) (c)

Figure 4.13: Level-set segmentation. (a) 3D mesh constructed from level-set segmentation result shows that the level-set leaks into neighboring regions (square box). (b) Volume rendering of the region segmented. (c) Correct 3D mesh without leakage.

level-set algorithm segments the bone fragment. Finally, the same procedure to generate, smooth and simplify the mesh is applied. Figure 4.13(a) shows that the level-set algorithm leaks through the crack regions to the neighboring bone fragments because the cracks between the bone fragments are very small and unclear in the images.

The constructed deformed model (Figure 4.14(a)) was verified by an experienced CMF surgeon in NUH who operated on the patient. Volume rendering (Figure 4.14(b)) and CT images (Figure 4.14(c)) were provided to assist in the verification. The surgeon concluded that the patient's skull model was correctly constructed.

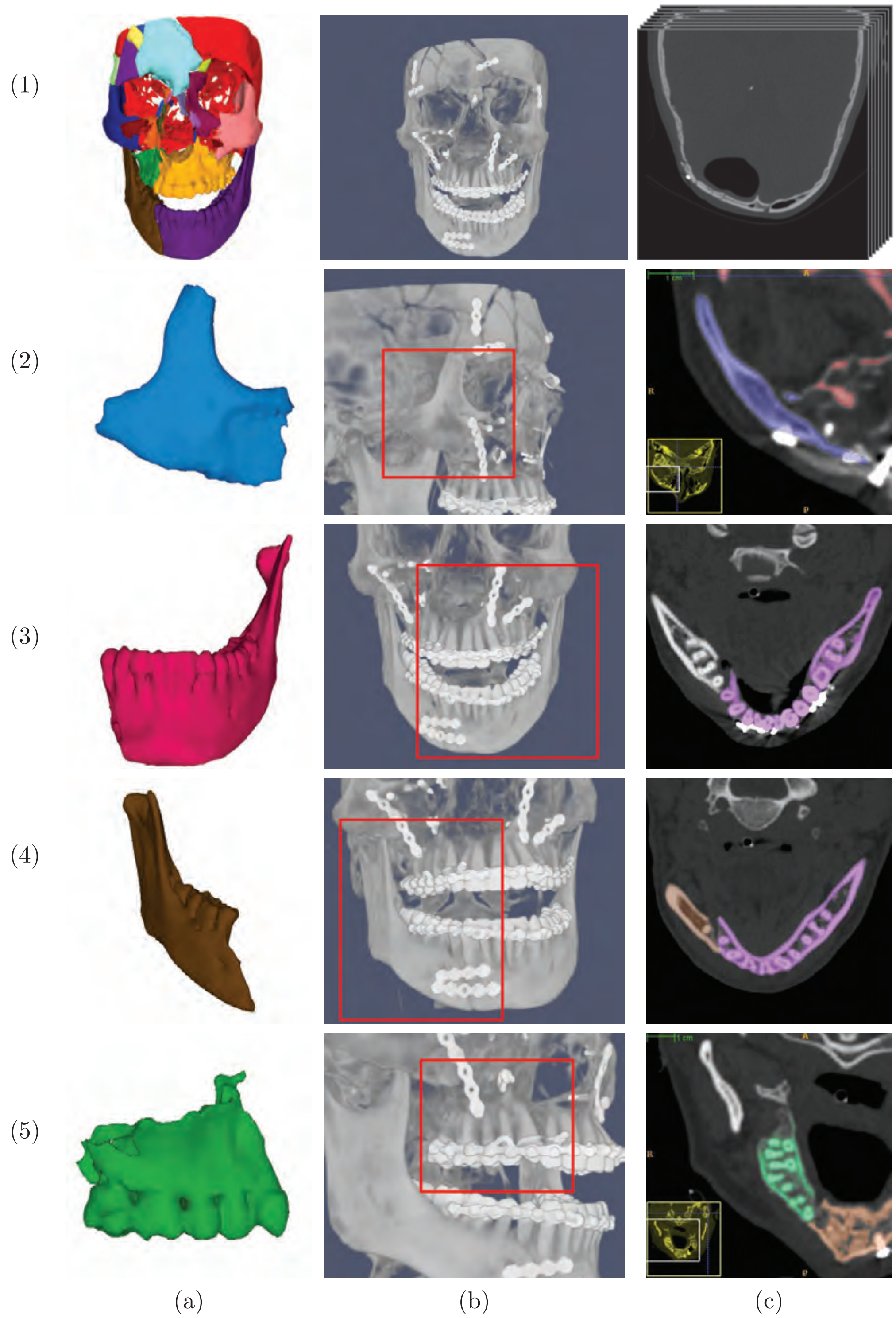


Figure 4.14: Segmentation and mesh construction result. (a) Mesh model. (b) Volume rendering. (c) CT slice. (1) Entire skull. (2) Right cheek bone. (3) Left lower jaw. (4) Right lower jaw. (5) Right upper jaw.

# Chapter 5

# FP and MSP identification

In surgery, forensics, and anthropology, identification of the Frankfurt plane (FP) and mid-sagittal plane (MSP) of a human skull (Section 2.2) is a very important task. These anatomical planes are used to define the three anatomical orientations of the skull: lateral (left-right), anterior-posterior (front-back), and superior-inferior (up-down). These anatomical orientations, in turn, are used to define craniometric landmarks that are used for pre-operative surgery planning, intraoperative surgery guidance, forensic reconstruction, and anthropological and archaeological studies [CHV99, DMCP*06, GWL99, SH, Tay01, Woo31]. Thus, automatic identification of FP and MSP, and landmarks, greatly facilitates computer-assisted processing and analysis in these applications.

The skull is a very complex 3D structure consisting of 28 bones that are fused together. While its general shape is similar for all normal humans, it can vary greatly in size and shape details among different individuals. Old age, diseases, and injuries can cause further changes to the skull's shape. Therefore, automatic identification of FP and MSP is a very difficult and challenging task.

## 5.1 FP and MSP Identification Algorithm

In anatomy, FP and MSP are used to define the skull's anatomical orientations (Section 2.2). In particular, lateral orientation is normal to MSP and up-down orientation is normal to FP. These orientations, in turn, are used to define craniometric landmarks. For example, the orbitale is the lowest point of the orbit (Figure. 2.2). But the lowest point changes as the orbit is rotated. So, incorrect skull orientation can result in inaccurate localization of landmark points, which in turn leads to inaccurate identification of MSP and FP that define the skull orientation. To resolve this difficulty, the proposed method registers a template skull model with known landmarks to a target skull to automatically locate the landmarks on the target skull. It then fits two planes to the landmarks to obtain good initial estimates of FP and MSP. Then, it iteratively refines the locations of the landmarks and the locations and orientations of FP and MSP.

An overview of the iterative algorithm is given in Algorithm 1. The set of anatomical landmarks used in this algorithm is described in Section 2.2.

---

**Algorithm 1: FP, MSP and Midline Landmarks Identification Algorithm**

**Input**: Template mesh model, target mesh model.

**Output**: The FP, MSP and midline landmarks on the target mesh model.

1. Register a template mesh model with known landmarks to the target mesh model.
2. Locate the landmarks on the target model using the registered template model, and fit FP and MSP to the MSP landmarks and FP landmarks in least square manner. These landmarks and the fitted planes serve as the initial estimates.
3. Repeat until convergence:
   (a) Refine locations of FP landmarks according to their medical definitions, and fit FP to the refined FP landmarks.
   (b) Refine locations of MSP landmarks according to their medical definitions, and fit MSP to the refined MSP landmarks, keeping it orthogonal to FP.

---

### 5.1.1 Model Registration

Human skulls naturally vary in shape details and sizes. Moreover, parts of the target skull may be missing due to diseases or injuries. To achieve good registration under these

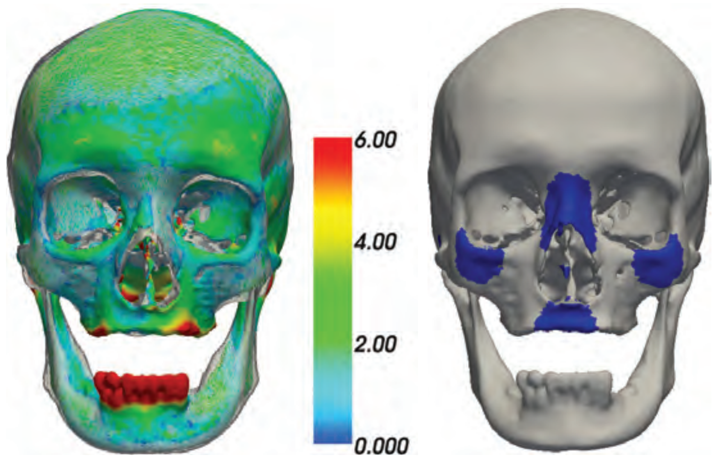


Figure 5.1: FICP registration and initialization. (a) FICP registration result of target model. Colors indicate the distances of the target points to corresponding template points (mm). (b) Landmark regions (blue) are located on the target model.

conditions, Fractional Iterative Closest Point (FICP) [PLT07], a variant of ICP [BM92] robust to these variations, is used. Like ICP, FICP iteratively computes the best similarity transformation that registers the template to the target. The difference is that in each iteration, FICP computes the transformation using only a subset of template points whose distances to the target model are the smallest. Figure 5.1(a) shows that FICP registration is very robust and accurate despite the differences between the template and the target.

### 5.1.2 Initialization

After registering the template model to the target model, known landmark points on the template are located on the target model (Figure 5.1(b)). This is achieved by mapping the template landmarks to the corresponding points on the target. Given these initial estimates of the landmark points, two planes are fitted to these points to yield the initial estimates of FP and MSP by applying Principal Component Analysis (PCA). The mean of the landmark points gives the position of the plane, and the smallest eigenvector obtained by PCA gives the unit normal vector of the plane. So, the FP and MSP are each represented by its position and unit normal vector.

The initial FP and MSP define initial estimates of the skull's orientations. Let $\mathbf{u}_x$, $\mathbf{u}_y$, and $\mathbf{u}_z$ denote the unit vectors pointing towards the left-lateral, up, and front directions

(Figure 2.2a). Then, $\mathbf{u}_x$ is normal to MSP, $\mathbf{u}_y$ is normal to FP, and $\mathbf{u}_z = \mathbf{u}_x \times \mathbf{u}_y$.

Due to normal variations of the human skulls, the template and target models may differ in shape details and sizes. So, the initial estimates of the target landmark points are not accurate. To obtain more accurate estimates, an elliptical region is placed around each target landmark point, and the mesh surfaces within the elliptical region are identified as the landmark region. The orientation and size of the ellipse are empirically predefined to fixed values, and they vary for different landmarks according to the shape of the skull around the landmark. It should be large enough to include the landmark on the target model. During iterative refinement (Section 5.1.3, 5.1.4), accurate locations of the landmarks are searched within the landmark regions according to the definitions of the landmarks. An exception is FMC, the center of foramen magnum (Sectionsec:planes). Since FMC does not lie on skull surface, landmark region is not defined for FMC.

### 5.1.3 Frankfurt Plane Identification

The Frankfurt plane (FP) passes through the orbitales and the porions (Figure 2.2). The orbitales (Ol, Or) are the lowest points of the lower margins of the orbits. To accurately locate the (left or right) orbitale, sagittal sections $S(x)$ of the lower margins parallel to the MSP are obtained, where $x$ is a local coordinate along the $\mathbf{u}_x$ direction. Each sagittal section $S(x)$ contains a part of the landmark region $R$ of the orbitale (Figure 5.2). The points $\mathbf{q}(x)$ on the lower margins correspond to the highest points in the intersections between $R$ and $S(x)$. The orbitale is the lowest point $\mathbf{q}(x)$ in the $\mathbf{u}_y$ direction. In other words, its $x$-coordinate minimizes the following objective function $F(x)$:

$$F(x) = \mathbf{q}(x) \cdot \mathbf{u}_y, \quad \mathbf{q}(x) = \arg \max_{\mathbf{p} \in R \cap S(x)} \mathbf{p} \cdot \mathbf{u}_y. \tag{5.1}$$

Porions are the most lateral points on the roof of the external bony ear holes. The surface normals of the roof points are in the direction of $-\mathbf{u}_y$. To accurately locate the porions, the algorithm looks for the most lateral points in the left and right landmark regions $R_l$ and $R_r$ whose surface normals are close to $-\mathbf{u}_y$. That is, select subsets $S_l$ and $S_r$ of points respectively in $R_l$ and $R_r$ whose surface normals are close to $-\mathbf{u}_y$. Then, the

(a) (b)

Figure 5.2: Sagittal section. (a) Sagittal section of lower orbit is indicated by the purple plane. (b) A sagittal section. Landmark region is colored green.

left porion is located at the most lateral point $\mathbf{q}_l$ on the left side:

$$\mathbf{q}_l = \arg\max_{\mathbf{p}\in S_l} \mathbf{p}\cdot\mathbf{u}_x, \tag{5.2}$$

and the right porion is located at the most lateral point $\mathbf{q}_r$ on the right side:

$$\mathbf{q}_r = \arg\max_{\mathbf{p}\in S_r} \mathbf{p}\cdot(-\mathbf{u}_x). \tag{5.3}$$

After refining FP landmark points' locations, a plane is fitted to the points using PCA to yield the refined FP.

### 5.1.4 Mid-Sagittal Plane Identification

The mid-sagittal plane (MSP) passes through 6 landmarks discussed in Section 2.2. Four of them are ridges and one is a peak point. So, methods for detecting ridges and peaks on the skull model are required. In theory, these features can be detected by computing curvatures on the skull surface. However, the accuracy of curvature computation is sensitive to the regularity and resolution of the mesh model [CRT04]. So, we apply the method proposed by Avants et al. [AG03] to compute curvature based on the Gauss map in a local neighborhood, which is numerically more stable.

### Computing Principal Curvatures

The Gauss map $\mathbf{N}(u, v)$ is a function of the surface normal parameterized by local coordinates $(u, v)$ on the surface. The derivative $d\mathbf{N}$ measures local changes of $\mathbf{N}(u, v)$, which is related to surface curvature. The derivatives $\mathbf{N}_u$ and $\mathbf{N}_v$ in the $u$- and $v$-direction lie in the planes formed by the tangents $\mathbf{T}_u$ and $\mathbf{T}_v$, and they can be expressed as

$$\mathbf{N}_u = a\mathbf{T}_u + c\mathbf{T}_v, \quad \mathbf{N}_v = b\mathbf{T}_u + d\mathbf{T}_v, \tag{5.4}$$

for some values $a, b, c$, and $d$. The Jacobian of $d\mathbf{N}$ expressed in the local coordinates gives the shape operator $S$:

$$S = \begin{bmatrix} a & c \\ b & d \end{bmatrix}. \tag{5.5}$$

It has been shown that the eigenvalues $\kappa_1, \kappa_2$ and eigenvectors $\mathbf{e}_1, \mathbf{e}_2$ of $S$ give the magnitudes and directions of the principal curvatures [DoC76].

In numerical computation, the Gauss map can be approximated by a degree-one polynomial:

$$\mathbf{N}(u, v) = \mathbf{g}_0 + \mathbf{g}_1 u + \mathbf{g}_2 v. \tag{5.6}$$

Fitting Equation 5.6 to a neighborhood of points and their surface normals gives the vectors $\mathbf{g}_i$. The derivatives $\mathbf{N}_u$ and $\mathbf{N}_v$ are simply $\mathbf{g}_1$ and $\mathbf{g}_2$. Then, the principal curvatures $\kappa_1, \kappa_2$ and their directions $\mathbf{e}_1, \mathbf{e}_2$ can be computed from $\mathbf{N}_u$ and $\mathbf{N}_v$ using the method discussed above.

### Ridge Detection

Landmark points NR, MPR, VR, and EOC are ridges on the skull (Section 2.2, Figure 2.2). A point $\mathbf{p}$ on a ridge that runs along direction $\mathbf{d}_r$ has locally maximum curvature along the direction $\mathbf{d}_t$ orthogonal to $\mathbf{d}_r$. Since the ridge lies in MSP, the ridge direction $\mathbf{d}_r$ and surface normal $\mathbf{n}$ at $\mathbf{p}$ lie in the same plane as $\mathbf{u}_y$ (Figure 5.3), which has been refined in Step 3(a) of the algorithm (Section 5.1.3). So, $\mathbf{d}_t$, which is orthogonal to $\mathbf{d}_r$, can be computed as

$$\mathbf{d}_t = \frac{\mathbf{n} \times \mathbf{u}_y}{|\mathbf{n} \times \mathbf{u}_y|}. \tag{5.7}$$

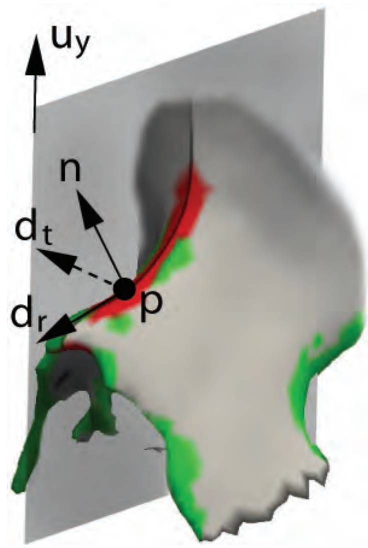


Figure 5.3: Ridge structure. Colored regions around the ridge have large curvatures, but only the red region is on the ridge.

Given a landmark region $R$, the ridge is detected as follows. First, the principal curvatures $\kappa_1, \kappa_2$ and their directions $\mathbf{e}_1, \mathbf{e}_2$ are computed using the method discussed in Section 5.1.4. Applying Euler's theorem, their normal curvatures $K_n$ along $\mathbf{d}_t$ can be computed as

$$K_n = \kappa_1 \cos^2\phi + \kappa_2 \sin^2\phi \tag{5.8}$$

where $\phi$ is the angle in the tangent plane measured counterclockwise from the direction $\mathbf{e}_1$ of the minimum principal curvature to $\mathbf{d}_t$. The points with large normal curvature $K_n$ are more likely to lie on the ridge.

In general, the triangular faces of a mesh model can vary in size. So, for accurate ridge detection, the high-curvature points are sampled from the centers of triangles instead of mesh vertices. Then, the areas of the triangles can be used as weights of the high-curvature points in ridge detection.

Note that the landmark region $R$ needs to be large enough to include the ridge. As a result, it may also include other nearby surfaces. So, the high-curvature points obtained above may include points on the ridge (inliers) and points on other nearby surfaces (outliers) (Figure 5.2c).

RANSAC is applied to iteratively identify the optimal set of inliers. A line $l$ is fitted to the inliers to represent the ridge by applying PCA. The position of $l$ is given by the mean of the inliers weighted by the areas of their triangular faces, and the direction of $l$ is given by the component $\mathbf{u}_l$ of the largest eigenvector $\mathbf{v}$ that is parallel to MSP:

$$\mathbf{u}_l = \mathbf{v}_l / \|\mathbf{v}_l\|, \quad \mathbf{v}_l = \mathbf{v} - (\mathbf{v} \cdot \mathbf{u}_x)\mathbf{u}_x, \tag{5.9}$$

where $\mathbf{u}_x$ is the normal vector of MSP. As the triangles typically vary in size, the area-weighted mean yields a more accurate position of the line than the unweighted mean.

### Peak Detection

Posterior nasal spine (PNS) is a peak landmark point (Section 2.2). A peak point has a locally maximum Gaussian curvature. To locate the peak accurately, the algorithm computes Gaussian curvature not only for mesh vertices but also for points inside the triangular faces.

A point in a triangle can be uniquely represented by the barycentric coordinates $(u, v)$ defined on the triangle. Then, the method discussed in Section 5.1.4 can be used to compute the principal curvatures $\kappa_1(u, v)$ and $\kappa_2(u, v)$. The Gaussian curvature is simply $K(u, v) = \kappa_1(u, v)\kappa_2(u, v)$. So, accurate location of the peak can be computed by finding the position $(u, v)$ over all the triangles in the landmark region $R$ that maximizes the Gaussian curvature $K(u, v)$.

### Foramen Magnum Center Detection

The margin of the foramen magnum is approximately circular. It has locally maximum curvature along the radial direction. So, to locate the foramen magnum center (FMC), a circle $C(\mathbf{c}, r)$ located at $\mathbf{c}$ with radius $r$ is fitted to the FMC region that has large maximum principal curvature $\kappa_2$. This is achieved by determining the circle $C(\mathbf{c}, r)$ that minimizes the objective function $F(\mathbf{c}, r)$:

$$F(\mathbf{c}, r) = \sum_{\mathbf{p} \in C(\mathbf{c}, r)} \{\kappa_M - \kappa_2[f(\mathbf{p})] + \gamma \|\mathbf{p} - f(\mathbf{p})\|\} \tag{5.10}$$

where $f(\mathbf{p})$ is the closest point of $\mathbf{p}$ on the target model, $\gamma$ is a constant weight and $\kappa_M$ is a constant representing the maximum possible $\kappa_2$ value. The first term is minimized for points with large $\kappa_2$, and the second term is minimized for points close to $C(\mathbf{c}, r)$.

#### Mid-Sagittal Plane Refinement

Refinement of MSP is performed by fitting a plane to the MSP landmarks subject to the constraint that the plane is orthogonal to FP. Since MSP is orthogonal to FP, its projects to a line $l$ on FP. The perpendicular distance of a point $\mathbf{p}$ to MSP is equal to the distance of the projection of $\mathbf{p}$ on FP to the line $l$. So, the line $l$ can be obtained by fitting it to the projections of MSP landmark points on FP. Then, the mid-point of $l$ gives the location of MSP, and MSP's normal vector $\mathbf{u}_x$ can be obtained as the cross product of FP's normal vector $\mathbf{u}_y$ and $l$'s unit direction vector $\mathbf{u}_z$: $\mathbf{u}_x = \mathbf{u}_y \times \mathbf{u}_z$.

## 5.2 Experiments and Discussion

Four full skulls were used in the experiments, of which three were from Visible Human Project, and one was from OsiriX. One full skull was used as the template (Figure 2.2) and the others were the test targets. In clinical practice, CT images are acquired only for the parts of the skulls under treatment. For this reason, the 3 target full skulls were cut at the top and the bottom to produce 3 additional partial skulls for testing. The only requirement was that all the FP and MSP landmarks could still be located on the partial skulls. Moreover, three partial skulls of patients from a local hospital were also used for testing. With this setting, there are three groups of targets, namely, full skull, partial skull, and patient skull.

The resolutions of the CT images of the skull models ranged from 0.47 to 1 mm/pixel. The CT images were segmented and 3D mesh models were reconstructed from them.

### 5.2.1 Plane Identification

The proposed automatic FP and MSP identification algorithm was applied to the test targets. For comparison, an automatic algorithm that estimated MSP based on symmetry was also implemented and tested. For fair assessment, the same initialization as discussed in Section 5.1.2 was performed before executing the symmetry-based algorithm.

To assess the accuracy of the algorithms in identifying the FP and MSP, a human

Table 5.1: Comparison of plane-fitting error. The proposed method performs better than symmetry based method. Both of them reduced error from initialization. (full) Full test skulls. (partial) Partial skulls cut from full skulls. (patient) Patients' partial skull models.

| skull | FP (mm) | | MSP (mm) | | |
|---|---|---|---|---|---|
| type | initial | proposed | initial | symmetry-based | proposed |
| full | 1.17 | 0.64 | 1.47 | 0.86 | 0.48 |
| partial | 1.26 | 0.60 | 0.97 | 0.79 | 0.50 |
| patient | 1.72 | 0.58 | 1.17 | 1.01 | 0.61 |

expert was asked to mark ground-truth landmark points on the skulls. Their mean distances to the detected planes were used to measure the identification error. This error measurement is consistent with the medical definition of the planes.

Figure 5.4 and Table 5.1 show the results of the applied methods on target skulls. These results show that the proposed method can identify FP and MSP accurately and robustly. For FP identification, the proposed automatic method gives an error around 0.61 mm for all the three test cases, which is highly accurate compared to the CT resolution (0.47 to 1 mm/pixel).

For MSP identification, the proposed method is also very accurate. It identified MSPs closer to the midline landmarks than did the symmetry-based method. The error of the proposed method is consistently lower than that of the symmetry-based method for all test cases.

In addition, the proposed method is robust to the asymmetry in skulls. Its accuracy on full and partial skulls are roughly the same (0.48 mm and 0.50 mm) because important landmark points can be located on them. The small increase in error for patient skulls is within an acceptable range because patient skulls have fractures.

In contrast, test results show that the symmetry-based method is less robust because it uses all the mesh vertices, most of which are outliers in defining MSP. Compared to partial skulls, full skulls have top and bottom parts, which tend to be outliers. Therefore, the symmetry-based method, using all the mesh vertices, has a larger error on full skulls. Patient skulls have more outliers than partial skulls due to fractures. Therefore, the error for patient skulls is the largest.

Overall, the proposed method is consistently accurate in identifying both FP and MSP on all kinds of skulls. Moreover, in identifying MSP, the proposed method, using only the midline features, is more accurate and robust than the symmetry-based method.

### 5.2.2 Landmarks Identification

The proposed algorithm also identifies landmarks of the test targets. The mean distance from the landmarks to the ground truth landmarks is measured. The ridge structures (NR, MPR, VR, EOC) are parallel to MSP They are useful for determining MSP, but these ridge structures cannot uniquely locate positions within MSP, and so are not used for computing landmark identification error. So there are four FP landmarks and two midline landmarks for evaluation.

The mean distance from the identified landmarks to the ground truth landmarks are measured. Table 5.2 shows the landmark identification errors on different data sets.

For complete normal skulls, FP and MSP landmarks identification errors are 3.29 mm and 3.10 mm. The mean error over all landmarks is 3.23 mm. This accuracy can be considered accurate compared to the CT resolution of about 0.5 mm.

For partial skulls, FP and MSP landmarks identification errors are 2.88 mm and 3.28 mm. The mean error over all landmarks is 3.01 mm. The errors are also small for partial skulls. This is because of the FICP registration algorithm is robust to the missing parts and gives similar quality initialisation as for complete skulls. The error is smaller than for full skulls. This is because the full skulls contain the top parts which are outliers for FP and MSP identification lacking of distinguishing FP and MSP features.

For patient skulls, FP and MSP landmarks identification errors become 5.90 mm and 2.90 mm. The mean error over all landmarks is 4.27 mm. Compared with normal complete skulls and partial skulls, the average error for patient skulls is increased by about 1 mm. Considering the incomplete scanning and deformation caused by fracture in real patient models, 1 mm increase from around 3 mm can also be considered accurate. For patients having serious injuries, the landmarks might not be located a normal position and orientations, the proposed method would become less accurate for them.

The result for full skull is slightly worse than for partial skulls. This is because the full models contains more outliers that affect the FICP algorithm in the initialisation stage.

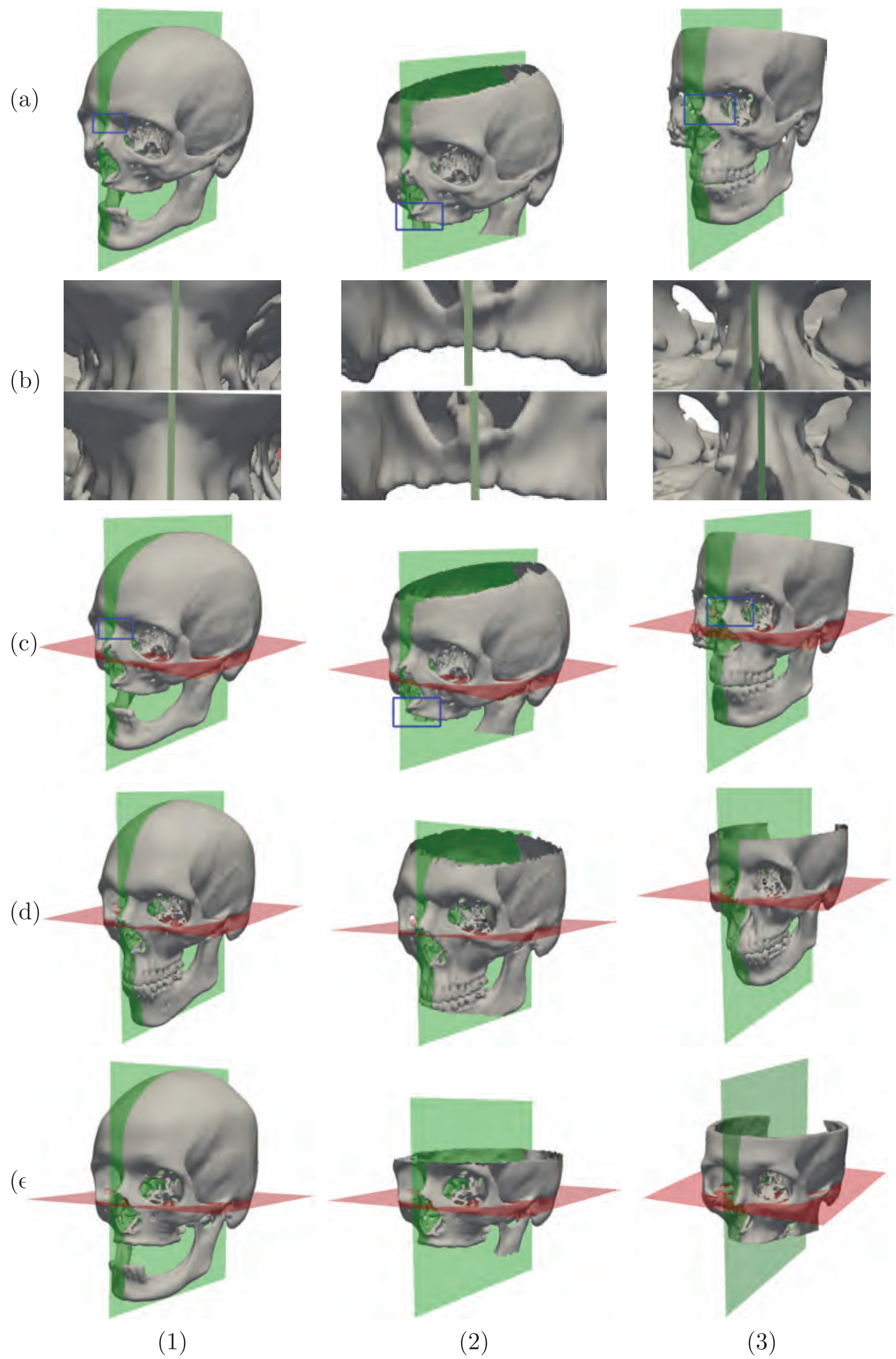


Figure 5.4: Identified MSP and FP. (1) Full skulls. (2) Partial skulls of (1). (3) Patient Skulls. (a) MSP of the models in (c) detected by symmetry-based method. (b) Zoom-in comparison of (a) on top and (c) at bottom. (c–e) Planes detected by proposed method.

Table 5.2: Landmark identification error averaged over the test skulls. (full) Full test skulls. (partial) Partial skulls cut from full skulls. (patient) Patients' partial skull models.

| Skull | FP Landmarks (mm) | MSP Landmarks (mm) | All Landmarks (mm) |
|---|---|---|---|
| full | 3.29 | 3.10 | 3.23 |
| partial | 2.88 | 3.28 | 3.01 |
| patient | 5.90 | 2.90 | 4.27 |

And the proposed algorithm guarantees local optimal from this initialisation.

Figure 5.5 shows landmarks identified by the proposed method. The green balls represent midline landmarks, and the red ones represent the Frankfurt plane landmarks. As can be seen, the landmarks are accurately identified on the skulls, even for patient's deformed skull.

## 5.3 Conclusion

This chapter presented an automatic, robust, and accurate method for identifying FP and MSP of human skulls. The method registers a template skull model with known landmarks to the target skull to obtain good initialization of the landmarks, FP, and MSP on the target. Next, it iteratively refines the landmarks, FP, and MSP according to anatomical definitions. Test results show that the algorithm is more robust and accurate than a symmetry-based algorithm in identifying MSP. Moreover, it can be applied to partial skulls. At this thesis, we only show experiments on detecting FP and MSP landmarks which is related to the thesis work. The proposed method has also been extended to accurately detect another 15 important craniometric landmarks in the application of building dense correspondence between skulls [ZCL13].

The proposed method works well for normal skulls and skulls with minor fractures. For certain plagiocephalic children and patients with serious head injuries, their skulls may be grossly distorted and the landmarks may not be located at their normal positions. In these cases, the proposed method is not expected to locate the landmarks accurately. As the skulls are grossly distorted, the concept of FP and MSP may not have much relevance in these cases, unless the surgeon wishes to perform surgical procedures to restore the patients' skulls to normal condition. Then, the FP and MSP of the restored skull may be compared to those of the template skull to assess the difference in alignment.

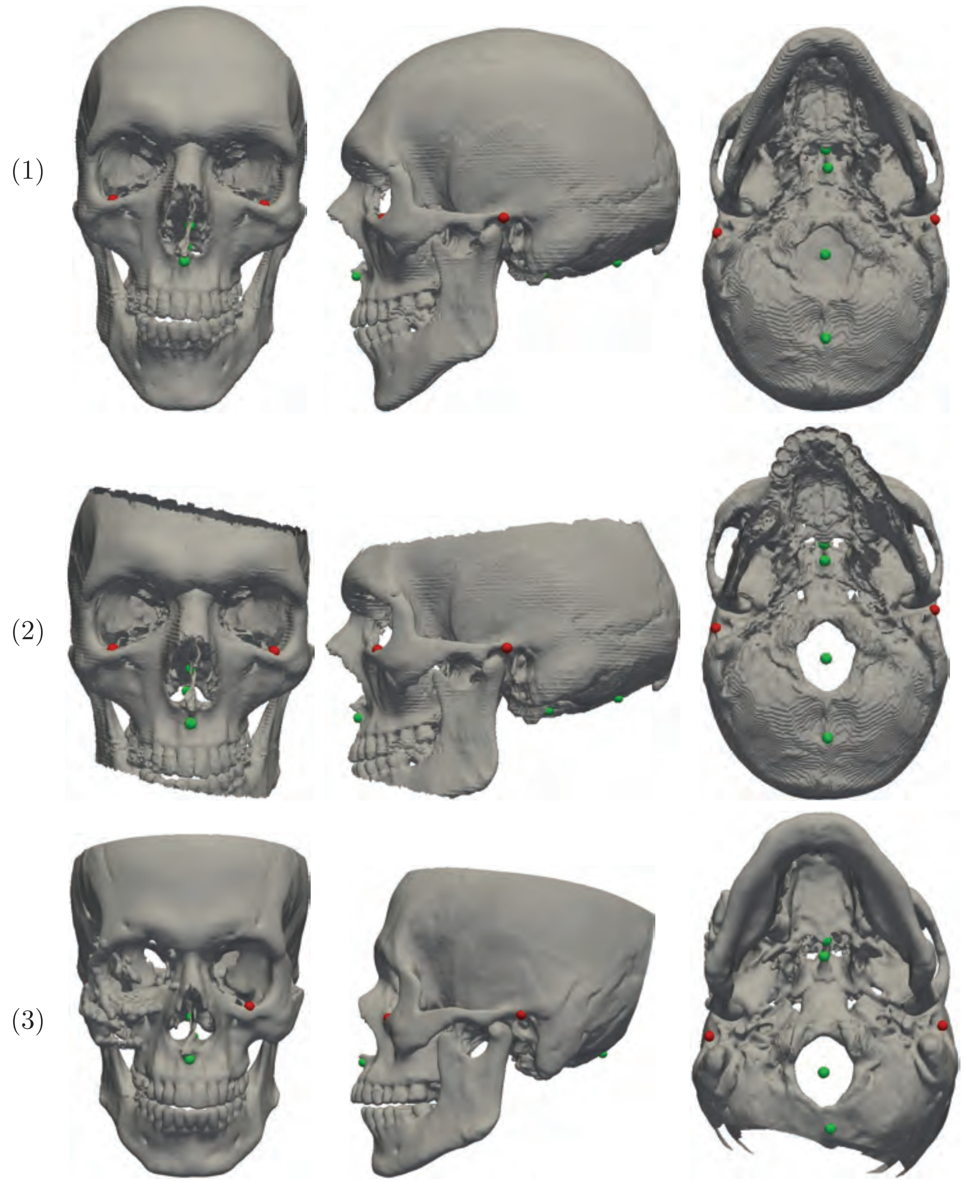


Figure 5.5: Identified FP and MSP landmarks on patients skulls. (1) Full normal skull. (2) Partial normal skull. (3) Patient's skull. (a) Front view. (b) Side view. (c) Bottom view. Green balls indicate the MSP landmarks, and red balls indicate the FP landmarks.

# Chapter 6

# Skull Restoration Algorithm

The skull restoration algorithm is a complex algorithm that iteratively repositions fractured bone fragments. An overview of the algorithm along with its inputs, outputs and desired characteristic of the outputs is first presented in Section 6.1. The desired output characteristics serve as constraints for iterative optimization. The algorithm uses a reference model as a guide by registering it to the patient's deformed skull. Preparation of the reference model and the registration algorithm are described, respectively, in Sections 6.2 and 6.3. The algorithm repositions the fractured bone fragments one at a time in decreasing order of confidence, which is presented in Section 6.4. The restored model should look normal. But the shape of normal healthy skulls varies significantly in details. The study of normal skull shape and the algorithm for ensuring normal shape in the restored model are described in Section 6.5. Section 6.6 presents how the algorithm repositions a single bone fragment. Finally, Section 6.7 presents experimental results and discussions.

## 6.1 Overview of Skull Restoration Algorithm

The inputs to the restoration algorithm include the following:

- Reference Model $F$ (Figure 6.1)
  The reference model $F$ is a mesh model of a normal skull. It has a mid-sagittal plane (MSP) $P_F$ that serves as the laterally symmetric plane. It also contains a subset $S_F$ of surfaces which are the salient surfaces.
- Deformed Model $D$ (Figure 6.2)

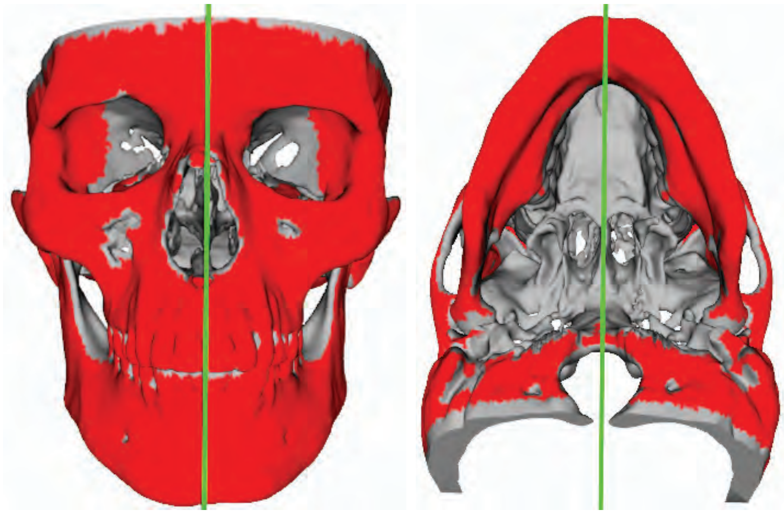

Front Bottom

Figure 6.1: Reference model ASR. Red surfaces are salient surfaces and green line indicates the mid-sagittal plane (MSP).

The deformed model $D$ contains a subset of bone fragment models $B_k$. These bone fragments are divided into a subset of fixed bone fragments and a subset of movable bone fragments. Some movable bones that contain teeth are also known. Each bone fragment has a mesh representing the bone's surface. It also has a subset $S_B$ representing its salient surfaces and a set $L_B$ of anatomical landmarks located on it (Figure 6.2) . $L_B$ can be empty for bone fragments that do not pass through any anatomical plane. There are some holes on the salient surfaces of the upper jaw bones. This is because metal implants in the teeth result in artifacts in the CT images and the mesh models, which are manually removed from the salient surfaces.

The output of the algorithm is the restored model $R$ which is produced by repositioning the movable bone fragments $B_k$ in the deformed model $D$. The restored model $R$ should have the following desired characteristics derived from surgical requirement listed in decreasing order of significance.

1. Anatomical Plane Fitting

   In the restored model $R$, the MSP landmarks should lie on the mid-sagittal plane (MSP) of the skull and FP landmarks should lie on the Frankfurt plane (FP). Before restoration, the bones containing these landmark may be fractured and displaced from their correct positions, and these landmarks may not lie on the corresponding

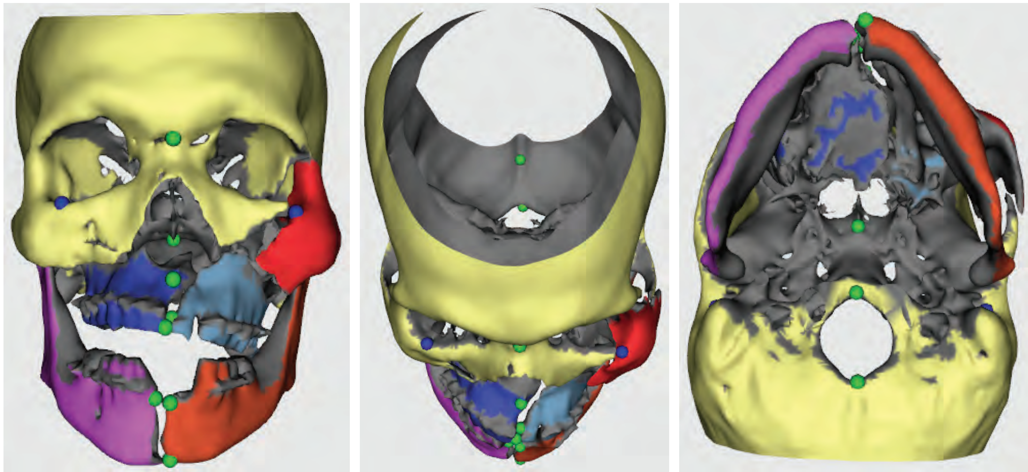

(a) (b) (c)

Figure 6.2: Patients' deformed model. Colored surfaces are salient surfaces of the bones. Small green balls indicate MSP landmarks and blue balls indicate FP landmarks. The yellow bones are the fixed bone, and the other colored bones are movable.

planes. Initially, the MSP landmarks can be checked against the MSP $P_F$ of the reference model $F$. As the algorithm converges toward a good solution, the MSP $P_R$ of the restored model can be computed by fitting it to the MSP landmarks. Likewise, FP can be fitted to the FP landmarks and it should be orthogonal to MSP. Plane fitting errors provide a means of assessing the quality of the restored model in terms of MSP and FP.

2. Normality

   The restored model should look like a normal person's skull. It is noted that there is a wide variation of normal look among people of different ages, genders and racial groups. Section 6.5.1 presents a study of normal skull shapes that motivates the algorithm developed in Section 6.5.2 for estimating normal shape.

3. Surface Continuity

   The salient surfaces of the restored skull should be continuous. That is, the salient surfaces of any two adjacent bone fragments should flush against each other. This constraint is implemented algorithmically together with the estimation of normal shape (Section 6.5.2).

4. Lateral Symmetry

   The restored model $R$ should be laterally symmetric with respect to the MSP. In the restoration algorithm, lateral symmetry of $R$ is considered together with the normality of $R$ when generating the estimated normal shape (Section 6.5.2).

5. Minimum Collision

   Physically, bones do not penetrate each other. Nevertheless, a CMF surgeon may opt to shave off a part of a bone if necessary to restore the patient's skull. So, collision between the bones in the restored model should be minimized but not necessarily completely avoided.

The restoration algorithm is an iterative optimization algorithm that repositions each bone fragment one at a time. An overview of the algorithm is as follows:

---

**Algorithm 2: Skull Restoration Algorithm**

1. Initialize the restored model $R$ as the deformed model $D$, i.e., $R \leftarrow D$.
2. Repeat until convergence:
   (a) Register reference model $F$ to the restored model $R$ by plane-fitting registration (Section 6.3).
   (b) Find corresponding points $c(p)$ on $R$ for points $p$ on $F$.
   (c) Compute MSP and FP of $R$.
   (d) Mark fixed bone fragments as confident and movable bone fragments as nonconfident.
   (e) Compute bone restoration order (Section 6.4).
   (f) For each nonconfident bone $B$ in decreasing order:
      i. Generate the estimated normal surface $M_B$ around bone $B$ (Section 6.5.2).
      ii. Register bone $B$ to $M_B$ by surface continuity-constrained registration (Section 6.6).
      iii. Mark bone $B$ as confident.

---

The skull restoration algorithm first initializes the restored model $R$ as the deformed model $D$. Next, it registers the reference model $F$ to the restored model $R$, which is initially the same as the deformed model $D$, using the plane-fitting registration algorithm that is robust to the difference between $F$ and $R$ (Section 6.3). After registration, the restoration algorithm finds the closest point on $R$ as the corresponding point $c(p)$ for each point $p$ on $F$. Then, it computes MSP and FP of $R$ based on the MSP of $F$. Specifically, the MSP of $F$ is transferred to $R$ and regarded as the MSP of $R$. FP is computed by fitting it to the FP landmarks while constraining it to be orthogonal to MSP in the same manner as described in Section 5.1.4. Then, the registration algorithm marks fixed bones as confident and movable bones as nonconfident and computes the repositioning order of the nonconfident bones (Section 6.4). It uses the confident bones to determine the optimal poses of adjacent nonconfident bones.

For each nonconfident bone $B$ in decreasing order, the restoration algorithm estimates a normal surface $M_B$ around $B$ (Section 6.5) based on the surfaces of the reference model $F$ that best enforces the constraints of normality, surface continuity and lateral symmetry. Next, it computes the correspondence between the salient surface $S_B$ of $B$ and the estimated normal surface $M_B$, and applies a surface continuity-constrained registration algorithm to register $B$ to $M_B$ (Section 6.6) in a manner that satisfies surface continuity and the anatomical plane fitting. Then, bone $B$ is marked as confident, and another nonconfident bone is repositioned.

In the current implementation, collision avoidance is not explicitly enforced because preliminary tests show that collision detection is a computationally expensive task. In the ideal case that the estimated normal surface are correct and the algorithm correctly registers the fractured bone fragments to the estimated normal surfaces, these bone fragments should naturally not collide.

## 6.2 Preparation of Reference Model

Reference models are built separately for the lower jaw and the skull. This is because the joint between the lower jaw and the skull allows for relative movement. First, 3D mesh models of the skull and the lower jaw are segmented from CT images and reconstructed (Figure 6.1). Next, a human expert indicates a set of MSP landmarks on the models using our planning GUI. The MSP is then fitted to the MSP landmarks by minimizing its mean squared distance to the landmarks. The origin of the plane is the mean position of these landmarks, and the normal of the plane is the principal component corresponding to the

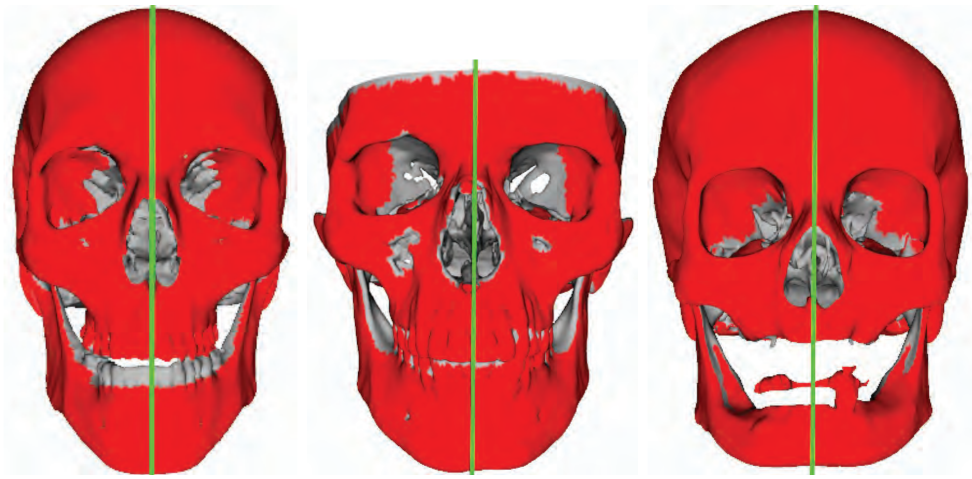

(a) (b) (c)

Figure 6.3: Reference models used by the skull restoration algorithm. (a) ADAM, (b) ASR, and (c) MANIX.

smallest eigenvalue of the covariance matrix of these landmarks. With the fitted MSP, the laterally symmetrical corresponding points $p$ and $s(p)$ are computed by reflecting $p$ with respect to the MSP, and determining the reflected point's closest point $s(p)$ on the reference model.

Salient surfaces of the reference model are identified in a similar manner as that of the patient's deformed model (Section 4.1). For the reference model, all the salient surfaces are identified (Figure 6.1). Salient surfaces are used by the restoration algorithm to check for normality, surface continuity and lateral symmetry of the restored model.

In practice, multiple reference models are prepared. Given a patient's deformed model, the reference model that is most similar is used by the algorithm. In the current implementation, 3 reference models are generated (Figure 6.3). Each reference model contains about $120,000$ vertices and $250,000$ faces totally, of which about $20,000$ vertices and $40,000$ faces belong to the salient surfaces.

## 6.3 Plane-Fitting Registration

Reference model $F$ and patient's deformed model $D$ can differ in size and shape details, due to the deformation caused by injury, normal variation between individuals and possible incomplete scanning of the patient's skull. The registration algorithm should be robust to these variations, and find the common parts between the two models to align them. In addition, the MSP $P_F$ of the reference model should match the MSP landmarks of the deformed model.

The proposed plane-fitting registration algorithm is an extension of the Fractional Iterative Closest Point (FICP) [PLT07]. FICP is a variant of ICP that is robust to the variation between the skulls. Like ICP, FICP iteratively computes the best similarity transformation that registers the reference model to the patient's model. The difference is that in each iteration, FICP computes the transformation using only a subset of mesh points on the reference model whose distances to the patient's model are the smallest. This set of mesh points is called the inlier set.

FICP minimizes a fractional mean-square distance:

$$E_1 = \left(\frac{|F|}{|G|}\right)^{\lambda} \frac{1}{|G|} \sum_{p \in G} \|T(p) - c(p)\|^2 \tag{6.1}$$

where $F$ is the set of reference model points, $G$ is a subset of $F$ containing only the inliers, $c()$ is the correspondence mapping function of $p$, $T$ is the similarity transformation to be optimized, and $\lambda$ is a constant parameter.

To enforce the matching of the reference MSP to the MSP landmarks of patient's model, a planar fitting error $E_2$ is added to the objective function:

$$E_2 = \frac{1}{|L_C|} \sum_{v \in L_C} d_{\pi}^2(v) \tag{6.2}$$

where $L_C$ is the set of MSP landmarks on the confident bones of $D$, and $d_{\pi}(v)$ is the distance from $v$ to the MSP $\pi$ of the transformed reference model $F$. The overall objective function to be minimized becomes:

$$E_r = E_1 + E_2 \tag{6.3}$$

The transformation $T$ that minimizes $E_r$ is the optimal transformation that registers $F$ to $D$.

Optimizing $E_r$ is a very difficult problem to solve exactly. An approximate algorithm is applied. This algorithm is an extension of FICP algorithm, which iteratively minimizes $E_r$ (Equation 6.3).

Given two sets of points $F$ and $D$ with unknown correspondence, FICP finds the similarity transformation $T$ that minimizes $E_1$ in Equation 6.1 by iteratively performing four steps until convergence:

1. Finds correspondence between $F$ and $D$. Denote $q \in Q$ as corresponding point of $p \in F$, where $q$ is the closet point of $p$.
2. Finds inlier subset $G$ of $F$.
3. Computes similarity transformation $T$ using correspondence of points in $G$.
4. Apply $T$ on all points of $F$.

The proposed algorithm has the same structure as FICP, but differs in algorithm details. In the first step, FICP finds the closest point as corresponding points only for the set $F$ of mesh vertices. In the proposed algorithm, for a mesh vertex $p \in F$, its corresponding point $q \in D$ is the closest point of $p$. On the other hand, for a landmark $q \in L_C$, its corresponding point $p$ of $F$ is the orthogonal projection of $q$ on the MSP $P_F$ of $F$. Let us denote the set of points $p$ as $P$, and the set of corresponding points $q$ as $Q$. In the third step, FICP applies Horn et al.'s algorithm [Hor87] to solve for the optimal $T$ between $P$ and $Q$ that minimizes:

$$E = \sum_{p \in P} \|sRp + t - q\|^2 \tag{6.4}$$

To minimize $E_1$ and $E_2$ at the same time, we introduce weights to Equation 6.4:

$$E = \sum_{p \in P} w_p^2 \|sRp + t - q\|^2 \tag{6.5}$$

where:

$$w_p^2 = \begin{cases} \left(\dfrac{|F|}{|G|}\right)^{\lambda} \dfrac{1}{|G|}, & \text{for } p \in G \\ \\ \dfrac{1}{|L_C|}, & \text{for other } p \end{cases}$$

This minimization can be achieved by adding the weights $w_p$ into Horn et al.'s algorithm where the rotation $R$ and translation $t$, are computed. After computing $s$, $R$ and $t$ the points $p$ are transformed by the similarity transformation:

$$q = sRp + t \tag{6.6}$$

Test in Section 6.7.2 verifies that the algorithm performs satisfactorily.

## 6.4 Repositioning Order

In the deformed model, fixed bones do not need to be repositioned. Thus, they provide useful guide for repositioning other neighboring movable bones.

Consider the example in Figure 6.4. The blue regions are fixed, and the bone fragments $B_1$, $B_2$ and $B_3$ are movable. If the algorithm uses the pose of $B_1$ to determine the pose of $B_2$, it may get the result shown in Figure 6.4(b). In this case, even though the pose of $B_2$ is correct with respect to $B_1$, the poses of the bones $B_1$ and $B_2$ are incorrect with respect to the whole skull. In contrast, the algorithm can first reposition $B_1$ with reference to the shape of its nearby fixed bone (Figure 6.4(c)). After $B_1$ is repositioned, it can be used to guide the repositioning of $B_2$ (Figure 6.4(d)).

In computing the order for repositioning the bone fragments, the following properties are considered:

1. Number of anatomical landmarks on the surface of a bone.
2. Fraction of salient surface vertices whose symmetric points lies on fixed bones. One way to determine the symmetric point is explained in Section 6.5.2.
3. Fraction of salient surface vertices that are at the boundary adjacent to confident bones.

Each of these property gives a score for a bone. These scored are normalized and accumulated to get an overall score. Then, the bone fragments are sorted according to their scores.

To correctly restore the bones that contain the teeth, additional dental knowledge and accurate tooth models are required. These are not considered in this thesis. So restoration of the bones that contain teeth are not as accurate as for other bones that do not have

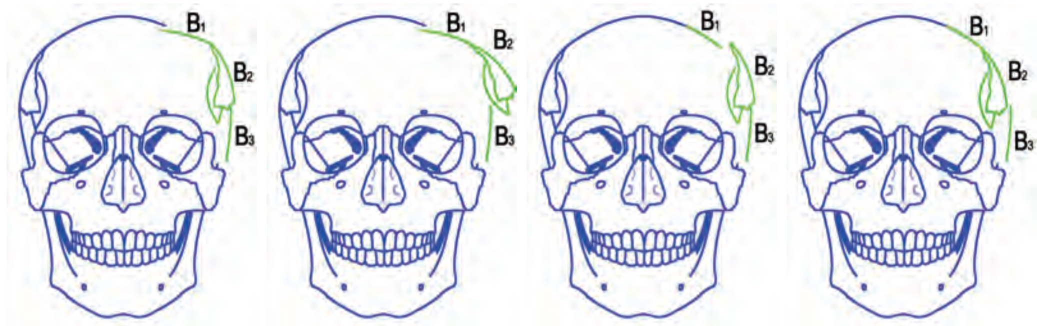


(a) (b) (c) (d)

Figure 6.4: Ordering of the bones to be repositioned. Given a deformed model (a), repositioning a bone that is adjacent to a confident bone produces more reliable result (c, d). Repositioning a bone that is not adjacent to confident bones produces less reliable result (b).

teeth. Therefore, the algorithm repositions the bones that contain teeth last.

## 6.5 Normal Shape of Skulls

Normal human skulls vary significantly in shape details. In order to understand how to incorporate normality constraint into the restoration algorithm, two experiments were conducted to examine the characteristics of normal skulls.

### 6.5.1 Study of Normal Skull Shape

The first experiment was conducted to compare normal skull models of different people. In this experiment, seven healthy skull models were used (Figure 6.5). One of the models was selected as a reference. The other six models were aligned to the reference model using the Fractional Iterative Closest Point algorithm (FICP) [PLT07] (Section 6.3). After alignment, the differences from the vertices of the reference model to their closest points on the surfaces of the aligned target models were computed.

Figure 6.6 shows the differences at the vertices of the reference model using pseudo color. The warmer the color, the larger the difference. It shows that the difference between the normal skull models and the reference model is large in most regions. The mean differences of the six pairs are also large in general (Figure 6.7(a)). These experimental results show that the mean difference of the skull has an average of 2.10 mm. This value

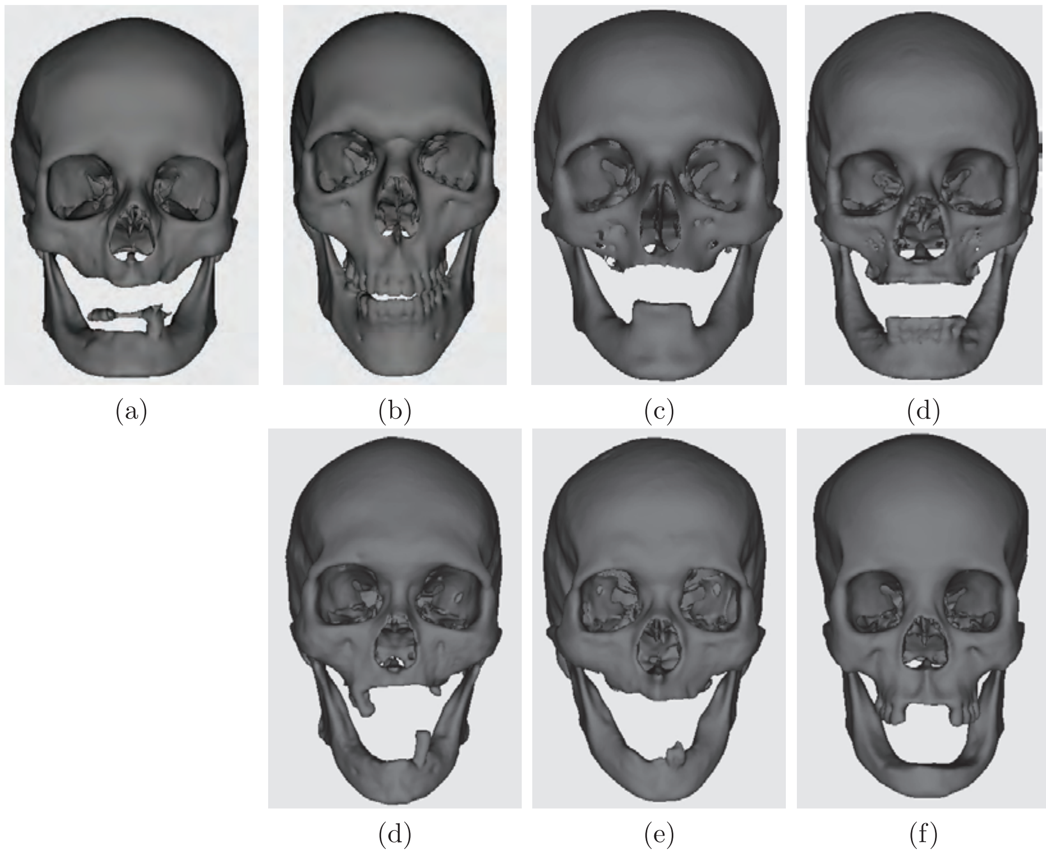


Figure 6.5: Skulls used for the study of normal shape. (a) MANIX. (b) Adam. (c) BWH. (d) Eve. (e) Angio. (f) Brain. (g) TAN.

is large compared to the resolution of the CTs, which is around 0.5 mm. The distribution of the mean difference (Figure 6.7(b)) shows that the mean difference is large in most regions. Therefore, any single normal skull model cannot be used directly to represent the normal shape of another skull.

The second experiment was conducted to examine the local variation of difference. The local variation of difference was defined as the variation between the difference at a vertex of the reference model and the mean difference at its neighboring vertices. It is small if the skulls vary from each other similarly in local regions and large if the skulls vary from each other differently in local regions.

Test results show that the local variation of difference averaged over the test models is 0.78 mm. Figure 6.8 shows that the mean local variation of difference in most regions of the skull is relatively small compared to the mean difference (Figure 6.7). Moreover, the

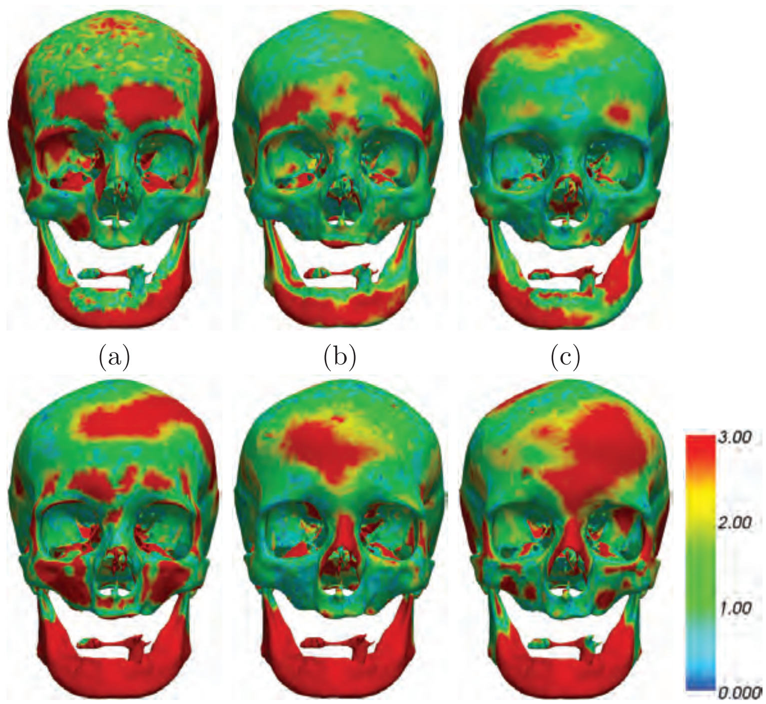


(a) (b) (c)

(d) (e) (f)

Figure 6.6: Difference between normal skull models and a reference model MANIX. Normal skull models differ significantly from reference skull model in many regions. (a) Adam vs. MANIX. (b) BWH vs. MANIX. (c) Eve vs. MANIX. (d) Angio vs. MANIX. (e) Brain vs. MANIX. (f) TAN vs. MANIX.

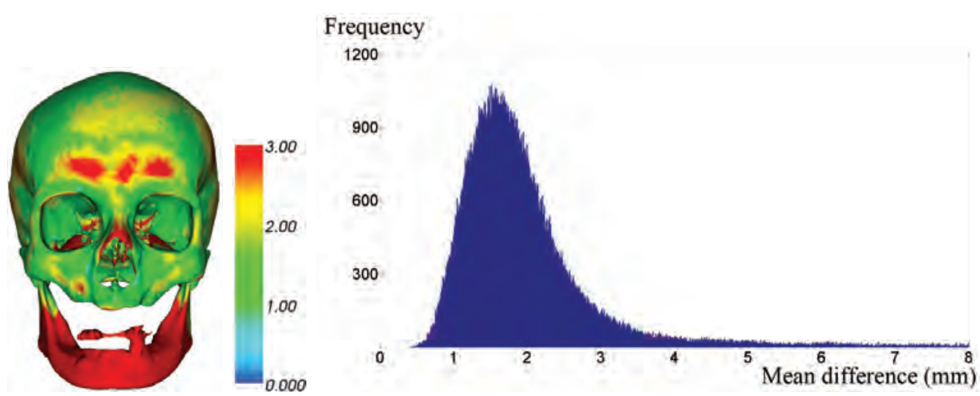


(a) (b)

Figure 6.7: Mean difference of normal skulls. Mean difference is large in most regions. (a) Mean difference. (b) Distribution of mean difference.

mean local variances of difference at most vertices are smaller than the CT resolution of 1 mm (Figure 6.9).

### 6.5.2 Generation of Estimated Normal Surface

The estimated normal surface $M_D$ of the patient's model $D$ is generated from salient surface $S_F$ of reference model $F$ based on the observation of small local variance of difference. The estimated normal surface $M_B$ of a bone fragment $B$ is a subset of $M_D$ around $B$.

First, let us formulate the problem of determining $M_D$. For each point $p$ on $S_F$, its local variance of difference $v(p)$ is given by:

$$v(p) = d(p) - \frac{1}{|N(p)|} \sum_{q \in N(p)} d(q) \tag{6.7}$$

where $N(p)$ is the set of neighboring points of $p$ and $d(p)$ is the difference between the reference model $F$ and the patient's model $D$ at $p$, which is simply:

$$d(p) = p' - p \tag{6.8}$$

where $p'$ the corresponding point on $M_D$ to be estimated. Replacing $d(p)$ with $p' - p$ and $d(q)$ with $q' - q$ yields:

$$v(p) = p' - \frac{1}{|N(p)|} \sum_{q \in N(p)} q' - \left( p - \frac{1}{|N(p)|} \sum_{q \in N(p)} q \right) = l(p') - l(p) \tag{6.9}$$

where $l(p)$ and $l(p')$ are the Laplacian-Beltrami operators at $p$ and $p'$ on $S_F$ and $M_D$, respectively.

To satisfy normality constraint, the magnitude of $v(p)$ should be small for all points $p$. That is, the normality error $E_n$ should be minimized:

$$E_n = \frac{1}{|S_F|} \sum_{p \in S_F} \|v(p)\|^2 = \frac{1}{|S_F|} \sum_{p \in S_F} \|l(p') - l(p)\|^2 \tag{6.10}$$

For a movable bone $B$ of $D$, its estimated normal surface $M_B$ does not coincide with its present surface and has to be estimated. For a fixed bone $B^*$ of $D$, $M_{B^*}$ coincides with the surface of $B^*$, which can be reflected about MSP to serve as a reference for where $M_B$

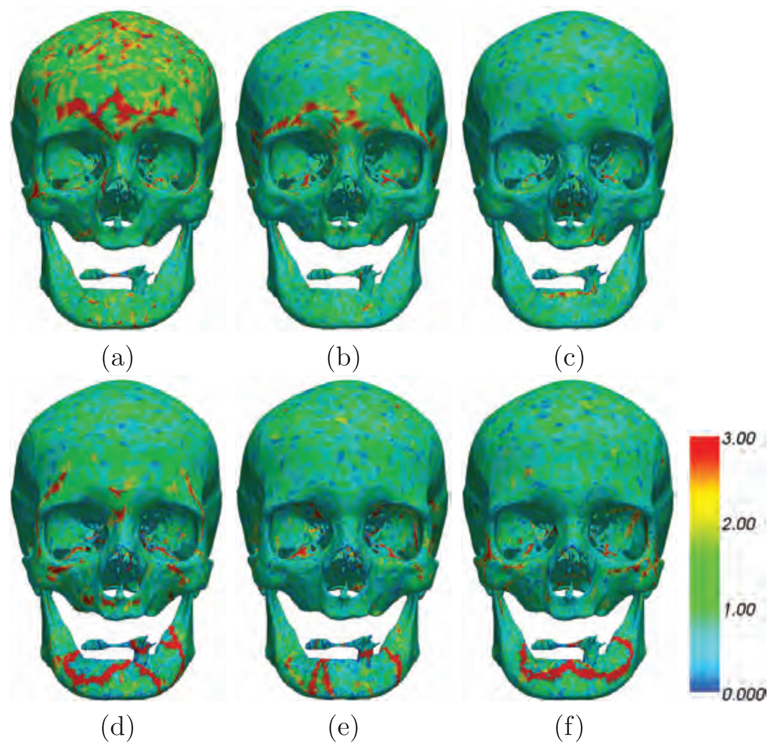


Figure 6.8: Local variation of difference between normal skull models and the reference model MANIX. Local variation of difference is small in most regions. (a) Adam vs. MANIX. (b) BWH vs. MANIX. (c) Eve vs. MANIX. (d) Angio vs. MANIX. (e) Brain vs. MANIX. (f) TAN vs. MANIX.

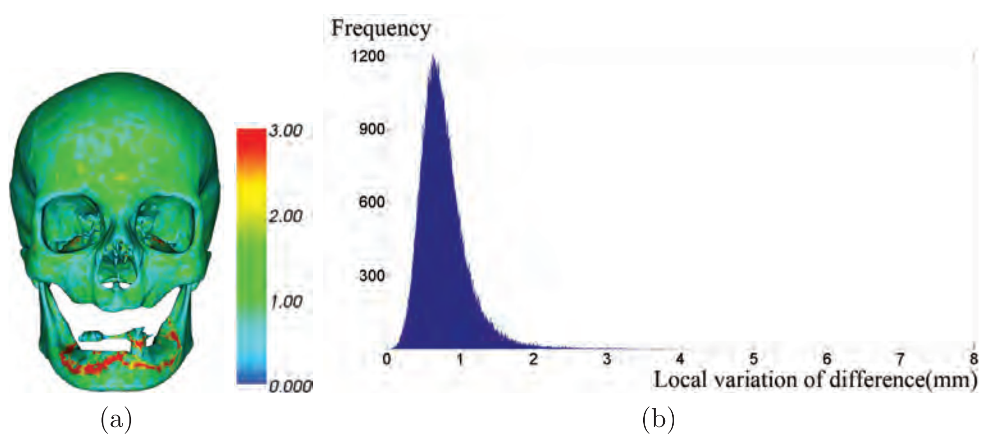


Figure 6.9: Mean local variation of normal skulls. Mean local variation is small in most regions (a) Local variation of difference. (b) Distribution of local variation of difference.

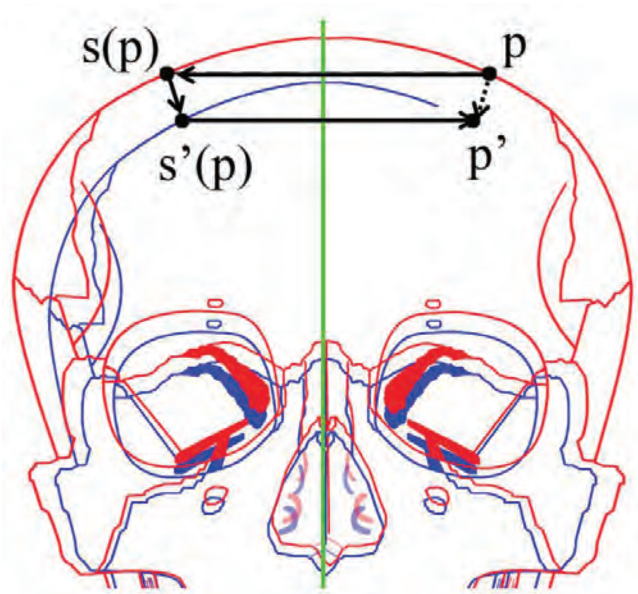


Figure 6.10: The correspondence relationship between symmetry points. $p'$ is a point to be estimated on the normal surface of deformed model, which is a corresponding point of $p$ in reference model (red). Symmetry constraint on $p'$ is computed using $p$ (dash line) by finding the symmetric corresponding point $s(p) \in F$ of $p$, computing the corresponding point $s'(p) \in D$ of $s(p)$ and reflects $s'(p)$ about the MSP (green line) if $s'(p)$ is on a confident bone (blue) of deformed model.

should be. Let $p'$ denote a point on a movable bone $B$'s estimated normal surface $M_B$ whose corresponding point on the reference model $F$ is $p$. Then the symmetric point $s(p)$ of $p$ would have a corresponding point denoted by $s'(p)$. If $s'(p)$ lies on a confident bone, then it can be reflected to serve as a reference for where $p'$ should be. That is, the error between $p'$ and the reflection $r(s'(p))$ of $s'(p)$ should be minimized:

$$E_s = \frac{1}{\|C_F\|} \sum_{s(p) \in C_F} \|p' - r(s'(p))\|^2 \tag{6.11}$$

where $C_F$ is a subset of $S_F$ whose corresponding points $s'(p)$ are on the confident part of the deformed model $D$. Figure 6.10 illustrates the idea of applying symmetry constraint.

The overall error $E_T$ to be minimized is a combination of $E_n$ and $E_s$:

$$E_T = \lambda_n E_n + \lambda_s E_s \tag{6.12}$$

Because normal skulls are not perfectly symmetric, so symmetry is less important than normality. $\lambda_n$ is set to 10 and $\lambda_s$ is set to 1 empirically.

In summary, the problem of generating estimated normal surface is to determine the $M_D = \{p'\}$ that minimizes the error $E_T$.

Laplacian surface deformation [BS08, MYF06, MDSB02, SCOL*04] is a method that solves for the minimization of $E_n$ (Equation 6.10) with hard and soft constraints. It can easily incorporate the linear sum squared error $E_s$ of Equation 6.11 [SCOL*04]. In our case, the problem of estimating the normal surface is solved by deforming $S_F$ to minimize $E_T$.f The $s'(p)$ on the confident bones $B^*$ serve as hard constraints and their reflected points $r(s'(p))$ serve as soft constraints.

The correspondence between $p$ on $S_F$ and $p'$ on $B$ is determined as follows:

1. $p'$ is close to $p$.
2. $p'$ lies near the surface normal of $p$.
3. The surface normal of $p'$ is similar to that of $p$.

After deforming $S_F$, the corresponding points $p'$ are recomputed and this procedure is repeated. Upon convergence, the deformed $S_F$ is $M_D$.

Since $S_F$ is a continuous surface, the $M_D$ estimated by Laplacian surface deformation of $S_F$ is also a continuous surface. Therefore, repositioning $B$ by registering it to $M_B$ automatically satisfies the surface continuity constraint.

## 6.6 Surface Continuity-Constrained Registration

The surface continuity-constrained registration algorithm registers a bone fragment $B$ to the estimated normal surface $M_B$ around $B$ by minimizing normality error and anatomical plane error. Figure 6.11 illustrates the idea.

The normality error $D_n$ is defined as the mean squared difference between the transformed points $T(p')$ of the salient surface $S_B$ of $B$ and their closest points $c(p')$ on the estimated normal surface $M_B$ around $B$:

$$D_n = \frac{1}{|S_B|} \sum_{p' \in S_B} \|T(p') - c(p')\|^2 \tag{6.13}$$

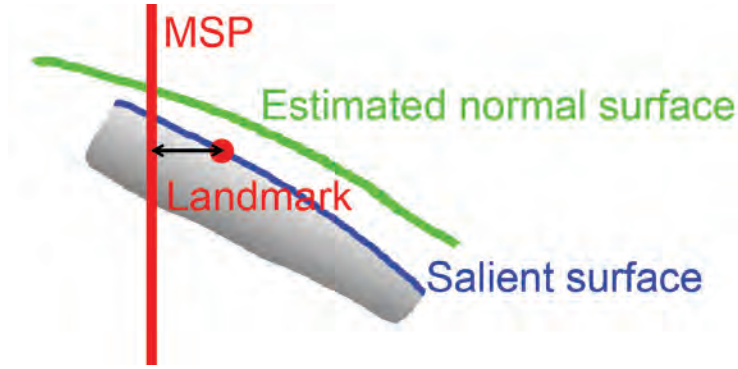


Figure 6.11: Surface continuity-constrained registration. The surface continuity-constrained registration registers a bone fragment to the estimated normal surface around it such that the bone fragment's salient surface (blue) matches the estimated normal surface (green) especially at the boundaries, and the bone fragment's anatomical landmarks (red point) are close to the corresponding anatomical plane (red line).

The normal shape is continuous at its boundaries to confident regions. The algorithm registers $B$ to $M_B$ giving more weights to the points near the boundaries of B adjacent to confident bones. In this way, the boundary regions are close to $M_B$, which satisfies surface continuity. So $D_n$ becomes:

$$D_n = \frac{1}{|S_B|} \sum_{p' \in S_B} w(p') \|T(p') - c(p')\|^2 \tag{6.14}$$

where $w(p')$ is set according to its distance to the $B$'s boundaries adjacent to confident bones. The closer $p'$ is to the boundaries, the larger is the $w(p')$.

The anatomical plane error $D_\pi$ is defined as the mean squared distance from the transformed landmark $T(l)$ in $L_B$ to the corresponding anatomical planes.

$$D_\pi = \frac{1}{|L_B|} \sum_{l \in L_B} d_\pi^2(T(l)) \tag{6.15}$$

where $\pi$ represents the corresponding anatomical plane of $l$, and $d_\pi(T(l))$ is the distance from the transformed landmark $T(l)$ to plane $\pi$. Minimizing $D_\pi$ keeps landmarks $L_B$ close to MSP and FP.

In summary, the surface continuity-constrained registration problem is to find the rigid transformation $T$ that minimizes the following objective function $D$:

$$D = \lambda_n D_n + \lambda_\pi D_\pi \tag{6.16}$$

This problem is similar to the plane-fitting registration algorithm and is solved in an iterative manner similar to the plane-fitting registration algorithm (Section 6.3). Because anatomical plan fitting is the most important, $\lambda_n$ is set to 1 and $\lambda_\pi$ is set to 50 empirically.

## 6.7 Experiments and Discussions

This section presents experiments that test various components of the proposed skull restoration algorithm. Both real and synthetic data were used in the tests. Section 6.7.1 presents the preparation of the synthetic data. Section 6.7.2 to 6.7.5 describe the experiments for testing the plane-fitting registration algorithm, the normal surface estimation algorithm. the surface continuity-constrained registration algorithm, and the whole restoration algorithm.

### 6.7.1 Preparation of Synthetic Data

Six normal skull models were used to generate synthetic data, three from a local hospital, two from Visible Human Project, and one from OsiriX. One model was used as the reference (Fig. 6.12). The other five were manually cut in a manner similar to real fractures in patients to synthesize five fractured skulls for quantitative evaluation (Figure 6.13). There were 4, 3, 3, 2 and 2 fractured bone fragments, respectively, in BWH, Brain, EVE, Angio and TAN. The fractured bones were manually displaced to simulate the displacement caused by impact injuries. Figure 6.13 shows that all the fractured bone fragments were displaced except the fixed bones. The deformed models were verified by a CMF surgeon and served as test inputs while the original models served as the ground truth.

### 6.7.2 Plane-Fitting Registration

An experiment was conducted to evaluate the proposed plane-fitting registration algorithm. Three seriously fractured skulls were used in this experiment, and they were real patients from National University Hospital. For patients' privacy, their skull models were

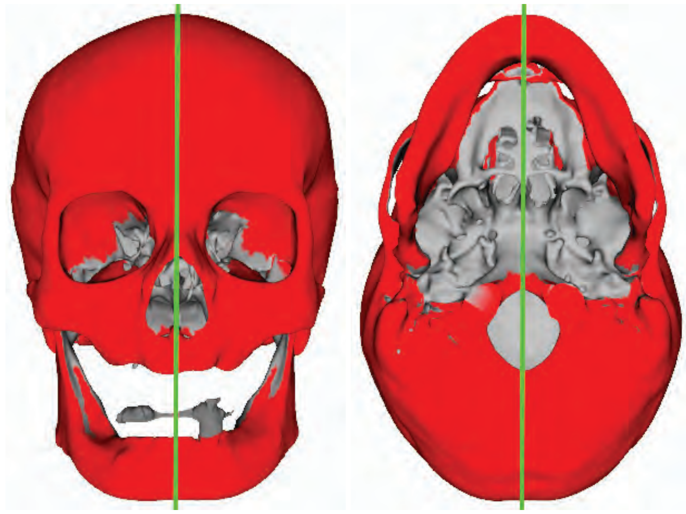


Figure 6.12: Reference model for synthetic data test. Red surfaces are the salient surfaces. Green line indicates the mid-sagittal plane (MSP).

anonymized and given different identification codes, namely NAV, NUH and SAMK. Note that the top parts of the patients' heads were not scanned, resulting in incomplete skull models (Figure 6.15). All of them had injuries on both side of their skulls. The test was performed on the skulls excluding the lower jaw because most of the MSP and FP landmarks were located in the skull. In the skull region, NAV had three fractured movable bones, whereas NUH and SAMK had 9 and 10 bones respectively. The severity of the injuries increased from NAV to NUH to SAMK. The fractured fragments of SAMK were displaced furthest from their original positions.

Among the three reference models prepared (Section 6.2), the reference model ASR was used for NAV and SAMK, and reference model Adam was used for NUH based on their similarity. The proposed plane-fitting registration algorithm was compared to two existing similarity registration algorithms, namely ICP [BM92] and FICP [PLT07]. These three algorithms were applied to align the reference models to the patients' deformed models.

To quantitatively evaluate the algorithms, three errors were measured. Surface error $E_S$ measured the root mean squared distance between the corresponding surfaces of two models, and MSP fitting error $E_P$ measured the root mean squared distance from the patients' MSP landmarks to the reference models' MSPs. The registration error of NAV

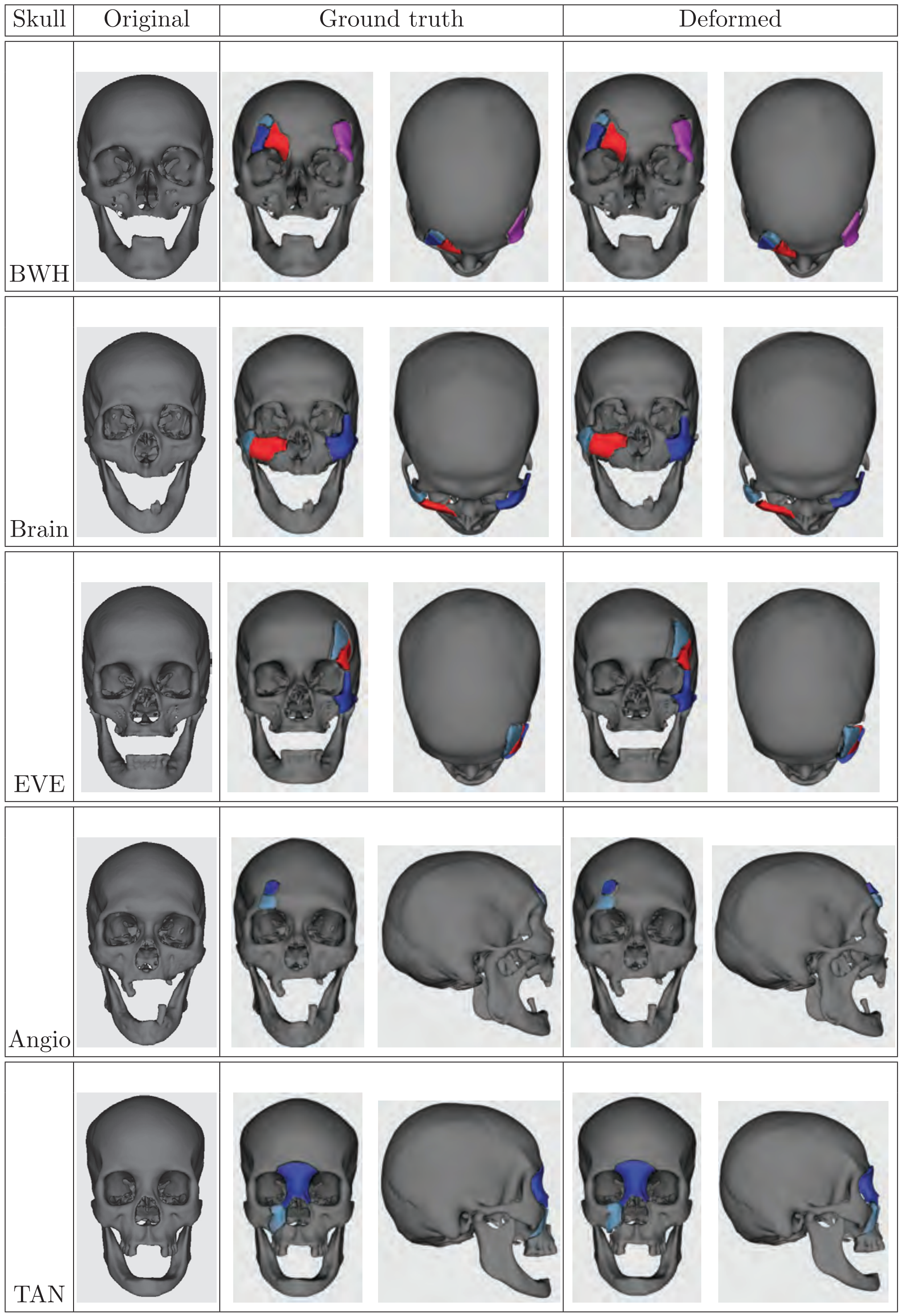


Figure 6.13: Synthetic deformed skull models and their ground truth models. Movable bones (colored) are displaced from their original positions whereas fixed bones (gray) are not displaced.

was measured for the intermediate results after each iteration according to the objective function (Equation 6.3) to examine the convergency of the algorithm. Execution time was measured on a PC with a 3.4GHz CPU.

ICP registration results were greatly affected by the incompleteness and fractures of the models (Figure 6.15). For NUH case, ICP shrunk the reference model to a small region, and failed to find reasonable alignment between the reference and the patient's model. Due to inaccurate alignment, the MSP $P_F$ of reference model were not accurately aligned with the MSP landmarks on the fixed bones of the patients' models. ICP had the lowest surface error $E_S$ because it minimized the distance for the full set of mesh vertices. However, ICP did not take in account MSP fitting, resulting in large MSP fitting error $E_P$ (Table 6.1).

FICP was robust to outliers and obtained relatively good alignment between the reference models and patients' models (Figure 6.15). It had larger surface error $E_S$ (Table 6.1). Alignment between the reference models' MSPs and the patient models' MSP landmarks were not accurate and has large MSP fitting error $E_P$ (Table 6.1), because FICP did not consider MSP fitting in the registration process.

The proposed plane-fitting registration algorithm inherited its robustness from FICP. In addition to robustly registering the reference models to the deformed models, it also matched the MSPs of the reference models to the patients' MSP landmarks accurately (Figure 6.15). It was more robust to outliers than did FICP due to the fitting of MSP. The outliers that violated the fitting of MSP were also identified and excluded from the computation of similarity transformation. Therefore, the MSPs of the reference models were aligned accurately to the patients' MSP landmarks, and the inlier surface points were robustly registered, resulting in the lowest MSP fitting error and similar surface error compared to FICP (Table 6.1).

The convergence curve (Figure 6.14) shows that registration error decreased in the first 10 iterations, and quickly converged to a stable value after about 50 iterations. Execution time for each iteration was about 10 ms, and the algorithm took about 0.5 second to converge.

Table 6.1: Comparison of registration methods. $E_S$ denotes surface error (mm), and $E_P$ denotes MSP fitting error (mm). The proposed plane-fitting registration algorithm attained the overall best performance with the lowest plane-fitting error $E_P$ and satisfactory surface error $E_S$

| skull model | ICP | | FICP | | Proposed | |
|---|---|---|---|---|---|---|
| | $E_S$ | $E_P$ | $E_S$ | $E_P$ | $E_S$ | $E_P$ |
| NAV | **2.71** | 0.83 | 2.73 | 0.96 | 2.73 | **0.65** |
| NUH | **2.17** | 2.71 | 2.68 | 1.83 | 2.71 | **1.29** |
| SAMK | **5.85** | 8.49 | 15.25 | 3.53 | 15.55 | **1.88** |
| Average | **3.58** | 4.01 | 6.89 | 2.11 | 7.00 | **1.27** |

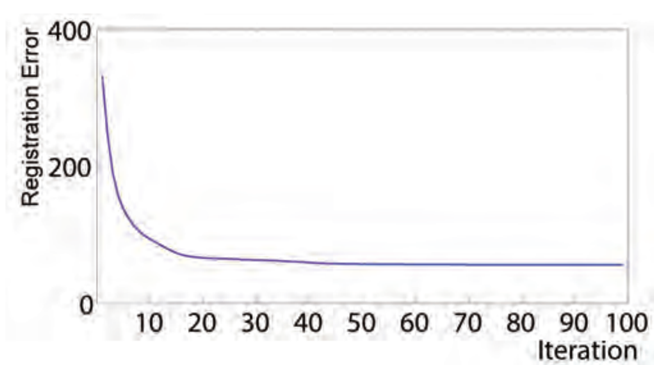


Figure 6.14: Convergence curve of plane-fitting registration. Registration error decreases rapidly and converges to a stable value.

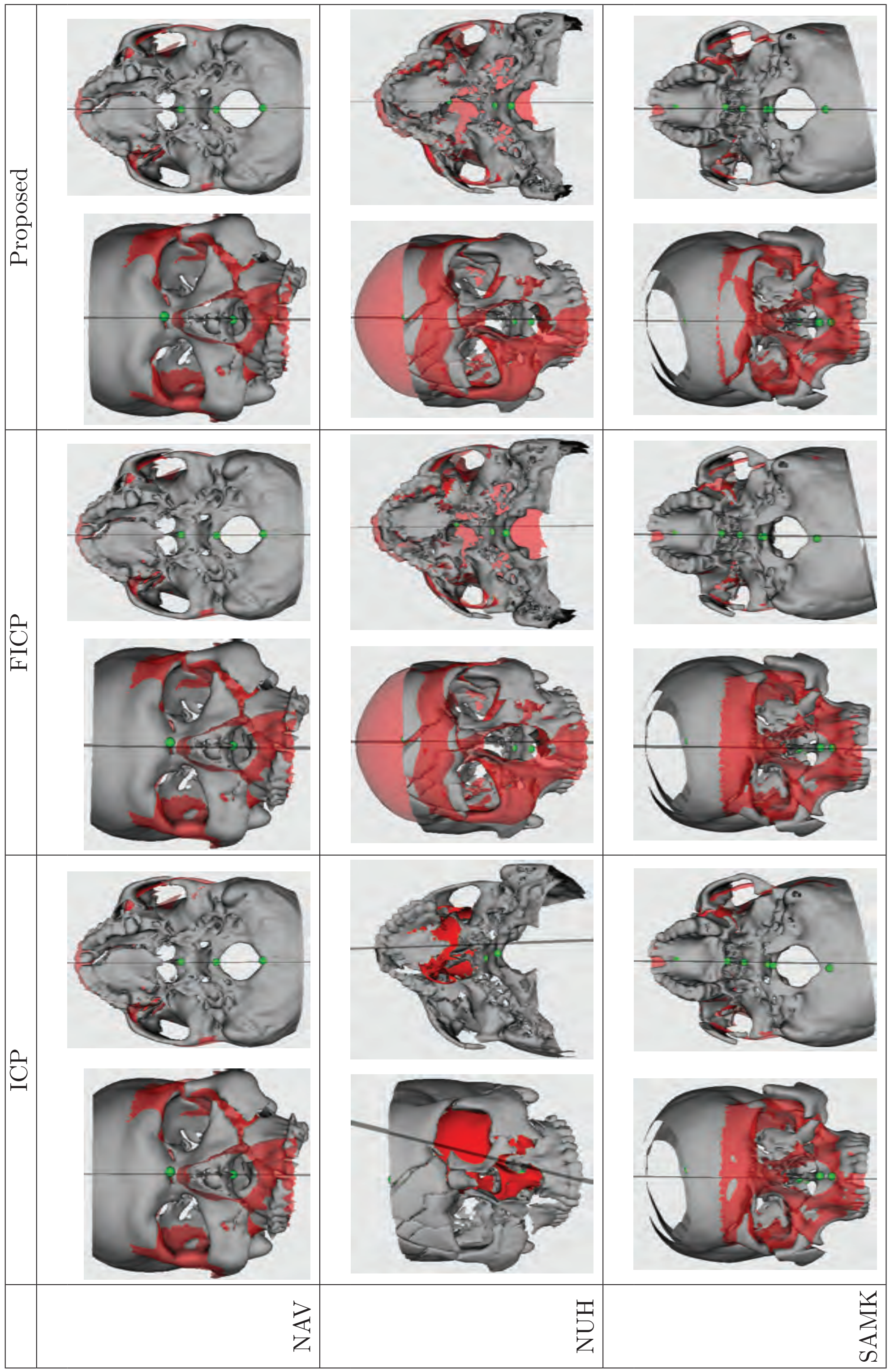


Figure 6.15: Plane-fitting registration results. The proposed plane-fitting registration algorithm attained the best overall performance compared to ICP and FICP. It aligned the reference models' MSP (gray lines) accurately to the deformed models' MSP landmarks (green balls). Salient surfaces of the reference models are colored red and the deformed models are colored gray.

Table 6.2: Comparison of normal estimation methods. This table tabulates the normal surface estimation errors (mm). The proposed algorithm generates the most accurate estimation of normal surfaces.

| skull | BWH | Brain | EVE | Angio | TAN | Average |
|---|---|---|---|---|---|---|
| Proposed | **0.81** | **1.17** | **1.30** | **0.88** | **1.93** | **1.23** |
| Reflection | – | – | 1.75 | 1.32 | – | 1.54 |
| Reference | 1.30 | 1.38 | 1.86 | 1.52 | 2.77 | 1.77 |

### 6.7.3 Generation of Estimated Normal Surfaces

An experiment was conducted to evaluate the accuracy and convergency of normal surface estimation algorithm (Section 6.5.2) using synthetic data (Section 6.7.1). The fixed bones of the deformed models were marked as confident bones, and all other displaced bones were marked as nonconfident bones. The reference models were aligned to the patients' deformed models using the plane-fitting registration algorithm. Then the normal estimation algorithm was applied.

For comparison two other methods were used to generate the estimated normal surfaces. The first method simply used the surfaces of the registered reference model as the estimated normal surface. The second method reflected healthy parts of the deformed model and used the reflected surface as the estimated normal surface. Estimation error was measured on the estimated normal surfaces as the mean surface distance from them to the actual normal surfaces of the patients. It was also measured for the estimated normal surfaces of BWH model after each iteration to evaluate convergence. Execution time was measured on a PC with a 3.4GHz CPU.

The estimated normal surfaces produced by the proposed algorithm were normal and symmetric (Figure 6.16). In addition, the confident bones were flushed at the bone boundaries. In contrast, the normal surfaces estimated by the reflection method were not flushed with the confident bones at the bone boundaries (Figure 6.17).

The proposed normal surface estimation method had the lowest error for all test models (Table 6.2). The reference model had the largest error due to significant variation among normal human skulls. The reflection method uses the patient's specific shape on the healthy side. However, due to natural asymmetry in human skulls, reflection was not as accurate as the proposed method which considers not only symmetry but also normality

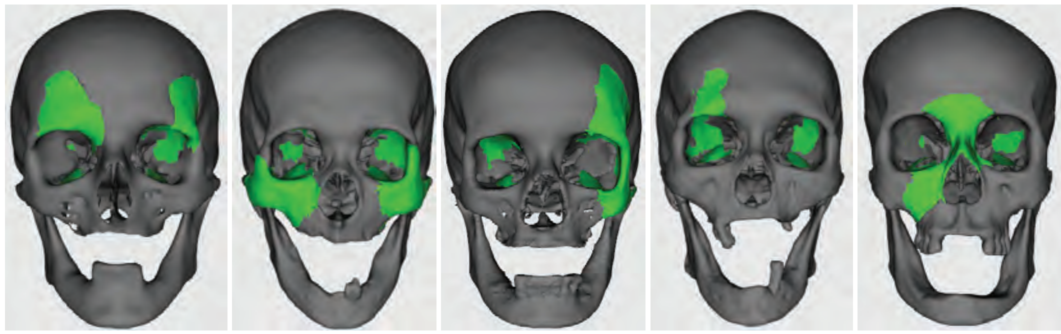

BWH Brain EVE Angio TAN

Figure 6.16: Estimated normal surfaces generated by the proposed algorithm. The estimated normal surfaces (green) looks normal and flushes with the confident bones (gray) at the bone boundaries.

(1)

(2)

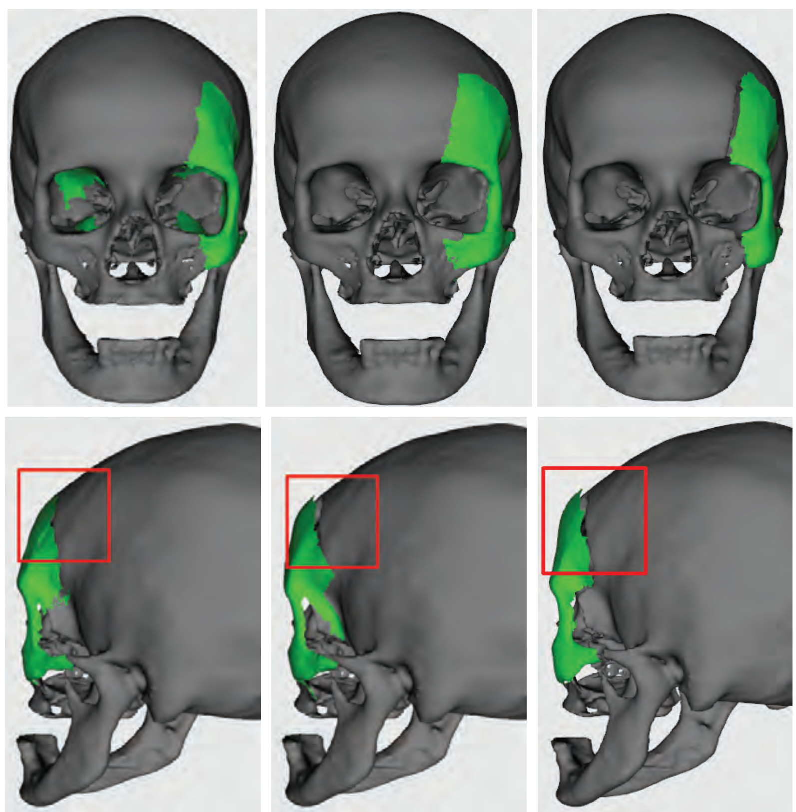

(a) (b) (c)

Figure 6.17: Comparison of various methods for generating estimated normal surface. (a) The normal surface estimated by the proposed algorithm flushes with adjacent confident bones (gray). (b, c) On the other hand, estimated surface generated by reflection method and registered reference surface are not flushed with adjacent confident bones.

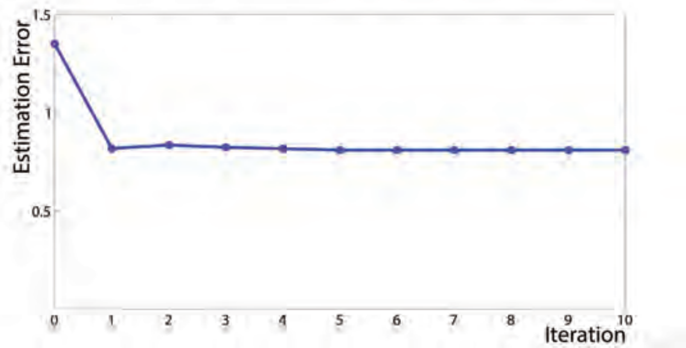


(a)

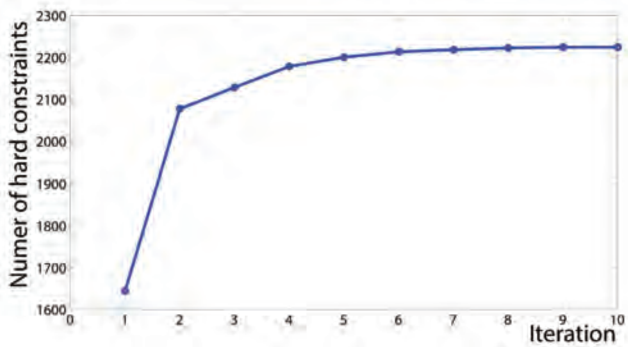


(b)

Figure 6.18: Convergence curves of normal surface generation algorithm. (a) Estimation error decreases rapidly and converges to a stable value. (b) Number of hard constraints increases as the algorithm iterates and converges to a stable value.

and surface continuity. More importantly, reflection method is not applicable to skulls with bilateral fractures.

Figure 6.18 shows the convergence curves for the estimated normal surface generation algorithm. Initially, the number of hard constraints was small because the reference model was significantly different from the patient's model. As Laplacian surface deformation deformed the salient surfaces of the reference model to match the deformed model using more hard constraints, the quality of the estimated normal surface improved. The number of hard constraints increased rapidly in the first iterations and converged after 9 iterations. However, after about 3 iterations, the number of hard constraints was large enough and the normal estimation error converged to a small value after 3 iteratoins. The estimated normal surface generation algorithm took about 1-2 minutes because it involves solving a large sparse linear system and took about 3-6 minutes to converge.

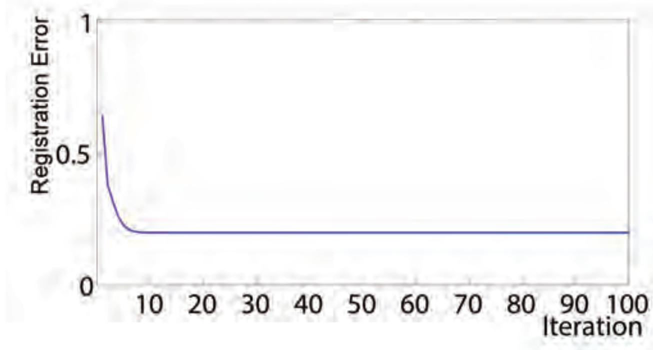


Figure 6.19: Convergence curve of surface continuity-constrained registration. Registration error decrease rapidly and converges to a stable value.

### 6.7.4 Surface Continuity-Constrained Registration

An experiment was conducted to evaluate the performance of the surface continuity-constrained registration algorithm (Section 6.6). The BWH model was used in this experiment. The estimated normal shape for the fractured bone fragment located at the left upper eye socket was first generated using the normal surface estimation algorithm. Then, the bone fragment was registered to the estimated normal surface using the proposed surface continuity-constrained registration algorithm. Registration error was measured using the objective function defined in Equation 6.16 for the intermediate result after each iteration. Execution time was measured on a PC with a 3.4GHz CPU.

Registration error decreased rapidly in the first few iterations and converged to a stable value after about 50 iterations (Figure 6.19). The surface continuity-constrained registration algorithm spent about 30 ms for each iteration, and it converged in about 1.5 seconds.

In a preliminary work, a Monte Carlo algorithm was implemented to reposition each bone fragment instead of estimating normal surface and registering bone fragment to the estimated surface. In each iteration, the preliminary algorithm took about 20 ms to compute errors in terms of anatomical plane fitting, normality, surface continuity and symmetry, which was roughly the same as the current algorithm. However, Monte Carlo algorithm required a much larger number of iterations ($\geq 30,000$) to converge, which made it much slower than the current algorithm. Since the Monte Carlo algorithm did not automatically avoid collision, collision detection was included using the vtkbioeng software package [Pan01]. Collision detection took about 70 ms in each iteration, adding to the overall computation time of the Monte Carlo method.

### 6.7.5 Skull Restoration Algorithm

An experiment was conducted to evaluate the skull restoration algorithm. The proposed skull restoration algorithm was applied to five synthetic deformed models (Section 6.7.1. Three quantitative measures were computed, namely restoration error, volume overlap and symmetry error. Restoration error was measured as the average distance from the restored models to the ground truth models. Volume overlap measured the overlap in volume between the fractured bones in the restored models and the corresponding ground-truth. Symmetry error measured the amount of asymmetry of the restored model with respect to MSP in the fractured region. It was computed as the mean surface distance between the fractured bones and their reflection on the other side. Surface distances from the intermediate restored models to the ground truth models were also computed to assess the convergence of the algorithm. Execution time was measured on a PC with a 3.4GHz CPU.

The skull restoration algorithm does not explicitly detect collisions of the restored bone fragments. Instead, it relies on the accurate estimation of normal surfaces and registration of bone fragments to the estimated normal surface to naturally avoid collisions. A test was performed to examine whether collisions were indeed avoided. Collision error was measured for each fractured bone as the percentage of the volume of the bone that collided with adjacent bones.

Test results show that the skull restoration algorithm repositioned the fractured bone fragments correctly, which improved the normality, surface continuity and lateral symmetry compared to the deformed models (Figure 6.20). It had small restoration error, and improved the symmetry error and volume overlap compared to the deformed model (Table 6.3). The restoration error of 0.76 mm can be considered accurate since the best resolution of the CT images used in the experiments is 1 mm. The restored models were similar to the ground truth models in most regions (Figure 6.21(2)). In comparison, the differences between the deformed models and the ground truth models (Figure 6.21 (1)) in most regions were larger than that of the restored models.

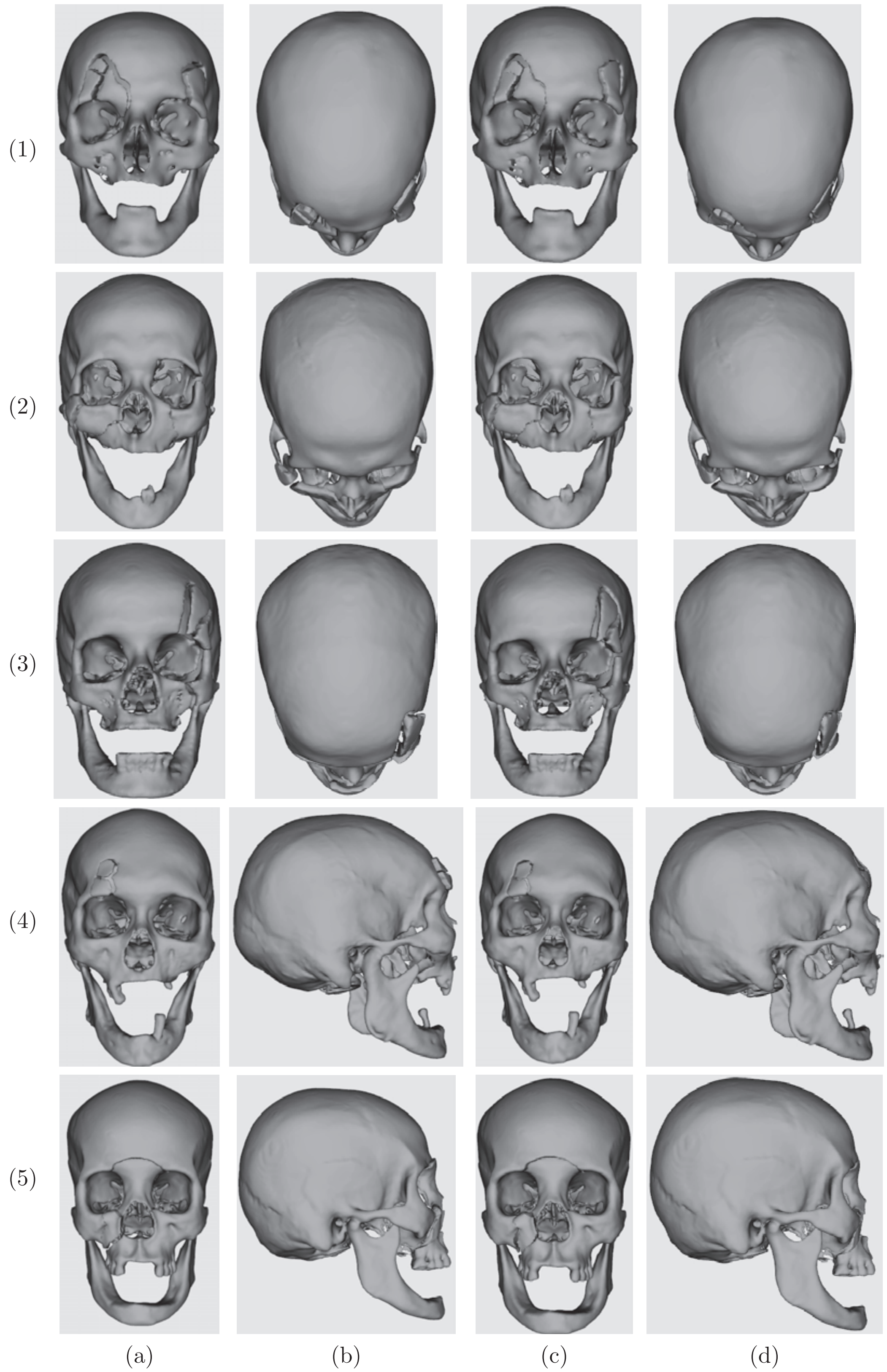


Figure 6.20: Restored models generated by the skull restoration algorithm. The restored models (c, d) show significant improvement in terms of normality, surface continuity and lateral symmetry compared to the deformed models (a, b) Qualitative evaluation of restored models. (1) BWH, (2) Brain, (3) EVE, (4) Angio, (5) TAN.

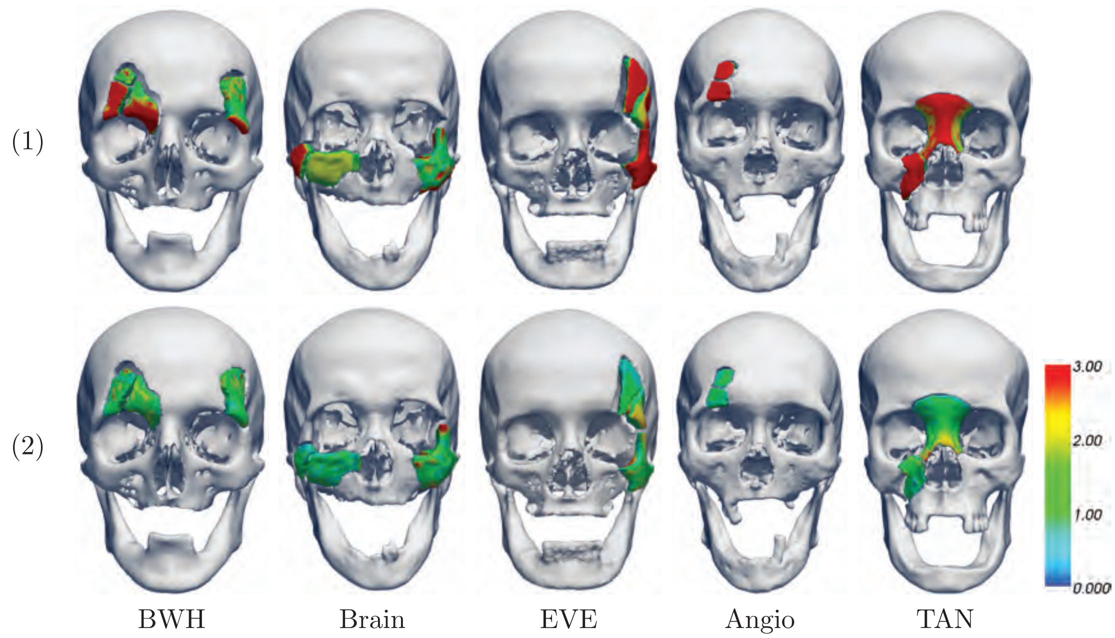


Figure 6.21: The restored models (1) are more similar to the ground truth models than do the deformed models (2). The warmer the color, the larger is the difference.

Table 6.3: Quantitative evaluation of the skull restoration algorithm. The skull restoration algorithm has the smaller restoration error (SD) and symmetry error (SE), and larger volume overlap (VO).

| Skull | | VO (%) | SD (mm) | SE (mm) |
|---|---|---|---|---|
| BWH | Deformed | 71.90 | 1.34 | 1.58 |
| | Restored | 95.76 | 0.78 | 1.44 |
| Brain | Deformed | 32.10 | 2.16 | 3.23 |
| | Restored | 76.63 | 0.86 | 1.07 |
| EVE | Deformed | 43.43 | 2.37 | 1.74 |
| | Restored | 78.36 | 1.40 | 1.43 |
| Angio | Deformed | 34.20 | 1.53 | 1.82 |
| | Restored | 86.33 | 0.54 | 1.23 |
| TAN | Deformed | 74.69 | 1.70 | 1.40 |
| | Restored | 91.97 | 0.45 | 0.93 |
| Mean | Deformed | 51.26 | 2.59 | 1.95 |
| | Restored | 85.30 | 0.76 | 1.21 |

Figure 6.22 shows the convergence curves for the five test cases. The restoration error dropped quickly and stabilized at a small value after about 3 iterations. The restoration algorithm did not guarantee the decrease of error in every iteration. Therefore, in some cases, the error of the first iteration was slightly smaller than the error of subsequent iterations (BWH and Angio). These results indicated that 3 iterations are enough for the algorithm to produce good converged restored models. All convergence curves of the components of the skull restoration algorithm shows that they converged very quickly, which is a property of good optimization algorithm.

In the skull restoration algorithm, the plane-fitting registration took about 0.5 seconds to converge. the surface continuity-constrained registration took 0.6 seconds to converge, while the estimated normal surfaces generation took 3-6 minutes to converge. The execution time for one iteration varied from 10 minutes to 20 minutes depending on the number of movable bone fragments in the deformed model. The restoration algorithm generated good results in about 30 minutes to 1 hour. Despite the significant execution time, it could still meet the requirement for real surgical applications where pre-operative planning is usually performed a few days before the actual surgery.

For most fractured bone fragments in the restored models, the collision error and the collision volume were very small (Table 6.4). Two bone fragments in BWH collided more than the others (Figure 6.23). Their collision error was relatively large compared to those of other bone fragments. The bone highlighted in light blue could be moved higher to avoid collision with the bone below. Future work should investigate efficient method to avoid collision without having to check for collisions for all bones because it is a computationally expensive process.

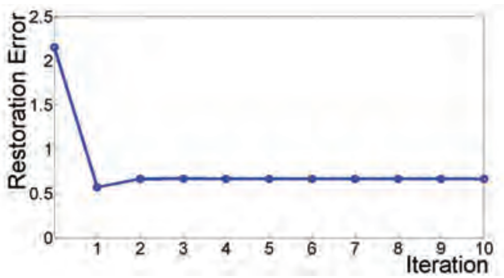


BWH

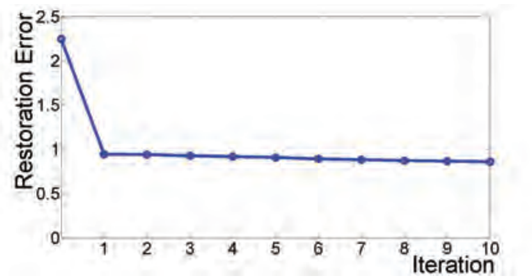


Brain

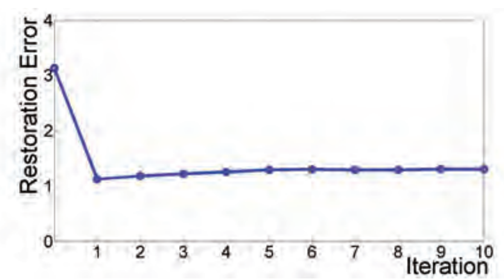


EVE

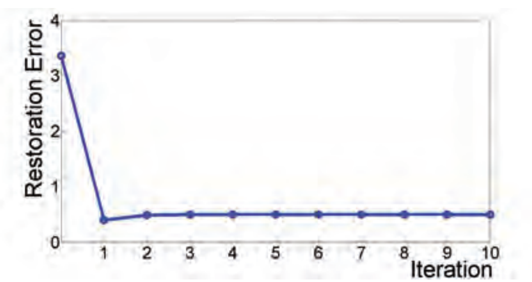


Angio

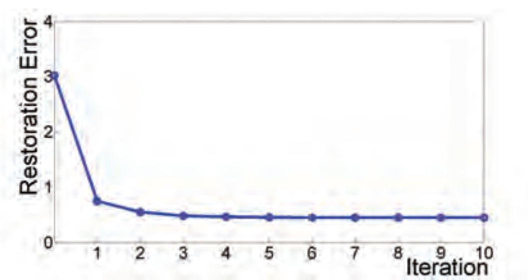


TAN

Figure 6.22: Convergence curves of skull restoration algorithm. All restoration errors decrease rapidly and converge to stable values.

Table 6.4: Fraction of collision. Bone volume and collision volume are measured in $cm^2$. Collision error is the ratio percentage of collision volume over bone volume. Collision error is small for most bones.

| Model | Collision error | Bone | | | |
|---|---|---|---|---|---|
| | | 1 | 2 | 3 | 4 |
| BWH | Collision volume | 0.23 | 0.22 | 0.002 | 0.002 |
| | Bone volume | 2.58 | 1.03 | 4.29 | 6.91 |
| | Collision error | **8.94** | **21.70** | **0.05** | **0.02** |
| Brain | Collision volume | 0.02 | 0 | 0.01 | |
| | Bone volume | 7.33 | 2.33 | 3.08 | |
| | Collision error | **0.31** | **0** | **0.15** | |
| EVE | Collision volume | 0 | 0 | 0 | |
| | Bone volume | 4.74 | 3.74 | 4.23 | |
| | Collision error | **0** | **0** | **0** | |
| Angio | Collision volume | 0.02 | 0 | | |
| | Bone volume | 0.94 | 1.10 | | |
| | Collision error | **2.40** | **0** | | |
| TAN | Collision volume | 0 | 0.10 | | |
| | Bone volume | 10.97 | 1.51 | | |
| | Collision error | **0** | **6.42** | | |

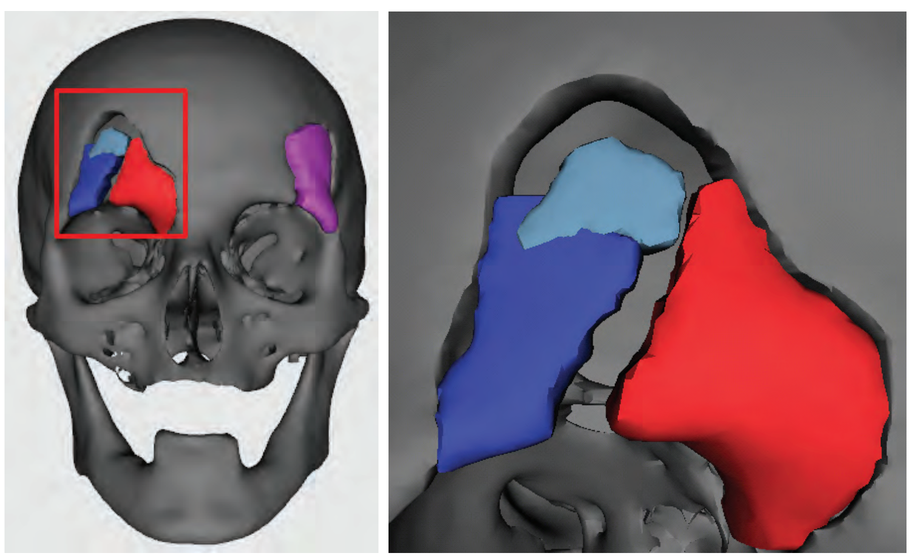

(a) (b)

Figure 6.23: Collision at top right of the restored BWH model. The region highlighted in red box in (a) is shown in (b). The bone marked in light blue can be moved up to avoid collision to the bone below.

### 6.7.6 Reference Skull Selection

An experiment was conducted to test the impact of reference model selection on restoration quality. This experiment used EVE's synthetic deformed model and three reference models. The three reference models included EVE's normal model, MANIX and ADAM. Among them, EVE's normal model was used to represent a ground truth case where patient's normal model was available. It also helped to explore the possibility of using a patient's twin sibling's skull as reference. The other two reference models MANIX and ADAM were used to represent reference models with different variations from EVE. Comparing to ADAM, MANIX looked more similar to EVE.

The restoration algorithm was applied to restore the deformed EVE model given the three reference models in turn. Four measurements were measured on the reference models and the restored models: healthy difference (DH) and fractured difference (DF) were used to measure the difference between the reference models and EVE's deformed model in healthy and fractured regions, restoration error (SD) and volume overlap (VO) were used to assess the restoration quality by comparing the restored models with the ground truth models.

Table 6.5 shows the experimental results. ADAM model was the most different from the deformed model's healthy region and resulted in the worst restoration result that had the smallest VO and the largest SD.

MANIX model was more similar to the deformed model's healthy region comparing to ADAM. Using it as the reference model, the restoration algorithm produced better restoration result that had larger VO and smaller SD.

EVE reference model was the most similar to the deformed model's healthy region. Using it as the reference model, the restoration algorithm produced the best restoration result that had the largest VO and the smallest SD.

In summary, the more similar the reference model is to the deformed model, the better the restoration result. In the ideal case where the patient's normal model or his twin sibling's normal model is available, the algorithm produces the best restoration result.

In practise, both the patient's normal model and his twin sibling's normal model are difficult to acquire. The patient's normal skull before injury is typically unavailable unless

Table 6.5: Selection of Reference Model. Small difference in the healthy part (DH) relates to high quality restoration results with large volume overlap (VO) and small restoration error.

| | Reference vs. Deformed | | Restored vs. Groundtruth | |
|---|---|---|---|---|
| Reference Model | DH (mm) | DF (mm) | VO (%) | SD (mm) |
| EVE | 0.07 | 3.31 | 93.14 | 0.92 |
| MANIX | 2.78 | 6.57 | 78.36 | 1.40 |
| ADAM | 3.87 | 4.03 | 71.22 | 1.62 |

he has undergone CT or MRI scan due to other head-related diseases prior to the injury. The same is true for his sibling's normal skull. Even if his sibling is willing to subject himself to CT or MRI scan, it may still be difficult to scan because priority is given to real patients.

# Chapter 7

# Validation

In practice, CMF surgeons reposition only major bone fragments and leave the smaller pieces untouched. After CMF surgery, CMF surgeons evaluate the quality of CMF surgery results by visually examining the normal look and symmetry of the restored skulls, and measuring symmetry errors. The same evaluation scheme is used in this chapter to validate the performance of the proposed skull restoration algorithm.

## 7.1 Real Patient Data

Four sets of real patient data with different amounts of fractures were used for the validation. These four patients have been operated by the collaborating surgeon.

The first set was ABM (Figure 7.1(a)). The patient's outer right orbital region was fractured into a small bone fragment, and this bone fragment was selected to be repositioned. Post-operative CT was not available for this patient.

The second set was AKM (Figure 7.1(b)). The patient's outer right orbital region and right zygomatic arch were fractured into many small bone fragments, and these bone fragment were displaced outward. Among these fractured bone fragments, 4 were selected to be repositioned. Post-operative CT was available for this patient.

The third patient was NAV (Figure 7.1(c)). The patient suffered from an accident which broke his left cheek bone, upper jaw and lower jaw. The left cheek bone was broken into many pieces, dropped down and displaced outward. The upper jaw was broken into

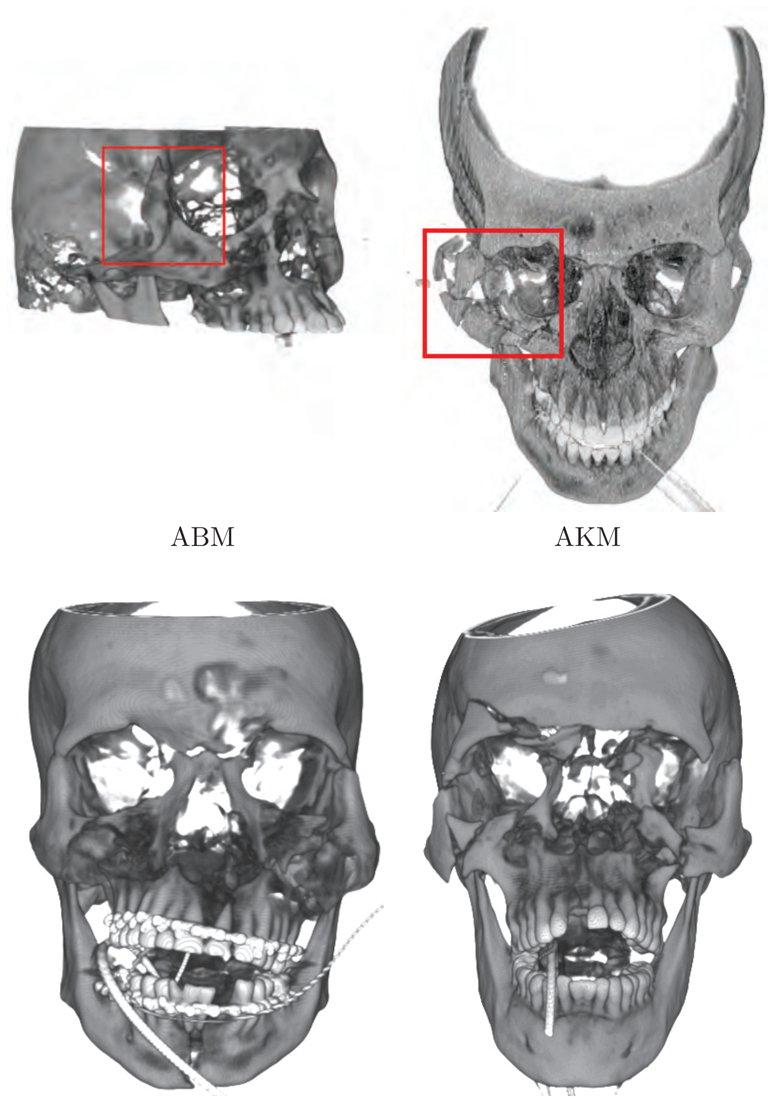

ABM AKM

NAV SAMK

Figure 7.1: Volume rendering of real patients' CT images for validation. Some skulls are unilaterally fracture (ABM and AKM) whereas some other skulls are bilaterally fractured (NAV and SAMK).

Table 7.1: Real patient data used for validation. The amounts of fractures increases from ABM to SAMK. Post-operative CT was available for one unilateral fracture case (AKM) and one bilateral fracture case (SAMK).

| Patient | Fracture type | Number of bones repositioned | Post-operative CT |
|---|---|---|---|
| ABM | unilateral | 1 | No |
| AKM | unilateral | 4 | Yes |
| NAV | bilateral | 5 | No |
| SAMK | bilateral | 11 | Yes |

several pieces and dropped down. The lower jaw was broken into several pieces near the middle. In total, 5 fractured bone fragments were selected to be repositioned: one at the right cheek, 2 from the upper jaw and 2 from the lower jaw. No post-operative CT of this patient was available.

The fourth patient was SAMK (Figure 7.1(d)). The middle part of the skull was fractured into many small pieces. Some of them sunk into the skull, and some of them were displaced very far away from their original positions. From the fractured bone fragments, 11 major ones were selected to be repositioned. Post-operative CT was available for this patient.

For the cases with post-operative CT, post-operative models were generated using thresholding algorithm for validation. Note that the difference in the qualities of the pre and post-operative CT images and segmentation error resulted in differences between the pre-operative and post-operative models in the regions where the surgeon did not operated on. Table 7.1 summaries the real patient test data in increasing order of number of bones to be repositioned.

## 7.2 Qualitative and Quantitative Evaluation

In practice, surgeons measure symmetric error in terms of 4 measurements from the bottom view of the skulls (Figure 7.2). First of all, the surgeon identifies the midline structure called vomer. Then, the surgeon draws a horizontal line that passes through the vomer, and measures the distances $LH$ and $RH$ from the vomer to the most lateral points on the two zygomatic arches. The symmetry error measures the absolute difference between

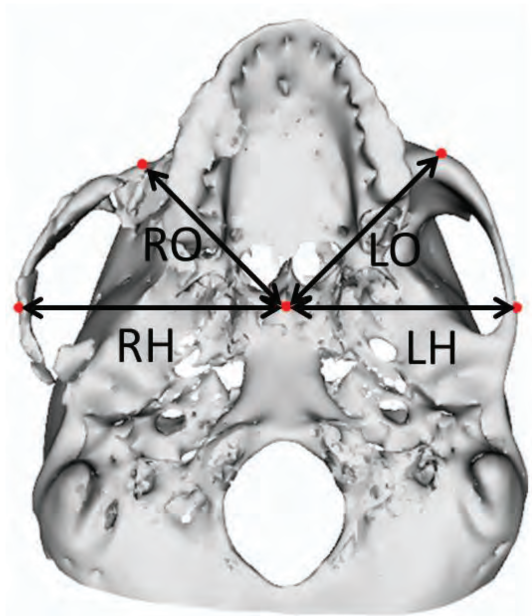


Figure 7.2: Surgeon's assessment of symmetry error at bottom view.

$LH$ and $RH$. The surgeon also draws two lines from the vomer at 45 degrees to the horizontal line measures the distances $LO$ and $RO$ from the vomer to the two most anterior intersection points of these lines with the skulls. The symmetry error $DO$ measures the absolute difference between $LO$ and $RO$.

For patient ABM, the restoration algorithm repositioned correctly the small fractured bone fragment, resulting in a normal structure at the eye socket (Figure 7.3). ABM's fracture regions were not visible from the bottom view, so all the symmetry measurements on the deformed model and the restored model were the same (Table 7.2). The difference of the measures on the two sides shows the natural asymmetry of the skull.

For patient AKM, the zygomatic arch (red boxes) and the outer boundary of right eye socket (green boxes) were restored to a normal shape (Figure 7.4). The restored model looked similar to the postoperative CT (Figure 7.4). The measurements on the restored model showed better symmetry than did the deformed model (Table 7.3). The symmetry error $DH$ was reduced significantly from 11.2 mm to 2.3 mm, and the error $DO$ was also reduced from 4.3 mm to 1.3 mm. In addition, its two symmetry errors were smaller than that of the post-operative model (Figure 7.7).

For patient NAV, the restored model was more normal and symmetric than the de-

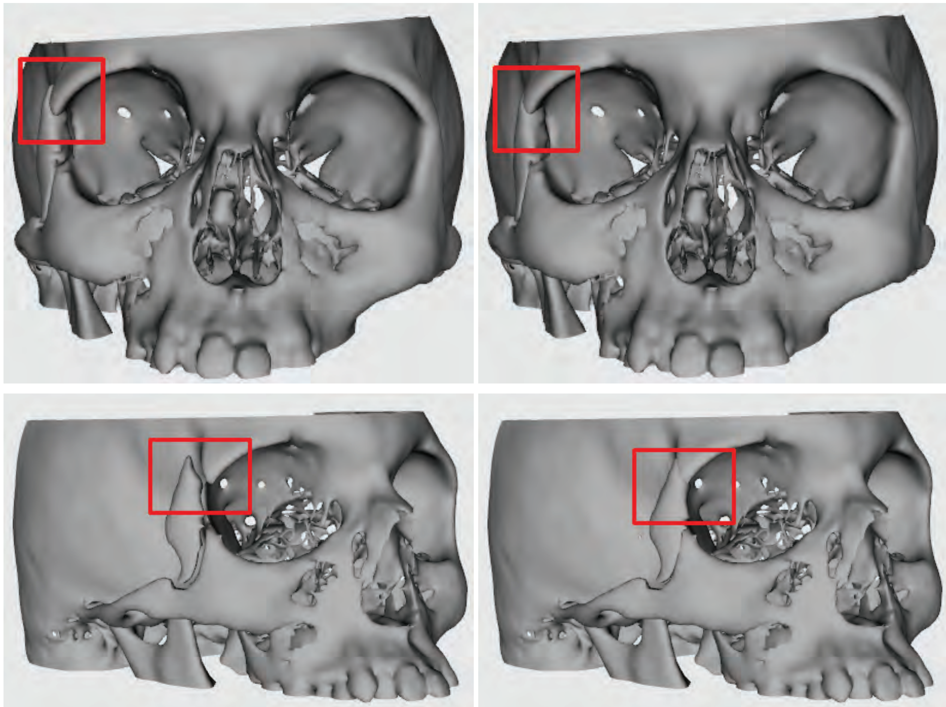

Deformed model Restored model

Figure 7.3: Restoration result of ABM. The fractured bone is correctly restored (red).

Table 7.2: Symmetry measurements for ABM. The symmetry measures are the same for deformed and restored models because fracture to ABM does not affect these measures.

| Model | LH | RH | DH | LO | RO | DO |
|---|---|---|---|---|---|---|
| Deformed | 65.2 | 65.6 | **0.4** | 166.9 | 158.4 | **8.5** |
| Restored | 65.2 | 65.6 | **0.4** | 166.9 | 158.4 | **8.5** |

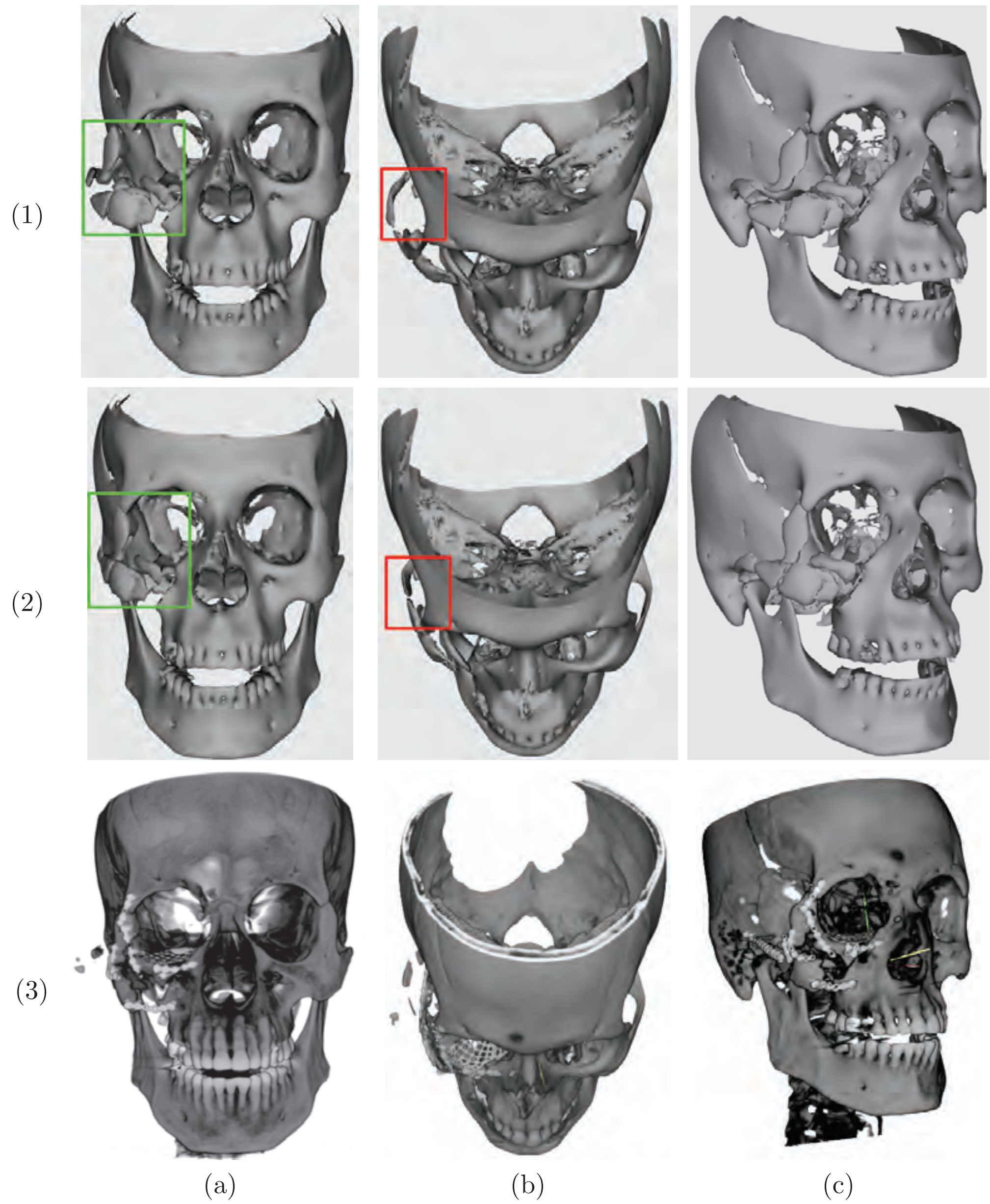


Figure 7.4: Restoration result of AKM. In the deformed model (1), the outer eye socket (green box) and the zygomatic arch (red box) look abnormal, which are restored by the skull restoration algorithm and appear normal in the restored model (2). The restored model is similar to the post-operative skull (3).

Table 7.3: Symmetry measurements for AKM. Length measures are in mm. Both restored model and post-operative models; symmetry error is smaller than that of deformed model. And restored models's symmetry error is also smaller than the restored model.

| Model | LH | RH | DH | LO | RO | DO |
|---|---|---|---|---|---|---|
| Deformed | 66.7 | 77.9 | 11.2 | 63.5 | 59.2 | 4.3 |
| Restored | 66.7 | 69.0 | **2.3** | 63.5 | 62.2 | **1.3** |
| Post-operative | 68.0 | 70.6 | 2.6 | 68.5 | 71.3 | 2.8 |

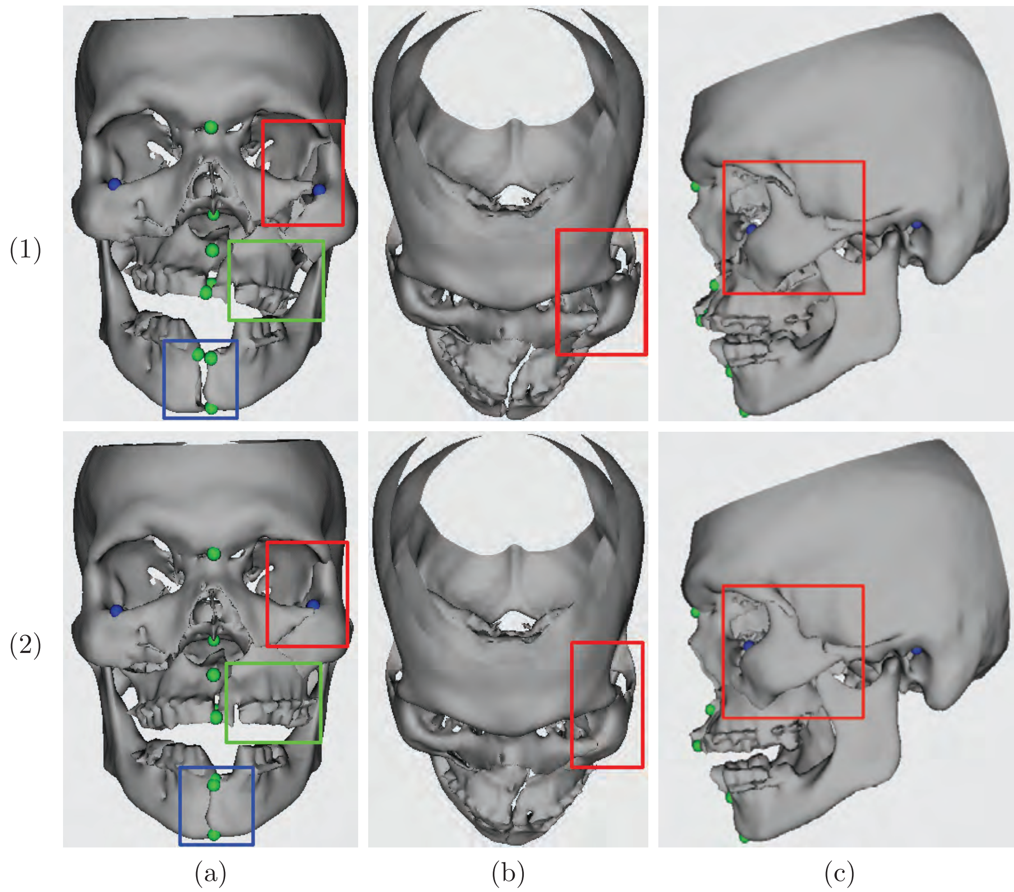


Figure 7.5: Deformed and restored models of NAV. In the boxes regions, the restored models (2)is normal and the deformed model (1) is abnormal. In the restored model, the MSP landmarks (green balls) and FP landmarks (red balls) lie on the correct planes. In the deformed model, the MSP and FP landmarks do not lie on the correct planes.

Table 7.4: Symmetry measurements for NAV. The restored model's symmetry error DO is reduced.

| Model | LH | RH | DH | LO | RO | DO |
|---|---|---|---|---|---|---|
| Deformed | 61.6 | 63.8 | **2.2** | 67.0 | 61.4 | 5.6 |
| Restored | 61.6 | 63.8 | **2.2** | 64.9 | 61.4 | **3.5** |

formed model (Figure 7.5). The left cheek bone fragment was pulled up and joined smoothly with adjacent bones (red boxes). The upper jaw bones were joined together and pulled up to the proper position (green boxes). The lower jaw bones were also properly joined (blue boxes). NAV's fracture caused large symmetry error $DO$ of 5.6 mm, and the restoration reduced it to 3.5 mm (Table 7.4). In addition, in the restored model, the MSP and FP landmarks were closer to the MSP and FP of the model.

For patient SAMK, in the restored model, the fractured out bone fragments of the deformed model were assembled together forming a normal and symmetric shape (Figure 7.6). The left zygomatic arch was aligned properly at the correct position (red). The right cheek bone was joined smoothly with the bones above it (yellow box). In addition, he MSP and FP landmarks were aligned with the MSP and FP. The restoration algorithm reduced SAMK's symmetry errors $DH$ and $DO$ significantly from 10.0 mm and 8.4 mm to 4.1 mm and 2.1 mm, respectively. In addition, its symmetry error $DO$ were smaller than that of the post-operative model (Figure 7.7).

In the restored skull the the left nose bone (blue box) and the bone at the right zygomatic arch (green box) were not repositioned to optimal position and orientation. Nevertheless, they looked similar to the post-operative skull.

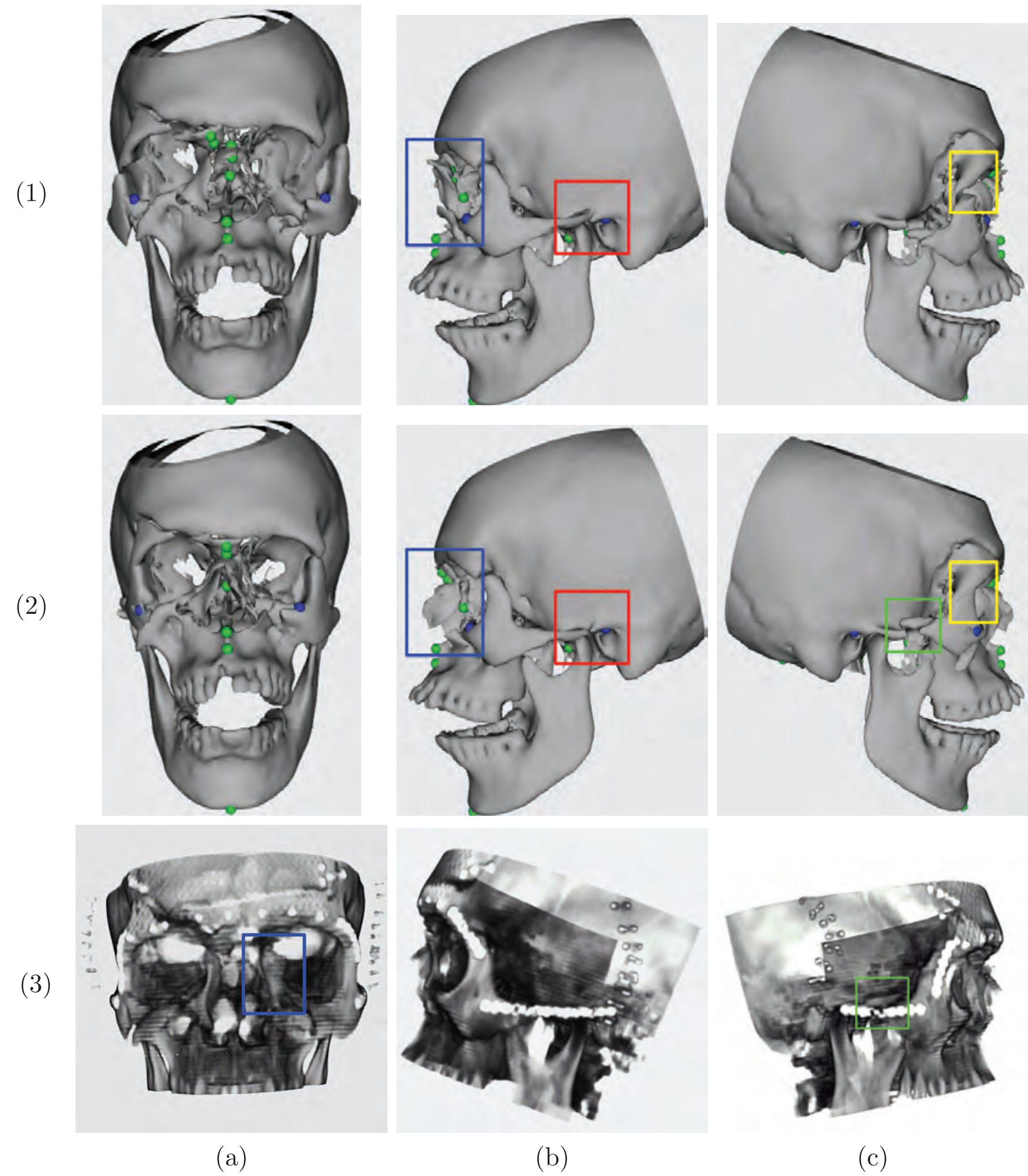


Figure 7.6: Qualitative evaluation on SAMK. (1) Deformed model. (2) Restored model. (3) Post-operative CT volume. Green balls indicate MSP landmarks. Blue balls indicate FP landmarks.

Table 7.5: Symmetry measurements for SAMK. The restored model has the lowest symmetry error DH and DO.

| Model | LH | RH | DH | LO | RO | DO |
|---|---|---|---|---|---|---|
| Deformed | 69.3 | 59.3 | 10.0 | 57.7 | 49.3 | 8.4 |
| Restored | 60.5 | 56.3 | 4.2 | 51.4 | 49.3 | **2.1** |
| Post-operative | 61.5 | 58.9 | **2.6** | 53.0 | 49.0 | 4.0 |

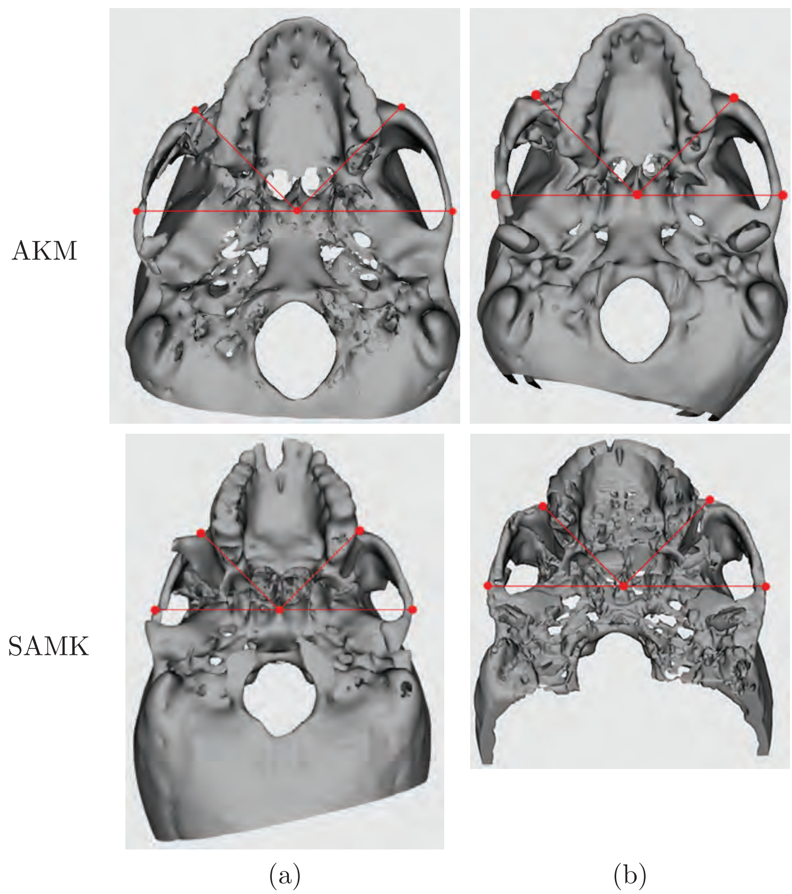


Figure 7.7: Measurement of symmetry error. The restored models (a) has smaller error than post-operative skulls (b) for some symmetry error measures.

# Chapter 8

# Limitations and Future Work

The computer-aided CMF surgery planning procedure and skull restoration algorithm described in this thesis can be extended and improved in many aspects. The following sections highlight some areas that require improvement.

## 8.1 Integrated Planning Tool

At present, segmentation and mesh model construction are performed by several general tools outside the surgery planning tool. Segmentation of each fractured bone fragment is tedious and time-consuming. And it is not efficient to export and load data between different tools. Further more, it takes time for a user to learn how to use these different tools. A more effective segmentation tool designed for skull segmentation could reduce the complexity of segmentation and model construction process, and it can be integrated into the surgery planning tool. Our research team has begun to develop a more effective tool.

## 8.2 Execution Time

The execution time of the proposed restoration algorithm is about 30 minutes to 1 hour. Though this execution time meets the requirement for real surgical applications where pre-operative planning is usually performed a few days before the actual surgery, it would still be better to reduce execution time so that the surgeon can explore more options.

The bottle-neck of the restoration algorithm is the Laplacian deformation for generating estimated normal surfaces, which requires the solving of a large scale sparse linear system. In the current implementation, the linear system is solved by VXL library [C*00] using a single thread. In the future, the efficiency can be improved by solving the linear system in parallel [BT89] using multiple threads. Other possibilities would be to reduce the number of vertices of reference model or to apply Laplacian deformation in a coarse to fine manner.

## 8.3 Collision Avoidance

The skull restoration algorithm described in this thesis does not explicitly detect collisions of the restored bone fragments. Instead, it relies on the accurate estimation of normal surfaces and registration of bone fragments to the estimated normal surface to naturally avoid collisions. Experiments showed that the collision error is small for most cases. However, there are some cases where the collision is not negligible.

Collision detection is a well solved problem. There are various algorithms and packages available, e.g., proximity query package [GLM96] and vtkbioeng [Pan01], etc. These methods all involve building hierarchical approximations. However, detecting collisions of many bones is a computationally expensive process. Future work should investigate efficient method to avoid collision without having to check for collisions all the time during the optimization process. One possibility is to check for collision after the skull is restored, and make fine adjustment for bones with severe collisions. Another possibility is to improve the accuracy of normal surface estimation using better reference models such as statistical shape models and to improve the accuracy of the surface continuity-constrained registration algorithm. One more possibility is to intensively add gaps between the estimated normal surface and the adjacent confident bones, and use surface continuity-constrained registration algorithm to register the movable bone to these shrunk normal surface.

# Chapter 9

# Conclusion

This thesis has presented a computer-aided procedure for pre-operative planning of craniomaxillofacial (CMF) surgeries. This procedure is flexible and allows a surgeon to explore various surgical options during planning more efficiently and accurately. Within the procedure, two new algorithms are developed to solve two problems that could not be solved by existing methods.

First, an automatic algorithm for the identification of craniometric landmarks and planes is developed. It registers a reference skull model with known landmarks to a target skull to locate the landmarks, FP, and MSP on the target skull. Then, it iteratively refines the landmark locations, FP and MSP according to their medical definitions. Test results show that the proposed algorithm is robust and accurate for both normal skulls and skulls with minor fractures.

Second, an automated algorithm for skull restoration is developed. The algorithm iteratively repositions fractured bones one at a time. When repositioning a fractured bone, the algorithm first generates its estimated normal surface according to normality, lateral symmetry and surface continuity constraints. Then, it repositions the bone to match the estimated normal shape while fitting the MSP and FP landmarks to their corresponding planes. Test results show that the skull restoration algorithm converges quickly and produces accurate restored skull models.

The skull restoration algorithm is validated on real patient data following the validation scheme used by CMF surgeons. Validation results show that the restoration algorithm satisfies surgical requirements and produces surgical results which can be better than real surgical results as shown in post-operative CTs.

In conclusion, this thesis has made the following contributions:

- Development of a computer-aided procedure for assisting a surgeon in deriving a surgery plan for restoring a patient's deformed model back to the normal state by bone repositioning.
- Development of an algorithm for automatic identification of anatomical planes and landmarks of skulls.
- Development of an algorithm for restoring a patient's deformed model by bone repositioning.

Our collaborating surgeon in NUH is pleased with our planning tool and the validation results. We are working with him to deploy the planning tool for clinical trial. We are hopeful that our tool will be able to help surgeons perform more accurate surgery planning which in turn benefits the patients.

# References


[AAG09] Anderson D., Anderson L., Glanze W.: *Mosby's Medical Dictionary*. Mosby St. Louis, 2009.

[AG03] Avants B., Gee J.: The shape operator for differential analysis of images. In *Proc. Int. Conf. Information Processing in Medical Imaging* (2003).

[AGG*03a] Agus M., Giachetti A., Gobbetti E., Zanetti G., Zorcolo A.: Adaptive techniques for real-time haptic and visual simulation of bone dissection. In *IEEE Proc. Virtual Reality* (2003).

[AGG*03b] Agus M., Giachetti A., Gobbetti E., Zanetti G., Zorcolo A.: Real-time haptic and visual simulation of bone dissection. *Presence: Teleoperators & Virtual Environments 12*, 1 (2003), 110–122.

[AGG*04] Agus M., Giachetti A., Gobbetti E., Zanetti G., Zorcolo A.: Hardware-accelerated dynamic volume rendering for real-time surgical simulation. In *Workshop on Virtual Reality Interactions and Physical Simulations* (2004).

[BCT*04] Bhandarkar S., Chowdhury A., Tang Y., Yu J., Tolllner E.: Surface matching algorithms computer aided reconstructive plastic surgery. In *Proc. IEEE Int. Symp. on Biomedical Imaging: From Nano to Macro* (2004).

[BM92] Besl P., McKay N.: A Method for Registration of 3D Shapes. *IEEE Trans. Pattern Analysis and Machine Intelligence 14*, 2 (1992), 239–256.

[BPM*00] Bettega G., Payan Y., Mollard B., Boyer A., Raphaël B., Lavallee S.: A simulator for maaxillofacial surgery integrating 3d cephalometry and orthodontia. *Computer Aided Surgery 5*, 3 (2000), 156–165.

[BS08] Botsch M., Sorkine O.: On linear variational surface deformation methods. *IEEE Trans. Visualization and Computer Graphics 14*, 1 (2008), 213–230.

[BSMG09] Benazzi S., Stansfield E., Milani C., Gruppioni G.: Geometric morphometric methods for three-dimensional virtual reconstruction of a fragmented cranium: the case of Angelo Poliziano. *Int. J. Legal Medicine 123*, 4 (2009), 333–344.

[BT89] Bertsekas D. P., Tsitsiklis J. N.: Parallel and distributed computation.

[C*00] Consortium T., et al.: The vxl book, 2000.

[CBRY06] CHOWDHURY A., BHANDARKAR S., ROBINSON R., YU J.: Virtual craniofacial reconstruction from computed tomography image sequences exhibiting multiple fractures. In *Proc. IEEE Int Conf. on Image Processing* (2006).

[CBRY07] CHOWDHURY A., BHANDARKAR S., ROBINSON R., YU J.: Novel graph theoretic enhancements to ICP-based virtual craniofacial reconstruction. In *Proc. IEEE Int. Symp. on Biomedical Imaging: From Nano to Macro* (2007).

[CHV99] CAVALCANTI M., HALLER J., VANNIER M.: Three-dimensional computed tomography landmark measurement in craniofacial surgical planning: Experimental validation in vitro. *J. Oral and Maxillofacial Surgery 57*, 6 (1999), 690–694.

[CIB13] CIBC:, 2013. Seg3D: Volumetric Image Segmentation and Visualization. Scientific Computing and Imaging Institute (SCI), Download from: http://www.seg3d.org.

[CLL11] CHENG Y., LEOW W. K., LIM T. C.: Automatic Identification of Frankfurt Plane and Mid-Sagittal Plane of Skull. In *IEEE Int. Workshop on Applications of Computer Vision* (2011).

[CMC*04] CHABANAS M., MARECAUX C., CHOULY F., BOUTAULT F., PAYAN Y.: Evaluating soft tissue simulation in maxillofacial surgery using preoperative and postoperative ct scans. In *CARS* (2004).

[CMPB02] CHABANAS M., MARECAUX C., PAYAN Y., BOUTAULT F.: Models for planning and simulation in computer assisted orthognatic surgery. In *Proc. Int. Conf. on Medical Image Computing and Computer-Assisted Intervention (MICCAI)* (2002).

[CNR13] CNR I.: Meshlab, http://meshlab.sourceforge.net/, 2013.

[CP00] CHABANAS M., PAYAN Y.: A 3D Finite Element model of the face for simulation in plastic and maxillo-facial surgery. In *Proc. Int. Conf. on Medical Image Computing and Computer-Assisted Intervention (MICCAI)* (2000).

[CRT04] CLARENZ U., RUMPF M., TELEA A.: Robust Feature Detection and Local Classification for Surfaces based on Moment Analysis. *IEEE Trans. Visualization and Computer Graphics 10*, 5 (2004), 516–524.

[CSP*07] CHAPUIS J., SCHRAMM A., PAPPAS I., HALLERMANN W., SCHWENZER-ZIMMERER K., LANGLOTZ F., CAVERSACCIO M.: A new system for computer-aided preoperative planning and intraoperative navigation during corrective jaw surgery. *IEEE Trans. Information Technology in Biomedicine 11*, 3 (2007), 274–287.

[CTS*10] CEVIDANES L., TUCKER S., STYNER M., KIM H., AMD MAURICIO REYES J. C., PROFFIT W., TURVEY T., , JASKOLKA M.: 3D Surgical Simulation. *Am J Orthod Dentofacial Orthop 138*, 3 (2010), 361–371.

[DGL*01] DUTREUIL J., GOULETTE F., LAURGEAU C., ZOREDA J. C., LUNDGREN S.: Computer assisted dental implantology: A new method and a clinical validation. In *Proc. Int. Conf. on Medical Image Computing and Computer-Assisted Intervention (MICCAI)* (2001).

[DMCP*06] De Momi E., Chapuis J., Pappas I., Ferrigno G., Hallermann W., Schramm A., Caversaccio M.: Automatic extraction of the mid-facial plane for cranio-maxillofacial surgery planning. *International journal of oral and maxillofacial surgery 35*, 7 (2006), 636–642.

[DoC76] DoCarmo M.: *Differential Geometry of Curves and Surfaces*. Prentice-Hall, 1976.

[Edm65] Edmonds J.: Paths, trees, and flowers. *Canadian J. Mathematics 17*, 3 (1965), 449–467.

[Fie88] Field D. A.: Laplacian smoothing and delaunay triangulations. *Communications in Applied Numerical Methods 4*, 6 (1988), 709–712.

[GEH*99] Glombitza G., Evers H., Hassfeld S., Engelmann U., Meinzer H.: Virtual surgery in a tele-radiology framework. *IEEE Trans. on Information Technology in Biomedicine 3*, 3 (1999), 186–196.

[GH97] Garland M., Heckbert P. S.: Surface simplification using quadric error metrics. In *Proceedings of the 24th annual conference on Computer graphics and interactive techniques* (1997), ACM Press/Addison-Wesley Publishing Co., pp. 209–216.

[GIR04] Gladilin E., Ivanov A., Roginsky V.: Generic approach for biomechanical simulation of typical boundary value problems in cranio-maxillofacial surgery planning. In *Proc. Int. Conf. on Medical Image Computing and Computer-Assisted Intervention (MICCAI)* (2004).

[GLM96] Gottschalk S., Lin M. C., Manocha D.: OBBTree: A hierarchical structure for rapid interference detection. In *Proc. ACM SIGGRAPH* (1996).

[Gmb] GmbH V. I.: Amira. [Online; accessed 29-Feb-2012].

[GMbW04] Gunz P., Mitteroecker P., bookstein F., Weber G.: Computer aided reconstruction of human crania. *British Archaeological Reports International Series 1227*, 4 (2004), 92–95.

[GTH*03] Gassner R., Tuli T., Hächl O., Rudisch A., Ulmer H.: Craniomaxillofacial trauma: a 10 year review of 9543 cases with 21 067 injuries. *J. Cranio-Maxillofacial Surgery 31*, 1 (2003), 51–61.

[GWL99] Gumprecht H., Widenka D., Lumenta C.: Brainlab vectorvision neuronavigation system: technology and clinical experiences in 131 cases. *Neurosurgery 44*, 1 (1999), 97.

[GZDH01] Gladilin E., Zachow S., Deuflhar P., Hege H.: Validation of a linear elastic model for soft tissue simulation in craniofacial surgery. In *SPIE Medical Imaging Conference* (2001).

[GZDH03] Gladilin E., Zachow S., Deuflhard P., Hege H.: Realistic prediction of individual facial emotion expressions for craniofacial surgery simulations. In *Visualizatoin, Image-Guided Procedures, and Display* (2003).

[HFG*06] Huang Q.-X., Flöry S., Gelfand N., Hofer M., Pottmann H.: Reassembling fractured objects by geometric matching. In *ACM SIGGRAPH* (2006).

[Hor87] HORN B.: Closed-form solution of absolute orientation using unit quaternions. *JOSA A 4*, 4 (1987), 629–642.

[KGA*96] KEEVE E., GIROD S., AUGUSTIN A., BINNER A., GIROD B.: Interactive craniofacial surgery simulation. In *Proc. ACM SIGGRAPH* (1996).

[KGPG96] KEEVE E., GIROD S., PFEIFLE P., GIROD B.: Anatomy-based facial tissue modeling using the finite element method. In *IEEE Visualization* (1996).

[KGRG98] KEEVE E., GIROD S., R.KIKINIS, GIROD B.: Deformable modeling of facial tissue for craniofacial surgery simulation. *Computer Aided Surgery 3*, 5 (1998), 228–238.

[KRG*99] KOCH R., ROTH S., GROSS M., ZIMMERMANN A., SAILER H.: A framework for facial surgery simulation. In *Spring Conf. Computer Graphics* (1999).

[KSS09] KERWIN T., SHEN H.-W., STREDNEY D.: Enhancing realism of wet surfaces in temporal bone surgical simulation. *IEEE Trans. Visualization and Computer Graphics 15*, 5 (2009), 747–758.

[KWT88] KASS M., WITKIN A., TERZOPOULOS D.: Snakes: Active contour models. *Int. J. Computer Bision 1*, 4 (1988), 321–331.

[LAV09] LÜTHI M., ALBRECHT T., VETTER T.: Building shape models from lousy data. In *Proc. Int. Conf. on Medical Image Computing and Computer-Assisted Intervention (MICCAI)* (2009).

[LC87] LORENSEN W., CLINE H.: Marching Cubes: a high resolution 3D surface construction algorithm. In *ACM Siggraph Computer Graphics* (1987).

[LCL*02] LEE M., CHANG C., LIN C., LO L., CHEN Y.: Custom implant design for patients with cranial defects. *IEEE Engineering in Medicine and Biology Magazine 21*, 2 (2002), 38–44.

[LCL*03] LEE M., CHANG C., LIN C., LO L., CHEN Y.: T medical rapid prototyping in custom implant design for craniofacial reconstruction. In *IEEE Int. Conf. on Systems, Man and Cybernetics* (2003).

[Lit10] LITTLEBABYFACEFOUNDATION: Facial deformities. http://www.littlebabyface.org, 2010.

[LP98] LANGDON J., PATEL M.: *Operative Maxillofacial Surgery.* Chapman & Hall Medical, 1998.

[Ltd06] LTD I.: *Patient Information Guide to Inion CMF (Craniomaxillofacial) Surgery.* Inion Ltd, 2006.

[MDSB02] MEYER M., DESBRUN M., SCHRÖDER P., BARR A. H.: Discrete differential-geometry operators for triangulated 2-manifolds. In *Visualization and Mathematics III*, Hege H.-C., Polthier K., (Eds.). Springer-Verlag, 2002, pp. 35–57.

[Mim] MIMICS M.: Materialise surgicase cmf. [Online; accessed 19-Jan-2011].

[MSB*06] MORRIS D., SEWELL C., BARBAGLI F., SALISBURY K., BLEVINS N., GIROD S.: Visuohaptic simulation of bone surgery for training and evaluation. *IEEE Computer Graphics and Applications 26*, 6 (2006), 48–57.

[MSCP04] MOLLEMANS W., SCHUTYSER F., CLEYNENBREUGEL J., P.SUETENS: Fast soft tissue deformation with tetrahedral mass spring model for maxillofacial surgery planning systems. In *Proc. Int. Conf. on Medical Image Computing and Computer-Assisted Intervention (MICCAI)* (2004).

[MSCS03] MOLLEMANS W., SCHUTYSE F., CLEYNENBREUGEL J., SUETENS P.: Tetrahedral mass spring model for fast soft tissue deformation. In *Lecture Notes in Computer Science* (2003).

[MYF06] MASUDA H., YOSHIOKA Y., FURUKAWA Y.: Interactive mesh deformation using equality-constrained least squares. *Computers & Graphics 30*, 6 (2006), 936–946.

[Pan01] PANDY M. G.: Computer modeling and simulation of human movement. *Annual review of biomedical engineering 3*, 1 (2001), 245–273.

[PG96] PANCHERZ H., G
"OKBUGET K.: The reliability of the frankfort horizontal in roentgenographic cephalometry. *The European J. Orthodontics 18*, 4 (1996), 367.

[Phi05] PHILIP G.: *Statistical and geometric reconstruction of hominid crania: reconstructing australopithecine ontogeny.* PhD thesis, University of Vienna, Austria, 2005.

[PLT07] PHILLIPS J. M., LIU R., TOMASI C.: Outlier Robust ICP for Minimizing Fractional RMSD. In *Proc. Int. Conf. on 3D Digital Imaging and Modeling* (2007).

[RRS03] ROSSI M., RIBEIRO E., SMITH R.: Craniofacial asymmetry in development: an anatomical study. *The Angle orthodontist 73*, 4 (2003), 381.

[SBF*04] SCHMIDT J. G., BERTI G., FINGBERG J., CAO J., WOLLNY G.: A finite element based tool chain for the planning and simulation of maxillo-facial surgery. In *ECCOMAS 2004: European Congress on Computational Methods in Applied Science and Engineering* (2004).

[SCOL*04] SORKINE O., COHEN-OR D., LIPMAN Y., ALEXA M., ROSSL C., SEIDEL H.: Laplacian surface editing. In *Proc. Eurographics* (2004).

[SH] SIWEK D., HOYT R.: Anatomy of the human skull. http://skullanatomy.info.

[SOGB*09] SOFIE C. V., OKKERSE W., G. BRIJS M. D. B., BRAEM M., VERHEGGHE B.: 3d cephalometry: a new approach for landmark identification and image orientation. In *European Conf. of the Int. Federation for Medical and Biological Engineering* (2009).

[SS04] SEZGIN M., SANKUR B.: Survey over image thresholding techniques and quantitative performance evaluation. *J. Electronic Imaging 13*, 1 (2004), 146.

[SVBBC09] San Vicente G., Buchart C., Borro D., Celigueta J.: Maxillofacial surgery simulation using a mass-spring model derived from continuum and the scaled displacement method. *Int. J. Computer Assisted Radiology and Surgery 4*, 1 (2009), 89–98.

[Tay01] Taylor K.: *Forensic art and illustration*. CRC, 2001.

[TGG99] Teschner M., Girod S., Girod B.: Optimization approaches for soft-tissue prediction in craniofacial surgery simulation. In *Proc. Int. Conf. on Medical Image Computing and Computer-Assisted Intervention (MICCAI)* (1999).

[TPS*02] Troulis M., P.Everett, Seldin E., Kikinis R., Kaban L.: Development of a three-dimesional treatment planning system based on computed tomographic data. *J. Oral Maxillofacial Surgery 31*, 4 (2002), 349–357.

[TVE*07] Tardieu P., Vrielinck L., Escolano E., Henne M., Tardieu A.-L.: Computer-assisted implant placement: scan template, SimPlant, SurgiGuide, and SAFE system. *The Int. J. Periodontics & Restorative Dentistry 27*, 2 (2007), 141–149.

[VvCM*96] Verstreken K., van Cleynenbreugel J., Marchal G., van Steenberghe D., Suetens P.: Computer-assisted planning of oral implant surgery - an approach using virtual reality. In *Proc. Medicine Meets Virtual Reality* (1996).

[Wik] Wikipedia: Human skull. http://en.wikipedia.org/wiki/Human_skull.

[Wik12] Wikipedia: Traffic collision, 2012. [Online; accessed 27-Feb-2012].

[Woo31] Woo T.: On the asymmetry of the human skull. *Biometrika 22*, 3/4 (1931), 324–352.

[Wro10] WrongDiagnosis: statistics by country for cleft palate. http://WrongDiagnosis.com/, 2010.

[WW08] Winkelbach S., Wahl F. M.: Pairwise matching of 3d fragments using cluster trees. *IJCV 78*, 1 (2008), 1–13.

[WYLL11] Wei L., Yu W., Li M., Li X.: Skull assembly and completion using template-based surface matching. In *3D Imaging, Modeling, Processing, Visualization and Transmission (3DIMPVT), 2011 International Conference on* (2011).

[XGT05] Xia J., Gateno J., Teichgraeber J. F.: Three-dimensional computer-aided surgical simulation for maxillofacial surgery. In *Atlas of the Oral and Maxillofacial Surgery Clinics* (2005).

[XIS*00] Xia J., Ip H., Samman N., Wang D., Kot C., Yeung R., Tideman H.: Computer-assisted three-dimensional surgical planning and simulation: 3D virtual osteotomy. *Int. J. Oral and Maxillofacial Surgery 29*, 1 (2000), 11–17.

[XSC*00] Xia J., Samman N., Chua C. K., Yeung R. W. K., Wang D., Shen S. G., Ip H. H.-S., Tideman H.: PC-based virtual reality surgical simulation for orthognathic surgery. In *Proc. Int. Conf. on Medical Image Computing and Computer-Assisted Intervention (MICCAI)* (2000).

[YPH*06] Yushkevich P., Piven J., Hazlett H., Smith R., Ho S., Gee J., Gerig G.: User-guided 3d active contour segmentation of anatomical structures: Ssignificantly improved efficiency and reliability. *Neuroimage 31*, 3 (2006), 1116–1128.

[YWML11] Yin Z., Wei L., Manhein M., Li X.: An automatic assembly and completion framework for fragmented skulls. In *Proc. of Int. Conf Computer Vision* (2011).

[ZCL13] Zhang K., Cheng Y., Leow W. K.: Dense correspondence of skull models by automatic detection of anatomical landmarks. In *15th International Conference on Computer Analysis of Images and Patterns (CAIP)* (2013).

[ZGSZ03] Zachow S., Gladilin E., Sader R., Zeilhofer H.: Draw and cut: intuitive 3d osteotomy planning on polygonal bone models. In *Int. Congress Series* (2003).

[ZLES05] Zachow S., Lamecker H., Elsholtz B., Stiller M.: Reconstruction of mandibular dysplasia using a statistical 3D shape model. In *Int. Congress Series* (2005).